

Alma Mater Studiorum - Università di Bologna

**DOTTORATO DI RICERCA IN  
CHIMICA**

Ciclo XXXV

**Settore Concorsuale** : 03/A2 - Modelli e Metodologie per le Scienze Chimiche

**Settore Scientifico Disciplinare** : CHIM/02 - Chimica Fisica

**MULTISCALE MODELING OF  
LIGHT-HARVESTING SYSTEMS BASED  
ON RHODAMINE B AGGREGATES**

**Presentata da:** Giacomo Fanciullo

**Coordinatore Dottorato:**  
Prof. Luca Prodi

**Supervisore:**  
Prof. Ivan Rivalta

**Co-supervisore:**  
Prof. Marco Garavelli

Esame finale anno 2023

---

# Contents

<b>Abstract</b>	<b>5</b>
<b>Introduction</b>	<b>7</b>
<b>1 Rhodamine B based Light-Harvesting Systems</b>	<b>11</b>
1.1 The Optical Properties of Rhodamine B . . . . .	11
1.2 Rhodamine B in Light-Harvesting Nanomaterials . . . . .	12
1.3 Experimental Evidences of Rhodamine B Dimerization . . . . .	14
<b>2 Energy Transfer Dynamics in Rhodamine B Networks</b>	<b>17</b>
2.1 Theoretical Background: The Macroscopic Models for Energy Transfer Dynamics	17
2.1.1 The Förster Model for Energy Transfer . . . . .	17
2.1.2 The Macroscopic Model of Time-Evolving Exciton Density . . . . .	18
2.1.3 Energy Transfer Mechanisms and Macroscopic Models . . . . .	19
2.1.4 The Gösele Model . . . . .	21
2.1.5 The Exciton-Exciton Annihilation . . . . .	22
2.2 A New Macroscopic Models for Exciton Density Decay in RB Networks . . .	23
2.2.1 Inclusion of EEA and Quenchers. . . . .	23
2.2.2 Investigating the Effect of Model Parameters . . . . .	25
2.2.3 Toward a Reliable Fitting of Experimental Fluorescence Decays . . . .	27
<b>3 Molecular Dynamics Simulation of Rhodamine B Aggregation in Water</b>	<b>31</b>
3.1 Theoretical Background: Molecular Mechanics and Molecular Dynamics . . .	31
3.1.1 Energy Calculation in Molecular Mechanics . . . . .	32
3.1.2 Equations of Motion and Different Ensembles in Molecular Dynamics	33
3.2 Simulating Rhodamine B Aggregation in Water . . . . .	34
3.2.1 Force Field Parametrization . . . . .	34
3.2.2 Molecular Dynamics Simulations: Computational Methodology . . . .	37
3.2.3 Molecular Dynamics Simulations: Results . . . . .	38
<b>4 Density Functional Theory Studies of Rhodamine B and Its Dimers</b>	<b>45</b>
4.1 Theoretical Background: Density Functional Theory for Electronic-Structure	
Calculations . . . . .	45

---

4.1.1	Wavefunction Description of Electronic-Structure: the Schrödinger Equation . . . . .	45
4.1.2	Density Functional Theory . . . . .	49
4.1.3	Kohn-Sham Theory . . . . .	50
4.1.4	The Correction for Dispersion Interactions. . . . .	53
4.1.5	Generalized Kohn-Sham Theory . . . . .	53
4.1.6	Solvent Effect: the Polarizable Continuum Model . . . . .	57
4.1.7	Excited State Calculations: Time-Dependent Density Functional Theory	58
4.1.8	Excited State Analysis: Natural Transition Orbitals . . . . .	61
4.1.9	Charge Transfer States in Time-Dependent Density Functional Theory	62
4.2	DFT Investigations on Rhodamine B Dimerization . . . . .	66
4.2.1	Geometrical Conformations of Rhodamine B Dimers . . . . .	66
4.2.2	TD-DFT Investigations on Rhodamine B Dimers Excited States . . .	70
4.2.3	Rhodamine B Excited States . . . . .	72
4.2.4	Rhodamine B Dimers Excited States . . . . .	73
4.2.5	A Novel Strategy for Improving the Excited State Calculation for Rhodamine B and Its Dimers. . . . .	77
	<b>Conclusions.</b>	<b>81</b>
	<b>A Force Field Parameters.</b>	<b>85</b>
	<b>Bibliography.</b>	<b>89</b>

# Abstract.

Rhodamine B (RB) is a positively charged organic dye which has been successfully exploited in the synthesis of light harvesting (LH) nano-antennas. These antenna systems are characterized by networks in which thousands of RB dyes can harvest light and efficiently transfer their excitation energy to a single final acceptor molecule. Since RB is prone to form dimers acting as quenchers for the fluorescence, high energy transfer (ET) efficiencies can be reached only when using bulky and hydrophobic counterions that are able to prevent the RB dimerization, acting as spacers between dyes. In this PhD thesis, a multiscale theoretical study aimed at providing insights into the structural, photophysical and optical properties of RB and its aggregates is presented. At the macroscopic level, the atomistic details are completely neglected and a phenomenological theoretical model can be conceived for describing the fluorescence decay of RB networks detected experimentally. A model taking into account the effect of both the quenching from dimers and the exciton-exciton annihilation is presented and analyzed. The results of such macroscopic model showed that the quenching due to RB dimers produces an acceleration in the long time scale of the fluorescence decay, which can be exploited in global fitting analysis procedures to determine relevant chemical and photophysical information. At the mesoscopic level, the atomistic structure of the system is considered but the electronic structure of the involved species is completely neglected. In this context, the RB aggregation in water solution in presence of different kinds of counterions has been studied with molecular dynamics (MD) simulations. In particular, a new classical force field (FF) has been carefully parametrized for correctly describing the RB flexibility and the RB-RB interaction driving the dimerization. The MD simulations performed employing the newly developed FF resulted to be in full agreement with the experimental evidences: the RB/counterion aggregation occurs only in presence of bulky and hydrophobic counterions, while is absent if a small anion is used as RB counterion. The results demonstrated the hypothesis that bulky and hydrophobic anions act as spacers, preventing the formation of fluorescence quenching species, such as the H dimers. Finally, at the microscopic level a full description of the electronic structure of molecular species was considered by means of Density Functional Theory (DFT) methodologies. DFT calculations have been used to further demonstrate the capability of bulky counterions to hinder the formation of stacked dimers but also to characterize the RB electronic excited states and to investigate the photophysical properties of RB dimers. Regarding the latter, several commonly used exchange-correlation functionals have been tested within a time-dependent DFT (TD-DFT) approach, showing that a correct reproduction of electronic transition energies for RB and its dimers is far from trivial. Moreover, it has been shown that the standard procedures proposed in literature for obtaining *ad hoc* optimized DFT functionals do not

---

work properly for the case of RB and its dimers. The detailed analysis on the effect of the various functional parameters has showed that the short range Hartree-Fock exchange is the crucial quantity for ameliorating the TD-DFT performances. As a consequence, a new class of range-separated hybrid functionals containing a proper and physically motivated amount of such an exchange has been proposed and successfully tested on RB dimers.

# Introduction.

The work presented in this PhD thesis stems from a scientific collaboration of our group with two research groups from Strasbourg University and CNRS, France, (Dr. A. Klymchenko, Prof. P. Didier and Dr. J. Léonard), in the framework of a joint project aimed at characterizing and optimizing the energy transfer (ET) properties of artificial light-harvesting (LH) nanomaterials (LHNANOMAT, AAPG2019, CE9: 8.11 “Nanomatériaux et nanotechnologies pour les produits du futur”). These nanosystems are based on the rhodamine B (RB) organic dye and consist of polymeric nanoparticles (NPs) in which thousands of RBs are embedded to form dye networks able to harvest the solar light and transfer the energy to a single final acceptor [1]. The technological relevance of such nanosystems is associated to the high ET efficiency observed in the RB networks, and it has been shown that high efficiencies can be achieved only by combining the cationic RB with the use of specific bulky and hydrophobic counterions [2]. Indeed, RB is well known for its tendency to aggregate and certain type of RB dimers (as well as larger oligomers) have been experimentally found to be quenchers for the fluorescence [3, 4]. Indeed, aggregations featuring closely interacting dyes within the NPs’ networks can be responsible for the loss of excitations from the network. In this context, bulky and hydrophobic counterions are able to successfully hinder the RB-RB dimerization within the NPs working as spacers between dyes without affecting their intrinsic photophysical properties, thereby ensuring high ET efficiencies of dye networks.

As computational chemists, our tasks in the project aimed at the interpretation of the experimental results provided by our collaborators by means of reliable theoretical modeling and simulations. We chose to set up a *multiscale* theoretical approach (from *macro-*, to *meso-*, to *micro-scopic* level) in order to attack the complexity of the scientific problem under investigation, mainly focusing on the effect of dimerization within RB/counterion networks in the target NPs. The first part of our study regarded the simulation of ET processes happening in polymeric NPs at the *macroscopic* scale, in which the atomistic detail of the network structure is completely neglected by assuming a homogeneous distribution of RBs involving a certain amount of RB dimers with fluorescence quenching properties. The second part focused on the simulations of RB aggregation at the *mesoscopic* level, with the dyes’ organization within the aggregates being fully described at the atomistic level but totally neglecting the electronic structure of each molecule. Such a study has been performed by means of molecular dynamics (MD) simulations aimed at reproducing the aggregation of RB molecules induced by the presence of the hydrophobic and bulky counterions in water solution (that is, in absence of the polymeric medium), focusing in particular in determining the dimerization extent within the NPs composed of RBs and counterions. Such simplified nano-aggregates are of extreme theoretical interest because, first, their study can provide a

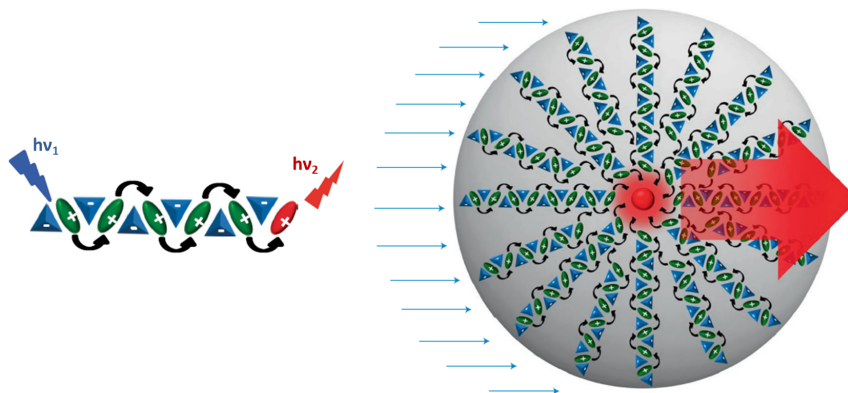


**Figure 1:** Light-harvesting nano-antennas based on RB. On the left, a schematic representation of the energy transfer among RB units (in green) through which the excitation reach the final acceptor (in red). Blu triangles represent the bulky counterions acting as spacers for the dyes. On the right, a hypothetical arrangements of RB/counterions in a nanometric polymeric matrix.

primary structural characterization of RB aggregation at the atomistic level and, secondly, such NPs have been experimentally found to feature ET properties which are very similar to those observed in the polymeric NPs [5]. Finally, the third part of our study regarded the investigation of structural and electronic properties of monomeric and dimeric species at the *microscopic* level, employing quantum mechanical (QM) calculations based on density functional theory (DFT). The results of our multiscale studies are presented in this thesis with the organization described below.

In Chapter 1, a brief summary on the optical and photophysical properties of RB and its dimer are reported along with relevant experimental data (provided by our collaborators). Such data comprise: i) the experimental evidences associated to RB dimerization in solution; ii) the evidence of exciton-exction annihilation (EEA) processes within the LH NPs; and iii) a detailed spectroscopic study carried out on chemically synthetized covalently linked RB pairs.

In Chapter 2, the macroscopic model conceived for the purpose of fitting the experimental fluorescence decays of LH NPs is presented, including all possible photophysical processes that could happen within the RB network. The phenomena included in the macroscopic models are: i) the ET processes moving the excitations through the dyes (considering two possible mechanisms), ii) the fluorescence quenching due to dimers and iii) the EEA.

In Chapter 3, the results of MD simulations aimed at describing the RB aggregation in water are reported, with the aim of determining the effects of bulky hydrophobic counterions. In order to perform reliable simulations, a new Force Field for RB monomers and dimers has been carefully parametrized, providing a reliable reproduction of the RB intramolecular flexibility and of the RB-RB interactions.

In Chapter 4, two types of QM studies are reported, involving respectively the geometrical and the electronic structure characterizations of RB dimers both investigated by means

---

of DFT methods. The first study aimed at the quantification of how the stability of various dimers conformations are affected by the presence of different counterions. The second study focused on the calculation of the excited states of RB monomers and dimers aimed at determining their photophysical properties with particular attention on the description of dark charge transfer states, which are of crucial importance in assessing the dimers optical behavior. In particular, the performance of the most commonly used exchange-correlation functionals is firstly extensively analyzed, showing that a correct reproduction of experimental data, such as the monomer and dimer transition energies, is far from trivial. Secondly, it is shown that the standard procedures proposed in literature for obtaining ad hoc optimized DFT functionals do not work properly for the case of RB and its dimers. Finally, based on a detailed analysis of how the functional parameters affect the results, it is proposed a new recipe for obtaining a reliable DFT functional able to reproduce the desired optical properties.

Each chapter is structured with a first part containing the theoretical background of the methodology used, in the second part, to obtain results that are then discussed.



# Chapter 1

## Rhodamine B based Light-Harvesting Systems

### 1.1 The Optical Properties of Rhodamine B

Rhodamine B (RB) is a xanthene derivative organic dye that by virtue of its remarkable optical properties has been exploited in a wide range of technological applications, including fluorescent probes [7], chromic materials [8], thermal lenses [9] and optical thermometers for biological systems [10]. The molecular structure of RB, the transition dipole moment of its main electronic (HOMO to LUMO, i.e. H-L) excitation and its absorption spectra are depicted in Figure 1.1, showing a vibronic progression featuring a shoulder that is blue shifted with respect to the main absorption peak. The most important optical property of RB is the high fluorescence quantum yield [6] of this electronic excitation. However, RB has a large tendency to form dimers, which are well known to be responsible for the quenching of its fluorescence.

Even in solution, the RB dimerization can be directly observed by simply increasing the dye concentration up to few micromolar units [11]. In fact, the spectroscopic fingerprints of dimers have been straightforwardly identified since the late 80's, basing on fundamental exciton theory [12]. Upon increasing the concentration, indeed, the RB absorption spectrum shows a slight red shift of the main peak accompanied by a sensible increase of the relative intensity of the vibronic blue-shifted shoulder. The formation of J dimers is expected to red shift the main peak, while H dimers, associated to the  $\pi$ - $\pi$  stacking of the xanthene moieties, are expected to generate a blue shifted peak, lying very close in wavelength to the the monomeric vibronic shoulder, thus increasing its relative intensity.[11] Regarding the emission, the exciton theory predicts that H dimers generate low lying non-emitting (i.e. dark) states that can be populated from the higher absorbing (i.e. bright) state through an internal conversion mechanism, quenching the RB fluorescence. This prediction is indeed experimentally observed: other than raising the shoulder intensity, the concentration increase always provokes a strong drop of fluorescence quantum yield (FQY) [3, 4]. On the other hand, J dimers formation, generating a red shifted peak also in emission, is not clearly detected in solution while it was straightforwardly observed in systems in which RB

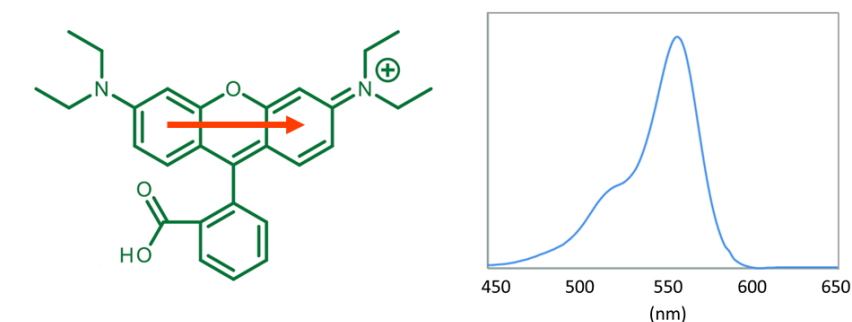


**Figure 1.1:** RB chemical structure with the transition dipole moment of its main (H-L) electronic excitation (red arrow) and its absorption spectrum (in water), featuring the typical vibronic progression and a clearly detectable blue-shifted shoulder.

is adsorbed on substrates such as quartz plates [13], mineral clays [14] and silica dip-coated films [15].

## 1.2 Rhodamine B in Light-Harvesting Nanomaterials

One of the most promising RB technological application is in artificial LH nanomaterials. In particular, RB alkylated derivatives have been successfully employed as the fundamental units for building photoactive dye networks encapsulated in polymeric nanoparticles (NPs), showing fascinating collective optical properties such as the reversible on/off switching of the single-particle fluorescence [2]. This phenomenon makes such systems of extreme technological interest, because it suggests that the excitation can easily migrate throughout the network via *energy transfer* (ET) among RB dyes, thereby allowing a single quencher molecule (if present) to suppress the fluorescence of the whole NP. These polymeric nanosystems have been in turn exploited to create giant LH nano-antennas [1], in which the dye network harvests the solar light and transfer the excitation energy from thousands of RBs to a single final acceptor molecule. In this way, the emission intensity of the single molecule acceptor is impressively enhanced to such an extent that it can be detected even with a light intensity 10.000 times lower than that generally required in single-molecule measurements.

The RB tendency towards dimerization has been observed also in LH nanomaterials: indeed, also in these systems the increase of the dye loading is always accompanied by an increase of the RB dimerization, which manifest itself through the same spectroscopic fingerprints observed in solutions, [2, 1] as describe above. Clearly, dimerization represents a serious issue for the efficiency of LH because of the quenching channels provided by dimers. Therefore, several efforts have been made in order to hinder as much as possible the dimerization extent. A successful chemical strategy consists in hindering the RB-RB interaction (i) by introducing bulky counterions able to bound RB thus acting as a spacer among dyes and (ii) by attaching very long and cumbersome alkylic chains on the carboxylic group of RB. Very interestingly, the counterion has turned out to be a fundamental ruler which can be exploited by chemists to regulate the network formation and thereby the nanosystem

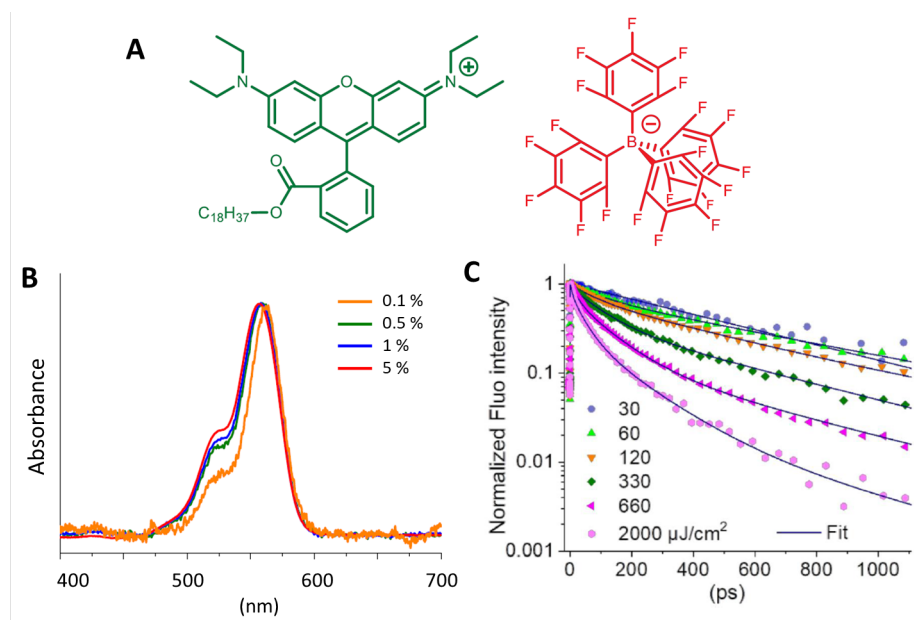


**Figure 1.2:** (A) Chemical structure of alkylated RB and F5TPB counterion used for building LH NPs. (B) Absorption spectra of single NPs showing the shoulder raising upon increasing the RB loading (expressed as weight percentage). (C) Fluorescence decays for single NP measured upon increasing the light pulse power (in  $\mu\text{J}$ ). The fingerprint of EEA is the decay acceleration as function of the light power.

photoactivity [16]. For instance, other than the counterion's size that clearly affects the dimerization extent, another useful parameter is its hydrophobicity, which can be used to regulate the encapsulation of the dyes within the polymer matrix and also the dispersion degree of the dyes within the network. Another parameter that can be used to regulate the network formation is represented by the kind of polymer employed: for example, the polymer hydrophobicity has been found to be another ruler for the dispersion degree of the dyes within the network [17]. A counterion that has been proved to successfully prevents the dimerization is the derivative of tetraphenylborate (TPB) having fully fluorinated phenyls (namely F5TPB, as each phenyl bears 5 fluorine atoms), whose structure is depicted in Figure 1.2A, close by the structure of the RB octadecyl ester, a modified version of RB that has been used for building efficient LH NPs [2, 1]. Despite the combination of bulky counterions and long alkylic chains really helps in reducing the dimerization, the dimers formation can not be totally prevented. Figure 1.2B reports the absorption spectrum and the FQY of NPs [2], showing how the presence of dimerization is still evident although being very reduced. In fact, upon increasing the RB loading, the blue-shifted shoulder in the absorption spectrum slightly increases and FQY slightly decreases, thus indicating that a certain extent of H dimers is still present.

Other than quenching from dimers, another optical feature experimentally observed in

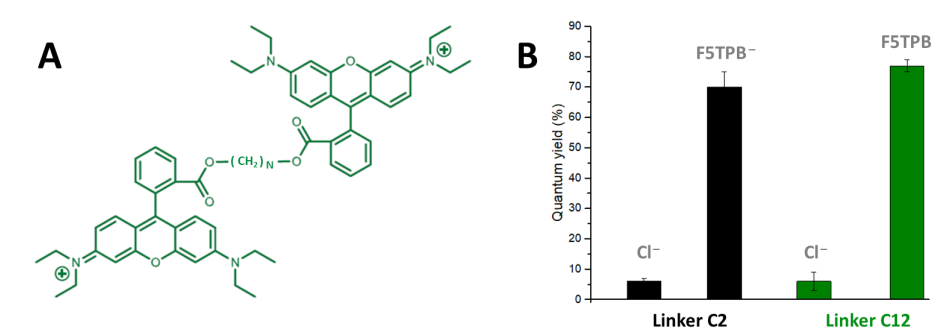


**Figure 1.3:** (A) Chemical structure of the RB-C-RB covalently linked couple (N=2,12). (B) FQY values for the RB-C-RB solutions in dioxane clearly showing the counterion effect on the dimerization.

LH NPs is the presence of a fascinating ET process involving two excited dyes, i.e. the so called *exciton-exciton annihilation* (EEA) responsible for an acceleration of the loss of excitations (or excitons) from the system. The presence of EEA can be easily revealed by measuring the fluorescence decay of the system in experiments involving laser pulses. Upon increasing the light power of the excitation pulse, a higher number of RBs are excited, thus increasing the probability of having EEA and accelerating the fluorescence decay. Figure 1.2C depicts a typical single NP's fluorescence decay measurement, clearly showing the acceleration of fluorescence decay obtained upon increasing the light power.

### 1.3 Experimental Evidences of Rhodamine B Dimerization

In this section, some experimental measurements (courtesy of our collaborators from Strasbourg University) aimed to rationalize the RB dimerization are reported. The characterization of dimers' photophysical properties focused on the use of bulky counterions to affect the RB dimerization. In order to more easily induce the dimer formation, RB couples covalently linked through an alkylic chain connecting the two carboxylic groups (indicated as RB-C-RB) have been synthesized. Two different chains composed by 2 and 12 carbon atoms (labelled as C2 and C12, respectively) have been compared with the aim of elucidating how photophysical properties change passing from the case in which the two RBs are forced to be very close (C2) to the case in which they are allowed to be more spaced (C12). The structure of such covalently linked RBs are depicted in Figure 1.3A. To test the counterion effect, the bulky F5TPB (see Figure 1.2) has been compared with the small chloride anion. All measurement discussed below refer to RB-C-RB solutions in dioxane. The FQY of these solutions are reported in Figure 1.3B, from which the counterion effect is clearly evident. Since the small Cl<sup>-</sup> counterion cannot act as a dye spacer, the two RBs can efficiently dimerize, thus leading to a serious FQY drop, which can be imputed to the formation of quenching stacked H dimers. Moreover, such a drop is observed with both linkers (C2 and C12), suggesting that the very hydrophobic environment provided by dioxane always sta-

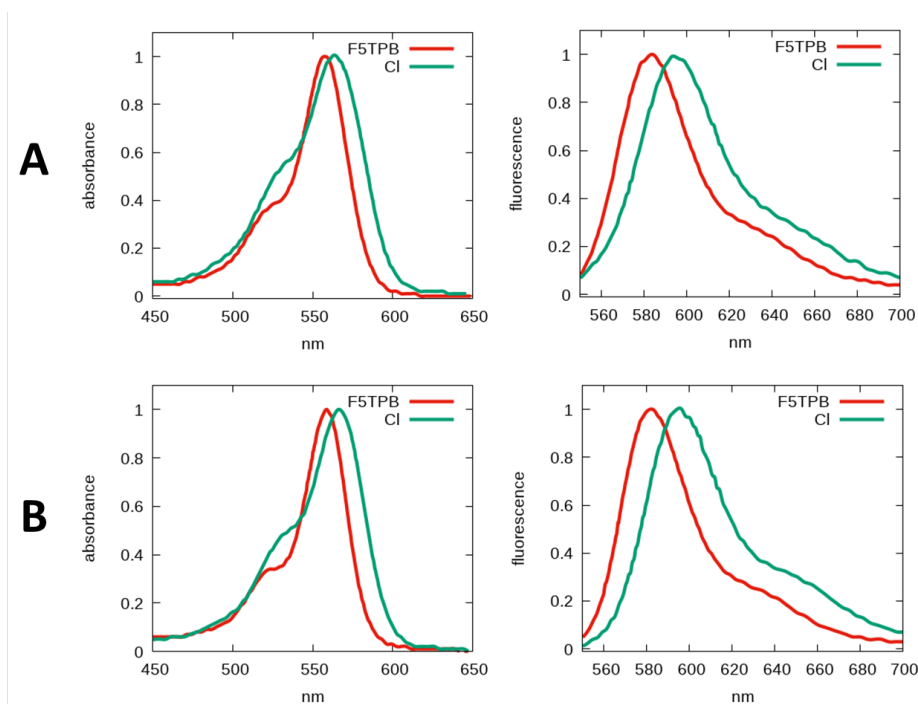


**Figure 1.4:** Absorption and fluorescence spectra of RB-C-RB solutions in dioxane with C2 (**A**) and C12 (**B**) linkers, clearly showing how the counterion affects the RB dimerization.

bilizes the stacking between RBs. On the other hand, the F5TPB counterion turns out to efficiently prevent the dimerization, as indicated by the very high FQY values observed with both linker chains. The associated absorption and emission spectra are reported in Figure 1.4. Regarding absorption spectra, the FQY drop observed with the  $\text{Cl}^-$  is, as expected, associated to an increase of the absorption shoulder corresponding to the blue shifted H dimers' absorption. A rather striking result is that when passing from F5TPB to  $\text{Cl}^-$  a slight red shift of the mean peak it is also observed. Such a red shift is normally imputed to the formation of fluorescent J dimers, and this hypothesis is confirmed by the presence of a red shift also in the main peak of fluorescence spectra. In summary, the F5TPB counterion is found to efficiently act as a spacer for RBs preventing the formation of both H and J dimers independently from the chain length. Such dimers are instead clearly formed when using the  $\text{Cl}^-$  counterion, for which the typical fingerprints of RB dimers are observed (again, independently from the chain length), i.e. the FQY drop and the increasing of the blue-shifted absorption shoulder (H dimers) along with the red shift of the main peak in both absorption and fluorescence (J dimers).



## Chapter 2

# Energy Transfer Dynamics in Rhodamine B Networks

### 2.1 Theoretical Background: The Macroscopic Models for Energy Transfer Dynamics

#### 2.1.1 The Förster Model for Energy Transfer

Energy transfer (ET) is a photophysical process through which an excited molecule is able to transfer its excitation energy to a another molecule (in its ground state) which can be even quite far from the excited one. A simple representation of this process is depicted in figure 2.1: the donor (D) excited molecule relaxes to its ground state (GS) and its excitation energy is immediately captured by the acceptor (A) molecule that therefore populates its excited state (ES).

The theoretical description for the mechanism of moving the excitation energy through ET among dyes dates back to the '50s. In his pioneering work, Theodore Förster presented the quantum mechanical model who represented the milestone for calculating the rate constant governing the ET [18, 19], which is nowadays referred to as the *Forster's resonance ET* (FRET) model [20, 21]. The FRET model assumes that the ET between two molecules

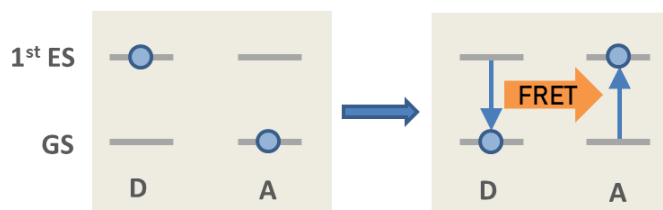


**Figure 2.1:** Pictorial representation of the FRET mechanism.

is governed by the interaction between their transition dipole moments. The formulation leads to a handy expression that traces back the ET rate constant to few parameters directly obtainable from experiments, such as the molecules' radiative lifetime, FQY, absorption and emission spectra. Considering a generic D-A couple, the FRET rate constant is given by

$$k_{FRET} = \frac{1}{\tau_D} \left( \frac{R_0}{R} \right)^6 \quad (2.1)$$

where  $R$  is the D-A separation and the  $1/R^6$  dependence derives from the dipole-dipole interaction energy,  $\tau_D$  is the donor's fluorescence lifetime and  $R_0$  is the so called *Forster radius* given by

$$R_0^6 = \frac{9 \ln(10) \kappa^2 \Phi_D}{128 \pi^5 n^4 N_A} J \quad (2.2)$$

where  $\Phi_D$  is the donor's FQY,  $n$  is the refractive index of the medium,  $\kappa$  is the geometrical factor describing the relative orientation of transition dipole dipoles,  $N_A$  is the Avogadro's number and  $J$  is the so called *spectral overlap* given by the integral

$$J = \int F_{norm}^D(\lambda) \epsilon_{abs}^A(\lambda) \lambda^4 d\lambda \quad (2.3)$$

where  $F_{norm}^D$  is the normalized donor's fluorescence spectrum lineshape and  $\epsilon_{abs}^A$  is the acceptor's molar extinction coefficient. Clearly, eq.(2.3) represents a strictly and physically motivated condition for having the ET: the donors' emission and the acceptor's absorption must share a spectral window, otherwise the overlap (and thus also the rate constant) is zero.

### 2.1.2 The Macroscopic Model of Time-Evolving Exciton Density

The FRET model is very useful to interpret the time-resolved fluorescence measurements because it can be used for providing a connection between the microscopic ET processes involving the individual D-A couples and the optical behaviour measured for the whole macroscopic sample. For instance, based on FRET, *macroscopic models* can be developed to quantitatively simulate the experimental fluorescence evolution. The fluorescence intensity  $I$  can be assumed to be at each time proportional to the so called *exciton density*,  $C$ , defined as the volume concentration of the emitting (excited) dyes. Considering the donor as the emitting specie of interest, one thus assumes  $C_D(t) \propto I(t)$ , where the proportionality is normally experimentally accessible since the number of absorbing dyes can be in principle exactly determined, at least immediately after the irradiation. The experimental data that can be more easily simulated with such macroscopic models are the fluorescence decay measurements, obtained by recording the fluorescence intensity evolving after the excitation of the sample with a very rapid excitation pulse. In fact, with laser pulses there is not a continuous source of excitation, so one needs only to know the initial exciton density to study how the ET processes affect its evolution.

Macroscopic models are based on the following microscopic equation for the time evolu-

tion of the exciton density [22]:

$$\frac{dC_D(t)}{dt} = -\frac{1}{\tau_D}C_D(t) - \frac{4\pi}{V^2} \sum_d^{N_D} \sum_a^{N_A} \int f[p_{da}(R, t)] dR \quad (2.4)$$

where  $V$  is the system volume,  $N_D$  and  $N_A$  are the total number of donor and acceptor molecules respectively and  $f$  is a function describing the probability of having an ET from the  $d$ -th donor to the  $a$ -th acceptor, expressed in terms of the D-A pair probability  $p_{da}$  [23], which quantifies the probability of having the D-A couple separated by  $R$  at a given time  $t$ . This expression actually contains the full microscopic information of the system, and integration over  $R$  means that all possible D-A spatial separations are taken into account. When a homogeneous distribution of dyes is considered, proper approximations allow to recast eq.(2.4) into a fully macroscopic equation which takes the general form

$$\frac{dC_D(t)}{dt} = -\frac{1}{\tau_D}C_D(t) - k(t)C_A(t)C_D(t) \quad (2.5)$$

where  $k(t)$  is the macroscopic ET rate constant. In the following section, the two most widely used models for the ET mechanism (with the associated  $f$  functions) are summarized and discussed.

### 2.1.3 Energy Transfer Mechanisms and Macroscopic Models

#### The Direct FRET Mechanism

When the ET is assumed to happens through a direct FRET mechanism (often referred to as the *long range* mechanism since it can involve also quite far D-A couples, see figure 2.2.A), the  $f$  function is simply given by

$$f[p_{da}(R, t)] = \frac{1}{\tau_D} \left( \frac{R_0}{R} \right)^6 p_{da}(R, t) \quad (2.6)$$

and the kinetic constant for the macroscopic equation (2.5) is found to be [24]:

$$k(t) = \frac{2}{3}\pi R_0^3 \sqrt{\frac{\pi}{\tau_D t}} \quad (2.7)$$

Here, the  $t^{-1/2}$  dependence can be interpreted with the fact that the ET rapidly happens between close D-A couples, thereby reducing the probability of having further ET with the passing of time.

#### Pure Diffusive ET Mechanism

A different, still widely used macroscopic model considers the excitation to be able to move through donors and eventually reach the acceptor through a sequence of D-D ET steps, for which one can consider the same mechanism of figure 2.1 but with the relaxed donor replacing the relaxed acceptor. In a very simplified picture, the microscopic mechanism

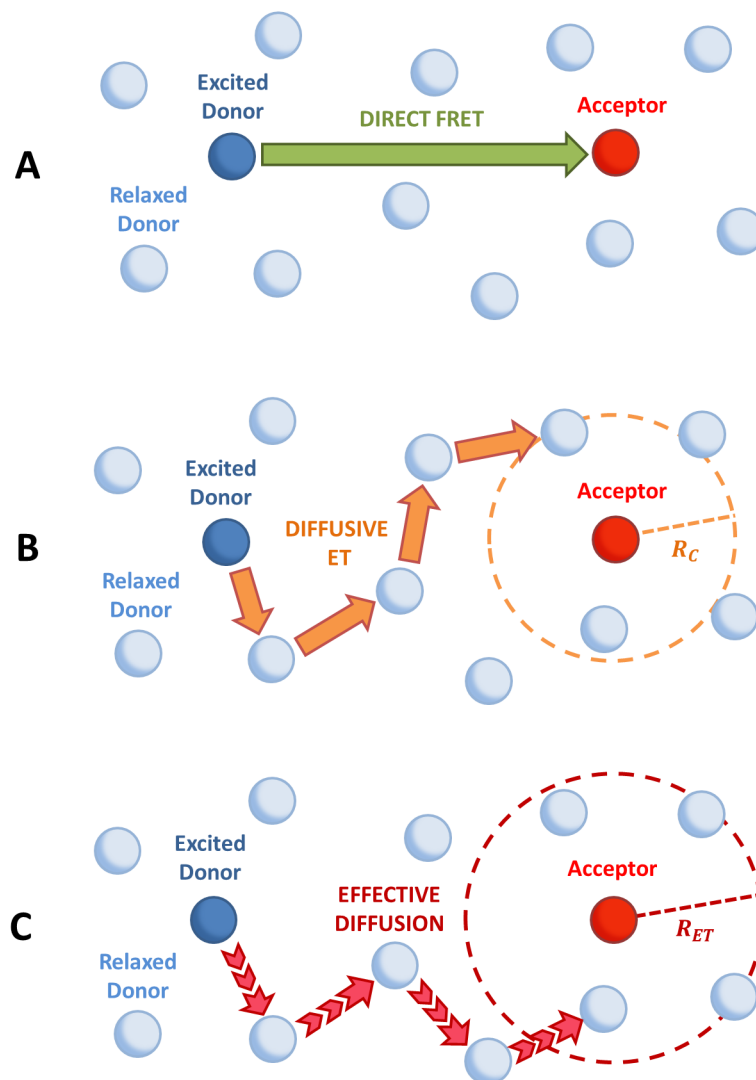


**Figure 2.2:** Schematic representation of possible ET mechanisms. (A) Direct FRET mechanism. (B) Diffusive ET mechanism involving a sequence of donor-donor ET steps that is macroscopically described as a classical diffusion governed by a simple diffusion coefficient  $D$ . The final ET to the acceptor is assumed to take place when the excitation enters a contact sphere defined by the contact radius  $R_C$ . (C) Gösele ET mechanism describing the combined action of both direct and diffusive ET as an effective diffusive mechanism driven by the usual diffusion coefficient  $D$  but governed by a new contact radius  $R_{ET}$ .

through which the D-D ET happens is ignored, and the excitation motion is assumed to be governed simply by a diffusion coefficient  $D$ . Also the mechanism for the final D-A ET is extremely simplified: ET is assumed to take place when the excitation driven by diffusion enters a *contact sphere* centred on A and defined by a certain *contact radius*  $R_C$  (see figure 2.2.B). In this mechanism, which has been originally developed for describing chemical reactions driven by diffusion [23], the  $f$  function takes the form

$$f[p_{da}(R, t)] = D\nabla^2 p_{da}(R, t) \quad (2.8)$$

which describes how the pair probability is affected by the diffusion that moves the donor's excitation, thus destroying the D-A couple separated by  $R$ . Therefore, the integral over  $R$  appearing in eq.(2.4) becomes the expression for the diffusion-driven flux through a generic surface, and the ET rate constant is simply obtained by integrating for  $R \geq R_C$ , which leads to the flux of the  $d$ -th donor through the contact sphere centred on the  $a$ -th acceptor. The kinetic constant for the macroscopic equation (2.5) is found to be [23]:

$$k(t) = 8\pi DR_C \left( 1 + \frac{R_C}{\sqrt{2\pi Dt}} \right) \quad (2.9)$$

#### 2.1.4 The Gösele Model

Gösele and collaborators derived a more complete macroscopic model in which the D-A ET is allowed to happen through a combination of both the direct FRET and the diffusive mechanisms [22, 24]. In this case, the  $f$  function is straightforwardly given by the sum

$$f[p_{da}(R, t)] = \frac{1}{\tau_D} \left( \frac{R_0}{R} \right)^6 p_{da}(R, t) + D\nabla^2 p_{da}(R, t) \quad (2.10)$$

but this more complicated form makes impossible to analytically obtain an expression for the kinetic constant, and for that reason authors employed several physically motivated approximations to simplify the mathematical treatment. First of all, it is assumed that at very short times the direct FRET immediately takes place while diffusion is considered to have not started yet, i.e. eq.(2.10) reduces to eq.(2.6). This leads to a kinetic constant for the short times analogous to that of eq.(2.7):

$$k_{short}(t) = \frac{2}{3}\pi R_0^3 \sqrt{\frac{\pi}{\tau_D t}} \quad (2.11)$$

Secondly, it is assumed that for long times a stationary regime holds, i.e. the probability of having a decay due to both mechanisms is considered constant in time, and the corresponding kinetic constant (which becomes time independent) is found to be:

$$k_{long} = 4\pi D \cdot 0.676 \left( \frac{R_0^6}{\sqrt{\tau_D}} \right)^{1/4} \quad (2.12)$$

Finally, a reliable albeit approximate form for the global rate constant is assumed to be simply given by summing the expressions for the two temporal limits, i.e.  $k(t) = k_{short}(t) +$

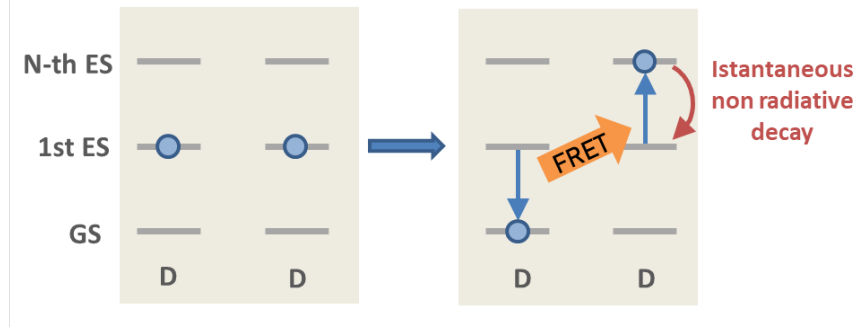


**Figure 2.3:** Pictorial representation of the EEA mechanism.

$k_{long}$ , which can be rewritten in a more compact form as

$$k(t) \approx 4\pi DR_{ET} \left( 1 + \frac{R_{ET}}{\sqrt{\pi Dt}} \right) \quad (2.13)$$

where the following new *ET radius* has been introduced:

$$R_{ET} = 0.676 \left( \frac{R_0^6}{\sqrt{\tau D}} \right)^{1/4} \quad (2.14)$$

Since eq.(2.13) has the same form of the kinetic constant obtained for the diffusive mechanism, eq.(2.9), we can consider the combination of the two mechanism as a new *effective diffusion* process having a new contact radius defined by eq.(2.14) (see figure 2.2C). The Gosele's kinetic constant has been re-obtained starting from a more sophisticated treatment by Jang and collaborators [25].

### 2.1.5 The Exciton-Exciton Annihilation

Other than being the fundamental process through which excitation can move through the network, ET is responsible also for a relaxation mechanism through which excitations are depleted from the system. This phenomenon is referred to as *exciton-exciton annihilation* (EEA) and is considered to be due to an ET involving two excited donors. Indeed, when the excited donor relaxes to its GS, its excitation energy can be captured by another excited donor that is thereby promoted to a higher ES. But very energetic ESs are always close to several other states that normally provide non-radiative decay pathways through internal conversion processes. Therefore, after having promoted to a very energetic ES, the donor is likely to rapidly relax back it to the low-lwing ES. This process as a whole coincides with a net loss of excitations from the system (see figure 2.3). In pulsed time-resolved fluorescence experiments, straightforward evidence for the presence of EEA is the acceleration of the fluorescence signal decay upon increasing the power of the excitation light pulse (see figure 1.2C). Since powerful pulses excite a higher number of dyes, excitations become closer in space thereby increasing their annihilation probability.

The impact of EEA on the fluorescence decay has been studied using the Gosele's model by Lochbrunner and collaborators [26], who considered the following macroscopic equation for the donor exciton density

$$\frac{dC_D(t)}{dt} = -\frac{1}{\tau_D}C_D(t) - \frac{1}{2}k_{EEA}(t)C_D^2(t) \quad (2.15)$$

and introduced an EEA rate constant given by an annihilation Förster radius  $R_{D^*D^*}$  (in which it is highlighted that both donors are excited) having the same form of eq.(2.2) but with a spectral overlap expression calculated using the *excited state absorption* (ESA) spectrum of the donor:

$$k_{EEA}(t) \approx 4\pi DR_{EEA} \left( 1 + \frac{R_{EEA}}{\sqrt{\pi Dt}} \right) \quad (2.16)$$

$$R_{EEA} = 0.676 \left( \frac{R_{D^*D^*}^6}{\sqrt{\tau D}} \right)^{1/4} \quad (2.17)$$

$$R_{D^*D^*}^6 = \frac{9 \ln(10) \kappa^2 \Phi_D}{128 \pi^5 n^4 N_A} J_{ESA} \quad (2.18)$$

$$J_{ESA} = \int F_{norm}^D(\lambda) \epsilon_{ESA}^D(\lambda) \lambda^4 d\lambda \quad (2.19)$$

## 2.2 A New Macroscopic Models for Exciton Density Decay in RB Networks

### 2.2.1 Inclusion of EEA and Quenchers.

In this section, a new macroscopic model conceived to account for both the EEA and the presence of fluorescence quenching is proposed. The model has been developed to be directly applied for describing the experimental fluorescence decays of the LH NPs presented in section 1.2. In fact, both the EEA phenomena and the presence of quenchers (in particular RB dimers) occur when the LH systems are based on a network of RB dyes. Since the exact structure of the RB network within NPs cannot be experimentally determined, a homogeneous (or random) distribution of RBs is assumed and the Gosele model is used for describing both the EEA and quenching mechanisms. The time-dependent exciton density is determined by solving a system of two coupled differential equations, describing respectively the exciton density of RB (hereafter indicated as the excited donor, D) and its dimers (hereafter indicated as the quencher, Q):

$$\frac{dC_D(t)}{dt} = -\frac{1}{\tau_D}C_D(t) - \frac{1}{2}k_{EEA}(t)C_D^2(t) - k_Q(t)C_D(t)[C_Q^{tot} - C_Q(t)] \quad (2.20)$$

$$\frac{dC_Q(t)}{dt} = -\frac{1}{\tau_Q}C_Q(t) + k_Q(t)C_D(t)[C_Q^{tot} - C_Q(t)] \quad (2.21)$$

where  $C_Q^{tot}$  and  $\tau_Q$  are the total concentration of the quenching dimers and the non-radiative lifetime of the quencher respectively, and  $C_Q^{tot} - C_Q(t)$  is the concentration of relaxed

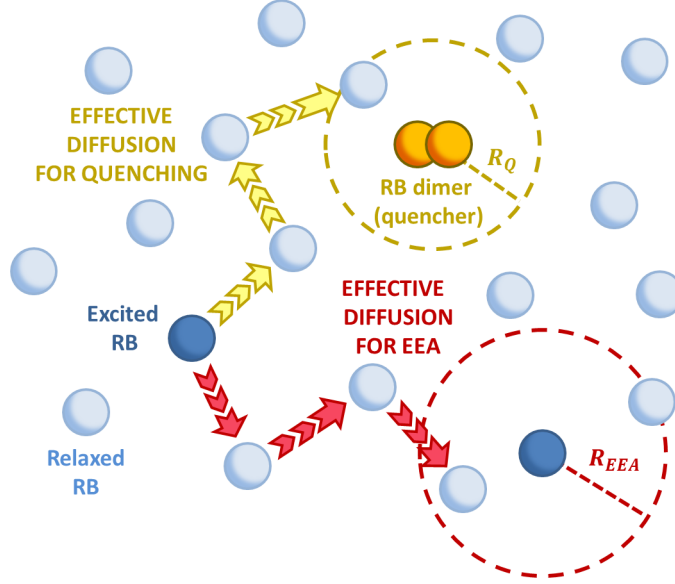


**Figure 2.4:** The two possible mechanisms for the exciton loss in RB networks. Within the framework of Gösele model, both EEA and quenching from RB dimers are described as effective diffusive mechanisms.

quenchers. The rate constant for the EEA is given by eq.s (2.16) and (2.17) while the rate constant for D-Q ET responsible for the RB fluorescence quenching is expressed in term of the quenching Förster radius  $R_{D^*Q}$ :

$$k_Q(t) \approx 4\pi DR_Q \left( 1 + \frac{R_Q}{\sqrt{\pi Dt}} \right) \quad (2.22)$$

$$R_Q = 0.676 \left( \frac{R_{D^*Q}^6}{\sqrt{\tau D}} \right)^{1/4} \quad (2.23)$$

Moreover, the diffusion accounting for the excitations mobility within the network is assumed to happen through a Förster hopping mechanism constituted by D-D ET steps. The diffusion coefficient for such a mechanism can be calculated as [27, 28]:

$$D = \eta \frac{R_{D^*D}^6}{\tau_D} \left( \frac{4}{3} \pi C_D^{tot} \right)^{4/3} \quad (2.24)$$

where  $C_D^{tot}$  is the total RB concentration,  $R_{D^*D}$  is the Förster radius describing the D-D ET (in which one donor is excited and the other is relaxed) and  $\eta = 0.43$  is a factor accounting for the homogeneous distribution of dyes.

To summarize, the RB exciton density describing the NPs' fluorescence decay is a function determined by three fundamental parameters, i.e. the Förster radii  $R_{D^*D}$ ,  $R_{D^*D^*}$ , and  $R_{D^*Q}$  describing the exciton diffusion, the EEA and the quenching from RB dimers, respectively. As a direct consequence of the Gösele model, both EEA and quenching are described as effective diffusive mechanisms, and the overall picture resulting from such a model is depicted in figure 2.4.

### 2.2.2 Investigating the Effect of Model Parameters

In this section, the effects of the parameters entering the macroscopic model presented in the previous section are analysed in detail. The polymeric LH NPs presented in ref. [2] have been considered as reference systems to which apply the macroscopic model, and NPs having a RB content equal to the 30% in weight have been considered as study case. The mean diameter of such NPs has been determined to be about 45 nm, and thus the corresponding RB concentration is  $C_D^{tot} = 0.13$  dyes/nm<sup>3</sup>. Since the dimerization extent cannot be experimentally determined, also the quencher concentration  $C_Q^{tot}$  is considered as a variable parameter. The dimerization still minimally persists within NPs despite the best efforts one can make to prevent it (i.e., the use of bulky counterions and long alkylic chains). Thus, only a slight amount of quencher is assumed to be present, i.e. not more of 1% of  $C_D^{tot}$ . Moreover, due to the lack of experimental information, also the quencher non-radiative lifetime  $\tau_Q$  is considered as a variable parameter. For the RB radiative lifetime, the value of  $\tau_Q = 4.24$  ns is considered (corresponding to the experimental value for the 0.1% loaded NPs reported in ref. [2], in which dimerization should be minimized).

The coupled equations (2.20) and (2.22) have to be solved by imposing certain initial conditions, including the exciton densities  $C_D(0)$  and  $C_Q(0)$  immediately generated by the pulse (at time zero). For the former, a value of 7% of  $C_D^{tot}$  (similar to values found for other systems [26]) is considered; for the latter, it is assumed that no quenchers are initially excited because dimers, due to the strong electronic coupling between monomers, presumably present a significantly shifted absorption maxima with respect to the isolated dyes, and since the pulse wavelength normally corresponds to the monomer absorption maximum, dimers are likely to present a very weak absorption at such a wavelength. The following analysis aims highlighting the various effects of the parameters entering the macroscopic model, emphasizing those features that could allow a straightforward identification of the presence of intruder quenching species. The system of coupled equations has been solved numerically by means of an in-house Python code employing the *scipy.integrate* package.

First of all, the effect of the  $R_{D^*D^*}$  and  $R_{D^*D}$  Förster radii, governing respectively the direct EEA and the exciton diffusion influencing both diffusive EEA and diffusive ET to the quenchers, is analysed. Since the typical radii are below 8 nm [20], values within the 3-6 nm range have been tested. To highlight the effect of EEA, the  $R_{D^*Q}$  radius governing the D-Q ET and the quencher concentration  $C_Q^{tot}$  are set to small values, i.e. 2 nm and 0.25% of  $C_D^{tot}$  respectively. From figure 2.5A, it is clear that  $R_{D^*D^*}$  has an influence on the decays only at short time, with the initial decay accelerating upon increasing the radius while leaving unaltered the long times evolution. This result indicates that EEA events following the direct mechanism start immediately after the light pulse and becomes less probable with time, as the spatially closed excitations are depleted through the annihilation. The influence of the  $R_{D^*D}$  radius is quite different from that of  $R_{D^*D^*}$ , as clearly shown in 2.5.B. Indeed,

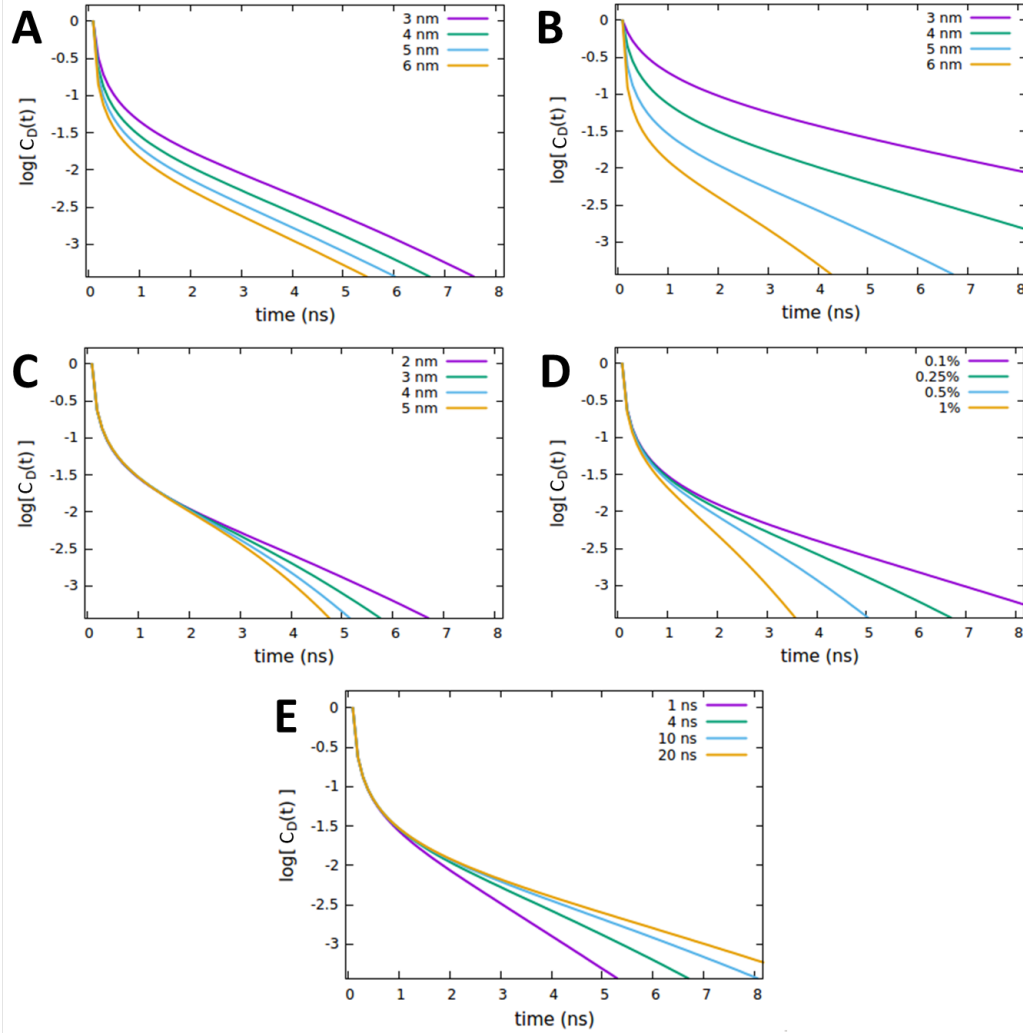


**Figure 2.5:** Effect of parameters entering the Gösele model on the (normalized) exciton density decay  $C_D(t)$  simulated for RB-based NPs.  $C_D(0)$  is assumed to be 7 % of  $C_D^{tot}$ . The quencher concentration  $C_Q^{tot}$  is always expressed as % of  $C_D^{tot}$ . **(A)** Effect of the  $R_{D^*D^*}$  radius governing the direct EEA mechanism. Fixed parameters are:  $R_{D^*D} = 5$  nm;  $R_{D^*Q} = 2$  nm;  $\tau_Q = 4$  ns;  $C_Q^{tot} = 0.25$  %. **(B)** Effect of the  $R_{D^*D}$  radius governing diffusive mechanisms. Fixed parameters are  $R_{D^*D^*} = 4$  nm;  $R_{D^*Q} = 2$  nm;  $\tau_Q = 4$  ns. **(C)** Effect of the  $R_{D^*Q}$  radius governing the direct quenching mechanism. Fixed parameters are  $R_{D^*D^*} = 4$  nm;  $R_{D^*D} = 5$  nm;  $\tau_Q = 4$  ns;  $C_Q^{tot} = 0.25$  %. **(D)** Effect of the quencher concentration  $C_Q^{tot}$ . Fixed parameters are  $R_{D^*D^*} = 4$  nm;  $R_{D^*D} = 5$  nm;  $R_{D^*Q} = 2$  nm;  $\tau_Q = 4$  ns. **(E)** Effect of the quencher lifetime  $\tau_Q$ . Fixed parameters are  $R_{D^*D^*} = 4$  nm;  $R_{D^*D} = 5$  nm;  $R_{D^*Q} = 2$  nm;  $C_Q^{tot} = 0.25$  %.

it affects both the short and long times evolution, and while the influence on the short times is similar to  $R_{D^*D^*}$ , here also the long time decays are accelerating upon increasing the radius.

Considering now the effect of the parameters related to the quencher species, i.e. its Förster radius  $R_{D^*Q}$ , concentration  $C_Q^{tot}$  and radiative lifetime  $\tau_Q$ , which are reported in figures 2.5C, 2.5D, and 2.5E respectively. It is evident that when the quencher is present in a small amount, its influence can affect the long times evolution only, since the few quencher molecules are very far from the majority of excited dyes and then a certain time has to pass to allow excitations to diffuse towards them. Since this specific (isolated) effect on the long-time evolution cannot be obtained by varying the parameters related to the EEA, it represents a straightforward signature for the presence of intruder quenching species.

Figure 2.6A shows how the exciton density decay is effected by the increase of the initial exciton density, which can be associated to the increase of the experimental light source power. Such an increase leads to the typical decay acceleration experimentally observed and normally imputed to the presence of EEA (see figure 1.2 for comparison). In order to establish whether the initial exciton density could affect the parameters effect discussed above, the initial value  $C_D(0) = 25\%$  of  $C_D^{tot}$  has been also tested. The corresponding decays and their comparison with results obtained by using  $C_D(0) = 7\%$  are reported in the other panels of figure 2.6, from which is evident that the higher  $C_D(0)$  value has the effect of accelerating the short time decay while leaving unaltered the long time behaviour. Therefore, also in this case the presence of quenchers can be straightforwardly associated to long time effects, which can thus be considered as the dimers' quenching fingerprint regardless of the  $C_D(0)$  value.

### 2.2.3 Toward a Reliable Fitting of Experimental Fluorescence Decays

When tested for fitting certain trial exciton density decays, the macroscopic model given by equations (2.20) and (2.22) has turned out to be an extremely flexible tool, being for example able to fit a given decay even by fixing up to two parameters and providing very good fits independently from the chosen couple of parameters and the fixed values (obviously within a reasonable range of values). Clearly, such flexibility has to be ascribed to the large number of parameters employed, including the  $R_{D^*D^*}$ ,  $R_{D^*D}$  and  $R_{D^*Q}$  Förster radii and the quencher concentration  $C_Q^{tot}$  and lifetime  $\tau_Q$ . Thus, to make applications bringing real physical information, one should experimentally and/or theoretically determine the highest number of parameters. For example, the  $R_{D^*D}$  radius can be straightforwardly obtained from the overlap between the RB absorption and emission spectra, while  $R_{D^*D^*}$  could be obtained from the overlap between the RB excited state absorption (ESA) and emission spectra. The latter is less straightforward than obtaining  $R_{D^*D}$  due to the fact that ESAs often overlaps with ground state bleaching and stimulated emission signals. In this context, advanced simulations of nonlinear electronic spectroscopy from first-principles (developed by other researchers in our research group) would be of great support to apply the presented model to real systems. Finally, regarding parameters associated to the RB quenching dimers, first-principles simulations would also be crucial to estimate the  $R_{D^*Q}$  radius, especially if dimers cannot be isolated and their absorption spectra recorded. Using structural models for these aggregates, indeed, absorption and emission spectra could be simulated and their

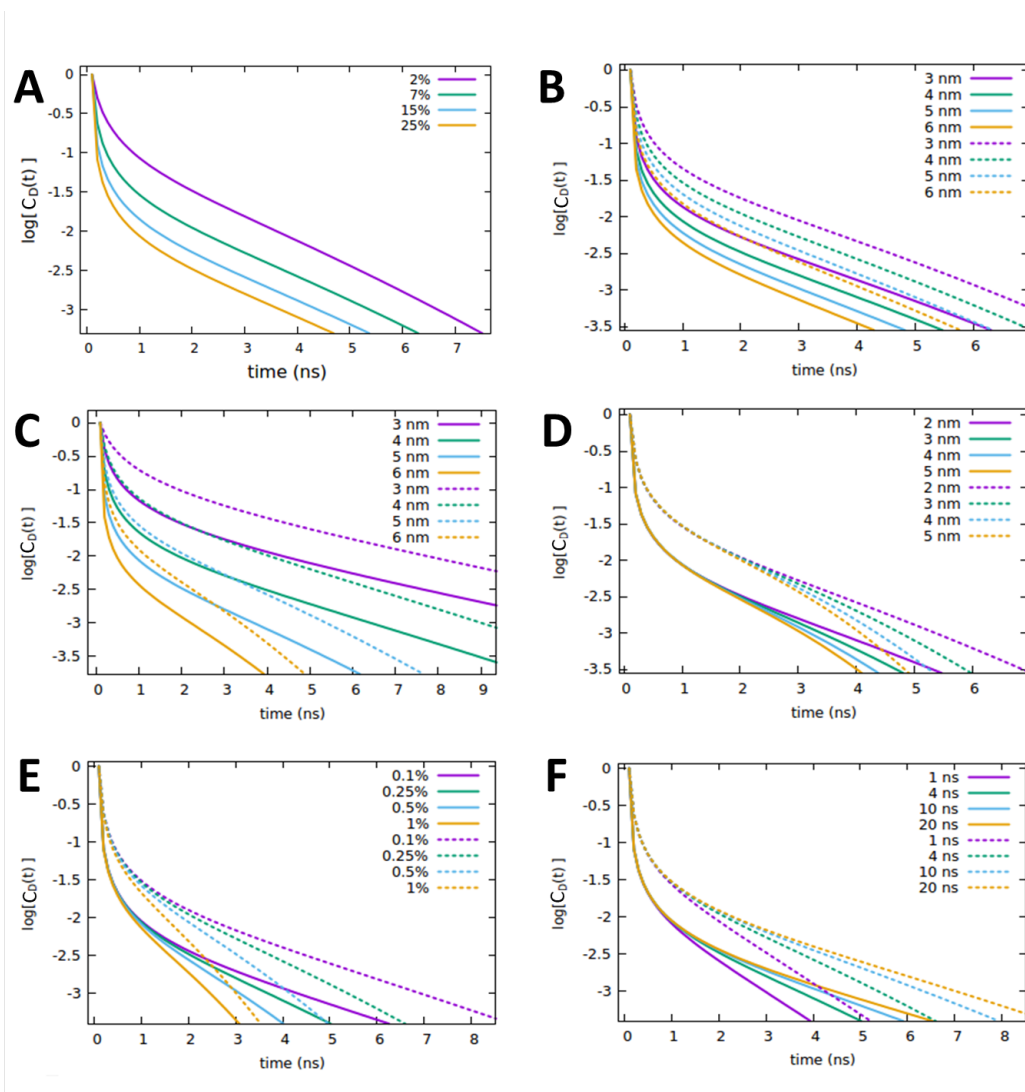


**Figure 2.6:** (A) Effect of the initial exciton density on the (normalized) exciton density decay  $C_D(t)$  simulated for RB-based NPs. (B-F) Effect of the parameters on the decay obtained for  $C_D(0) = 25\%$  of  $C_D^{tot}$  (full lines) and  $C_D(0) = 7\%$  (dotted lines). The quencher concentration  $C_Q^{tot}$  is always expressed as % of  $C_D^{tot}$ , and fixed parameters are the same reported in figure 2.5. (B) Effect of the  $R_{D^*D^*}$  radius governing the direct EEA mechanism. (C) Effect of the  $R_{D^*D}$  radius governing diffusive mechanisms. (D) Effect of the  $R_{D^*Q}$  radius governing the direct quenching mechanism. (E) Effect of the quencher concentration  $C_Q^{tot}$ . (F) Effect of the quencher lifetime  $\tau_Q$ .

Förster radius estimated. In such a way, one could restrict the set of fitting parameters to the quencher concentration and lifetime only, the values of which provide fundamental insights into the role of aggregation within the LH NPs.



## Chapter 3

# Molecular Dynamics Simulation of Rhodamine B Aggregation in Water

### 3.1 Theoretical Background: Molecular Mechanics and Molecular Dynamics

The *Molecular Mechanics* (MM) is a computational methodology aimed to calculate the energy of highly extended systems (spanning from large biomolecules such as proteins to whole solutions including thousands of solute and solvent molecules) that are obviously out of reach through QM methods. The fundamental idea underlying MM, which does not treat explicitly the quantistic nature of the electronic structure of atoms and molecules, is to treat atoms as pure classical particles and to describe molecules by a simple “balls and springs” model. Interactions between atoms are typically parametrized basing on QM calculations by assuming their transferability, i.e. two atoms of a given kind (for example, the C and O atoms constituting a carbonylic group) are assumed to interact in the same manner independently from the molecule to which they belong. The list of parameters defining all possible interactions between all possible atom kinds (i.e., the MM energy) is normally referred to as the *Force Field* (FF), in the sense that the set of atom’s positions and their classification in different *atom types* automatically determine the whole set of forces (which in turn determine the corresponding interaction energies) exerted on each atom by all the others. The MM model not only extremely simplifies the calculation of the energy with respect to QM methods, but also allow also to perform *Molecular Dynamics* (MD) simulations with a excellent computational cost. In MD simulations, each atom’s position evolves in time basing on the classical Newton’s equation of motion directly dictated by the forces arising from the FF.

### 3.1.1 Energy Calculation in Molecular Mechanics

The FF energy is partitioned as the following sum of independent terms [83]:

$$E_{FF} = E_{str} + E_{bend} + E_{tors} + E_{vdW} + E_{el} \quad (3.1)$$

where the first three terms represent the *bonding* interactions, which concern only atoms directly connected by chemical bonds, while the last two terms represent the *non-bonding* interactions, concerning all atoms and calculated as sums of two-body interactions.

The first term accounts for the bond *stretching* energy and is typically assumed to be described by an harmonic potential:

$$E_{stretch} = \frac{1}{2} \sum_{AB} k_{AB}^{str} (r_{AB} - r_{AB}^0)^2 \quad (3.2)$$

where the sum runs over the A-B couples of atoms directly bonded,  $r_{AB}$  is the bond length,  $r_{AB}^0$  is the associated equilibrium value and  $k_{AB}^{str}$  is the force constant governing the stretching.

The second term accounts for the *bending* energy and is also typically assumed to be described by an harmonic potential:

$$E_{bend} = \frac{1}{2} \sum_{ABC} k_{ABC}^{bend} (\theta_{ABC} - \theta_{ABC}^0)^2 \quad (3.3)$$

where the sum runs over the A-B-C triplets of atoms consecutively bonded,  $\theta_{ABC}$  is the A-B-C angle,  $\theta_{ABC}^0$  is the associated equilibrium angle and  $k_{ABC}^{bend}$  is the force constant governing the bending.

The third term accounts for the *torsional* energy, and being the energies of each A-B-C-D torsion periodic functions of the associated dihedral angles  $\phi_{ABCD}$ , they can be generally expressed in form of Fourier series:

$$E_{tors} = \frac{1}{2} \sum_{ABCD} \sum_{n=1}^N V_n^{ABCD} \cos(n\phi_{ABCD}) \quad (3.4)$$

where the sum runs over the A-B-C-D quartets of atoms consecutively bonded, the  $n$  values indicate the terms accounting for different periodicities ( $n = 1$  describes the contribution periodic by  $360^\circ$ ,  $n = 2$  describes the contribution periodic by  $180^\circ$ ,  $n = 3$  describes the contribution periodic by  $120^\circ$  and so on) and  $V_n$  are the corresponding amplitudes.

The fourth term accounts for the *van der Waal* interactions, for which the *Lennard-Jones* (LJ) potential [29] is normally employed:

$$E_{vdW} = \frac{1}{2} \sum_{A,B} 4\varepsilon_{AB} \left[ \left( \frac{\sigma_{AB}}{r_{AB}} \right)^{12} - \left( \frac{\sigma_{AB}}{r_{AB}} \right)^6 \right] \quad (3.5)$$

where the sum runs over all the atom couples separated by at least three bonds and the positive and negative terms represent the repulsive and attractive interactions, respectively.

Here, the  $\sigma_{AB}$  and  $\varepsilon_{AB}$  parameters represent the vdW equilibrium distance and interaction strength, respectively, which are in turn calculated starting from single atom parameters as

$$\sigma_{AB} = \sigma_A + \sigma_B \quad (3.6)$$

$$\varepsilon_{AB} = \sqrt{\varepsilon_A \varepsilon_B} \quad (3.7)$$

Finally, the last term accounts for the *electrostatic* energy, which is calculated by using atomic charges normally obtained from QM calculations:

$$E_{vdW} = \frac{1}{2} \sum_{A,B} \frac{Q_A Q_B}{\varepsilon r_{AB}} \quad (3.8)$$

where the sum runs over all the atom couples separated by at least three bonds and  $\varepsilon$  is the dielectric constant of the medium.

### 3.1.2 Equations of Motion and Different Ensembles in Molecular Dynamics

The time-dependent evolution of the system is simply dictated by the set of Newton's equations governing the motion of each atom through the force generated by the FF on it:

$$\mathbf{F} = -m\mathbf{a} = -\frac{dE_{FF}}{d\mathbf{r}} \quad (3.9)$$

All the methods that have been proposed for the numerical integration of eq.(3.9), in which the time is discretized in a sequence of *time steps*  $\Delta t$ , are based on the calculation of positions, velocities and accelerations at a given time step from their values at previous time steps. The most widely used is probably the *Verlet Velocity* algorithm [30], in which the equations used for propagating the atoms read

$$\mathbf{r}_{i+1} = \mathbf{r}_i + \mathbf{v}_i \Delta t + \frac{1}{2} \mathbf{a}_i \Delta t^2 \quad (3.10)$$

$$\mathbf{v}_{i+1} = \mathbf{v}_i + \frac{1}{2} (\mathbf{a}_i + \mathbf{a}_{i+1}) \Delta t \quad (3.11)$$

where the subscript  $i$  and  $i+1$  are shortcuts for indicating the time dependence, i.e.  $\mathbf{r}_i = \mathbf{r}(t_i)$  and  $\mathbf{r}_{i+1} = \mathbf{r}(t_i + \Delta t)$ .

The standard resolution of the equations of motion generates the so-called NVE ensemble, in which (other than the number of atoms N) the volume and the energy are the quantities that are conserved during the dynamics. One is usually be interested in considering different statistical ensembles, in particular the NVT having constant volume and temperature or the NPT having constant volume and pressure. Regarding the NVT ensemble, since the temperature is directly proportional to the kinetic energy of the system, an efficient way for regulating the temperature throughout the simulation without affecting the results is to scale all the atomic velocities by an equal factor at each time step. A very popular scaling method is the so-called *Berendsen thermostat* [31], which considers a thermal bath coupled to the system via a coupling parameter that is used to determine the scaling factor. Regarding

instead the NPT ensemble, the pressure regulation can be readily achieved by modifying the volume of the system through the uniform scaling of all atomic coordinates, and a popular method is the *Berendsen barostat* that consider a “pressure bath” (conceptually similar to the thermal one) characterized by a coupling parameter that, along with the compressibility of the system, is used to determine the scaling factor.

### 3.2 Simulating Rhodamine B Aggregation in Water

In Section 1.2, it has been discussed how the combination of the alkylated RBs with the bulky and hydrophobic F5TPB counterion can be exploited to form RB networks where the capability of F5TPB to act as a spacer among dyes prevents the formation of quenching stacked dimers. Such extremely important feature of F5TPB has been observed not only in polymeric LH NPs, but also in solution (i.e. in absence of polymer). Indeed, when added to aqueous RB solutions, F5TPB provokes the formation of colloidal NPs constituted by a clustering of  $\text{RB}^+$  and  $\text{F5TPB}^-$  ions [5] showing the same efficient ET observed in polymeric NPs.

Achieving insights on RBs arrangements within the dye networks is very challenging from an experimental point of view. If the presence of blinking could support the picture of an arrangement in which the dyes are quite close each other and an estimate of the mean dye-dye distance can be inferred from spectroscopic measurements, such as the fluorescence anisotropy decay [2], atomistic details of the network structure are completely out of reach experimentally. Therefore, MD simulations (which have been already used to successfully simulate the RB absorption on clay minerals [32], graphene [33] and membranes [34]) can surely be helpful in providing fundamental information about the structural features affecting the efficiency of ET in these systems.

In the following sections, it is presented and tested a FF for the modelling of self-assembling in RB/F5TPB systems in water solution based on the widely used Generalized Amber Force Field (GAFF) [35]. A full parametrization for the RB unit and an *ad hoc* refinement of the RB LJ parameters has been performed, aiming at a reliable reproduction of the RB-RB interactions, using as reference *Density Functional Theory* (DFT) calculations (see Section 4.1.2 for theoretical detail about the method). The FF reliability is judged on its ability to reproduce experimental studies on the influence of counterion type and of alkylic RB substituents reported by Shulov et al. [5], showing that (when a small, ethyl alkyl chain is considered) the F5TPB and the  $\text{I}^-$  counterions induce quite different aggregation of RB units in water.

In what follows, all DFT calculations have been performed using the Gaussian 16 software [36] with the B3LYP functional by using D3 Grimme’s empirical dispersion (see Sections 4.1.2 and 4.1.6 for details) and the 6-311+G\* basis set, while all MD calculations have been performed using the NAMD software [37].

#### 3.2.1 Force Field Parametrization

The FF parameters for RB ethyl ester (for simplicity named as RB in this Chapter) have been obtained with the procedure described below.

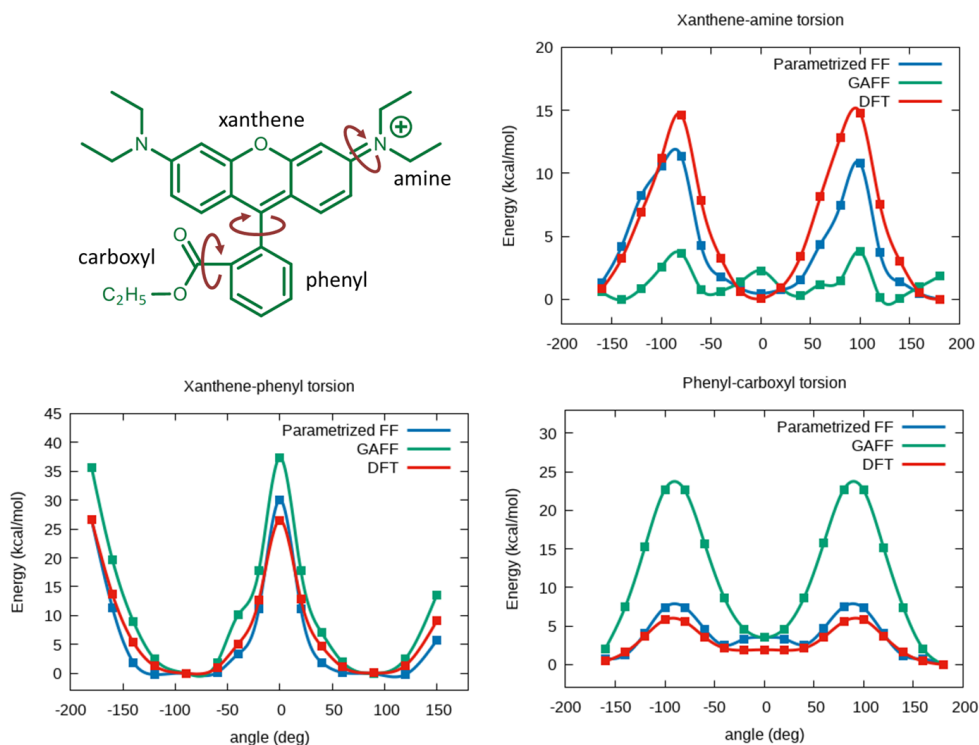


**Figure 3.1:** RB dihedral angles selected for parametrization and corresponding potential energy profiles calculated with the original and modified GAFF force fields, compared with DFT (B3LYP-D3/6-311+G<sup>\*</sup>) calculations used as reference. The MM energy of each point is calculated at the DFT optimized geometry.

Firstly, DFT calculations have been used to optimize the geometry and calculate the corresponding ESP charges. In order to evaluate if the standard GAFF parameters provide a reliable ground state (GS) structure of RB in vacuum, the DFT optimized geometry and the MM one (involving GAFF standard parameters and ESP charges) have been compared. Since several bonds of the xanthene moiety were found at the MM level to deviate for more than 0.01 Å (up to 0.04 Å) with respect to DFT, new atom types to describe all xanthene atoms have been defined (see Appendix) and replaced the equilibrium bond distances with the DFT ones, leaving unaltered the GAFF force constants.

Secondly, the MM parameters of the xanthene-phenyl, xanthene-amine and phenyl-carboxyl torsional potentials have been adjusted, as reported in Figure 3.1. For each dihedral, the potential energy surface (PES) for the torsions has been calculated at DFT level by constrained scans, i.e. evaluating the GS total energies every 10° of the selected dihedral angles and allowing relaxation of all the remaining internal coordinates. The corresponding free energy profiles at MM lever were obtained with the *adaptive biasing force method* [38], using the different dihedrals as collective variables in NVT simulations of a single RB con-

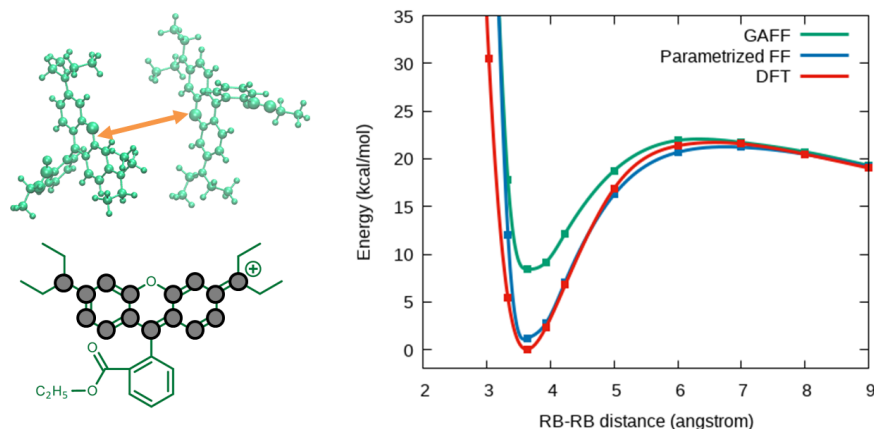


**Figure 3.2:** Lennard-Jones parametrization for the RB-RB interaction in forming a stacked H dimer. On the left, representation of a H dimer (top) and RB chemical structure (bottom) where the grey circles correspond to atoms for which the LJ parameters have been modified. On the right, the intermolecular energy is reported as a function of the xanthene-xanthene inter-plane distance (indicated by the arrow).

ducted at 300 K. The force field parameters were iteratively modified until the DFT PESs and the MM free energy profiles coincided within an error of 0.1 kcal/mol in the region of the minima (see ref.[39] for further details on the method). Clearly, the parameterization resulted to be crucial for the phenyl-carboxyl torsions, since the original GAFF predicted quite large torsional barriers. Notably, the opposite trend is observed for the xanthene-amine rotation. These behaviours probably arise from the fact that GAFF parametrization is performed on a database of neutral molecules, and likely the standard torsional parameters are inadequate for describing the torsions in charged aromatic systems like RB.

Finally, in order to correctly describe the dimerization of two positively charged RB molecules, a parametrization of the van der Waals interactions for two approaching RB molecules has been also performed. Taking as reference case the formation of a stacked H dimer, the LJ parameters of the xanthene atoms have been adjusted until the interaction energy given by the DFT calculations using Grimme’s dispersions is recovered. To calculate the PES related to two RB molecules approaching to form the stacked H dimer, the dimer’s geometry optimized in vacuum at the DFT level has been considered and the RB-RB distance has been varied leaving unchanged both monomer geometries. At each distance the DFT and MM total energies have been computed (all calculations were performed in vacuum). The PES obtained in such a way is reported in Figure 3.2: being RBs positively charged, one clearly sees that to form a dimer, stabilized by the van der Waals interactions, the two dyes firstly must overcome a potential energy barrier related to the Coulomb repulsive interaction. It is immediately evident that GAFF, although reproducing qualitatively the DFT profile,

underestimates the PES minimum energy of about 50% with respect to DFT. To correct for such a discrepancy, the  $\epsilon$  parameters of eq.(3.7) describing the vdW interactions among the atoms belonging to xanthene moiety have been uniformly scaled until the QM PES was correctly reproduced: a good agreement has been found upon doubling those parameters.

Regarding the MM parameters of the counterions, the standard GAFF parameters have been used for iodide ions while for the F5TPB molecule a minimal refinement have been performed: indeed, a fine parametrization for the F5TPB flexibility is not strictly required because the high symmetry of F5TPB combined with its almost spherical shape makes its bulkiness largely independent from the intramolecular motions. In particular, we computed the F5TPB minimum energy structure with DFT in vacuum and the corresponding equilibrium distance and force constant for the B-C stretching have been incorporated in the FF, while for bending and torsions angles involving boron we took the parameters for tetraphenyl methane from the literature [41]. The vdW parameters for the B atoms were also taken from ref.[41]. The complete set of modified parameters for RB and F5TPB is reported in Appendix.

For water molecules, which parameters are used in the MD simulations discussed below, the flexible variant of the simple point charge model (spc/fw) [40] was employed, since it well reproduces the dynamical and dielectric properties of bulk water.

### 3.2.2 Molecular Dynamics Simulations: Computational Methodology

Three independent MD simulations of RB molecules in water have been performed in presence of either F5TPB or I<sup>-</sup> as counterion. The simulation boxes were created using the Packmol package [42], containing 10 RB dyes and 10 F5TPB (or iodide) counterions within a cubic box with side length of 85 Å. The box dimensions were chosen such that all RB-RB distances in the initial configurations largely overcome the value of 7 Å, which is the distance at which the attractive potential between two RBs starts (see PES reported in Figure 3.2). It is worth noting that the experimental RB concentrations used in ref.[5] are much smaller than those considered in the MD simulations. This is due to the fact that MD simulations will be computationally unfeasible at the experimental concentrations, as they would require very large box dimensions and, consequently, a huge number of solvent molecules.

For each simulation, a time step of 1 fs was used, the cutoff for LJ and direct space electrostatic was set to 12 Å and the *Particle Mesh Ewald* method for the electrostatics was used by setting a grid spacing of 1.5 Å. The temperature and pressure equilibrations have been carried through 1 ns of thermal equilibration (in the NVT ensemble at 300 K) followed by 2 ns of pressure equilibration (in the NPT ensemble at 1 atm) using the Berendsen barostat. After the equilibration steps, the MD simulations were performed in the NVT ensemble for 20 ns.

To quantify the dimerization extent, each RBs couple in which the centre-centre distance between the xanthene planes ( $r_{CC}$ ) falls below the cutoff value of 6 Å has been considered as a dimer. Such a cutoff, which more or less corresponds to the distance at which the RB-RB interaction starts to be attractive in the stacked dimer in vacuum (see Figure 3.2), ensures to exclude those RB couples that could involve the presence of a F5TPB counterion (or a part of it, such as one of its phenyl groups) in between the two RB units. Moreover, considering that RB transition dipole moment lies on the xanthene plane and parallel to

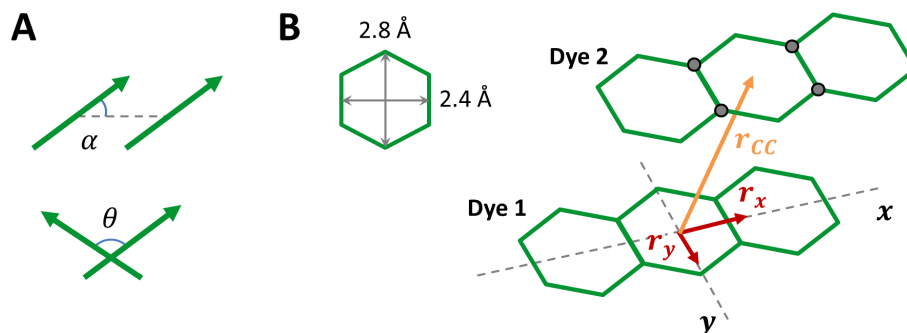


**Figure 3.3:** (A) Angles among the transition dipole moments of RB molecules employed for the classification in H ( $0^\circ < \theta < 12^\circ$ ;  $54.7^\circ < \alpha < 90^\circ$ ), J ( $0^\circ < \theta < 12^\circ$ ;  $\alpha > 54.7^\circ$ ) and crossed J ( $\theta > 12^\circ$ ) dimers. (B) Representative dimensions of the hexagonal units of the xanthenes plane and parameters employed for individuating the  $\pi$ -stacked dimers: the cutoffs for the components of the  $r_{CC}$  vector (calculated with respect to the molecular  $x$  and  $y$  axes of dye 1) are set to 4 Å for  $r_x$  and 2 Å for  $r_y$ , while the cutoffs for the distances separating the 4 central atoms of the dye 1 (labelled with gray circles) and the  $xy$  xanthenes plane of dye 2 is set to 4.5 Å.

its long axis, dimers have been classified as H, J and crossed J dimers depending on the reciprocal orientation of the xanthenes axes of each RB: as reported in Figure 3.3.A, parallel dimers are defined as those having  $0^\circ < \theta < 12^\circ$  and crossed J dimers those having  $\theta > 12^\circ$ , while for parallel dimers the angle  $\alpha$  is used to classify them as H ( $54.7^\circ < \alpha < 90^\circ$ ) or J ( $\alpha > 54.7^\circ$ ).

Another relevant feature to monitor is the formation of H  $\pi$ -stacked dimers, because they are expected to act as fluorescence quenchers. The  $\pi$ -stacked dimers are defined basing on a combination of the geometrical parameters depicted in Figure 3.3.B: the  $x$  and  $y$  components of  $r_{CC}$  have to fall within the cutoffs of 5 and 2 Å respectively, and the distances separating the 4 central atoms of one first monomer from the xanthenes plane of the second have to fall each within the cutoff of 4.5 Å (the xanthenes-xanthenes distance for a stacked H dimer predicted at the DFT level of theory is about 3.5 Å). In order to evaluate the formation of RB-RB clusters within NPs eventually involving also the counterions, the trajectory for the sum of the modules of  $r_{CC}$  vectors has been determined.

### 3.2.3 Molecular Dynamics Simulations: Results

Figures 3.4 and 3.5 show the results of three independent MD simulations carried out for each of the counterions considered, F5TPB and iodide respectively, using the re-parametrized FF. In particular, the numbers of H, J and crossed J dimers (in both generic and stacked conformations) formed along the MD trajectories (extracting one frame every 1 ps) are reported as simple moving average considering time intervals of 0.1 ns. The time evolutions of the sum of the dye-dye distances ( $R_{CC}$ ), being a useful parameter for qualitative evaluation

of the aggregations involving a large number of RB, i.e. this distance decreases when large aggregates are formed, is also reported. Representative snapshots reporting the typical structure of RB aggregates are depicted in Figure 3.6.

The most straightforward result is that only the F5TPB counterion can drive the formation of large aggregates involving basically all the RBs included in the simulation. This extensive clustering (see dropping of the sum of dye-dye distances in Figure 3.4) is in line with the NPs formation experimentally observed in ref. [5]. Despite conclusions out of this outcome inevitably suffer of limitations with respect to realistic experimental conditions (i.e. larger concentration and aggregates with reduced number of dyes in the simulations compared to experiments), they provide important insights at the atomistic level and interesting trends as a function of the counterion involved. Indeed, when the iodide counterion is considered, dimers formation is still observed (including crossed J stacked dimers) but formation of large RB or RB/iodide aggregates is not, see Figure 3.5 (where the sum of dye-dye distances is constantly large along all MD simulations). These results are also in line with the absence of RB NPs formation found in experiments [5] and, notably, such RB aggregates are not formed in presence of iodide despite the large concentration employed in our MD simulations. Interestingly, in the three MD simulations with F5TPB counterion, it is observed the formation of both a single RB/F5TPB aggregate comprising almost all RBs (namely a 'full aggregate', see MD2) and two separated aggregates (MD1,3), see Figure 3.6, allowing structural characterization of the formed dimers with atomistic resolution, as discussed below.

Other than inducing the spontaneous aggregation of RB, it is clearly observed the ability of the F5TPB counterion of acting as a spacer between RB monomers within the aggregate, preventing the H dimerization responsible for the fluorescence quenching. Indeed, another striking result is that despite the formation of large RB/F5TPB aggregates, the formation of stacked dimers is quite limited and the appearance of H dimers is a rather rare event. In particular, while up to 4 RB dimers (out of 5 potentially forming with the 10 RB monomers considered) are formed within large RB/F5TPB aggregates (see Figure 3.4), only 1 (and rarely 2) among them can be really considered as  $\pi$ -stacked, generally being of the crossed J type. In fact, one stacked H dimer stable enough to persist for about 1 ns has been observed only in one of the three replicas and when a full aggregate is formed (i.e. in MD 2, see Figure 3.4). It is worth mentioning that such results are obtained despite the parameterization for the RB-RB LJ interaction is based on the correct description for the formation of a stacked H dimer. Thus, the simulations strongly suggest that within large RB/F5TPB aggregates no preferences for the parallel stacking of RB exists, in full agreement with experimental evidence and corroborating the role of F5TPB counterion as spacer that avoid fluorescence quenching of RB aggregates while maintaining good spacing for energy transfers between RB dyes.

In order to evaluate the effect of our parametrization with respect to standard GAFF, three GAFF simulations have been performed, two with the F5TPB and one with the iodide counterions, as shown in Figure 3.7. It is found that the large clustering in presence of the F5TPB counterion is partially predicted by GAFF, with observed formation of two large aggregates, while a full aggregate comprising all RBs is not found. The absence of large RB clustering in presence of iodide, instead, is very similar in GAFF and re-parametrized FF along with the formation of RB dimers in solution and the presence of crossed J stacked

## MD Simulation of RB Aggregation in Water

---

dimers. However, regarding the characterization of dimers' structure in RB/F5TPB aggregates, much less dimerization of RB units is observed when the GAFF is used and very few stacked dimers are formed if compared with the re-parametrized FF. This suggests that, as expected from the potential energies shown in Figure 3.2, the fine re-parametrization has the effect of encouraging the RB-RB interaction and, in particular, the formation of  $\pi$ -stacked RB dimers.

In conclusion, the formation of RB/counterion full aggregates only in presence of F5TPB and the rare (and transient) appearance of H dimers (despite the significant number of stacked J dimers) within large RB/F5TPB aggregates are predictions of the re-parametrized FF that represent a great improvement towards the characterization with atomistic resolution of RB aggregation processes in solution.

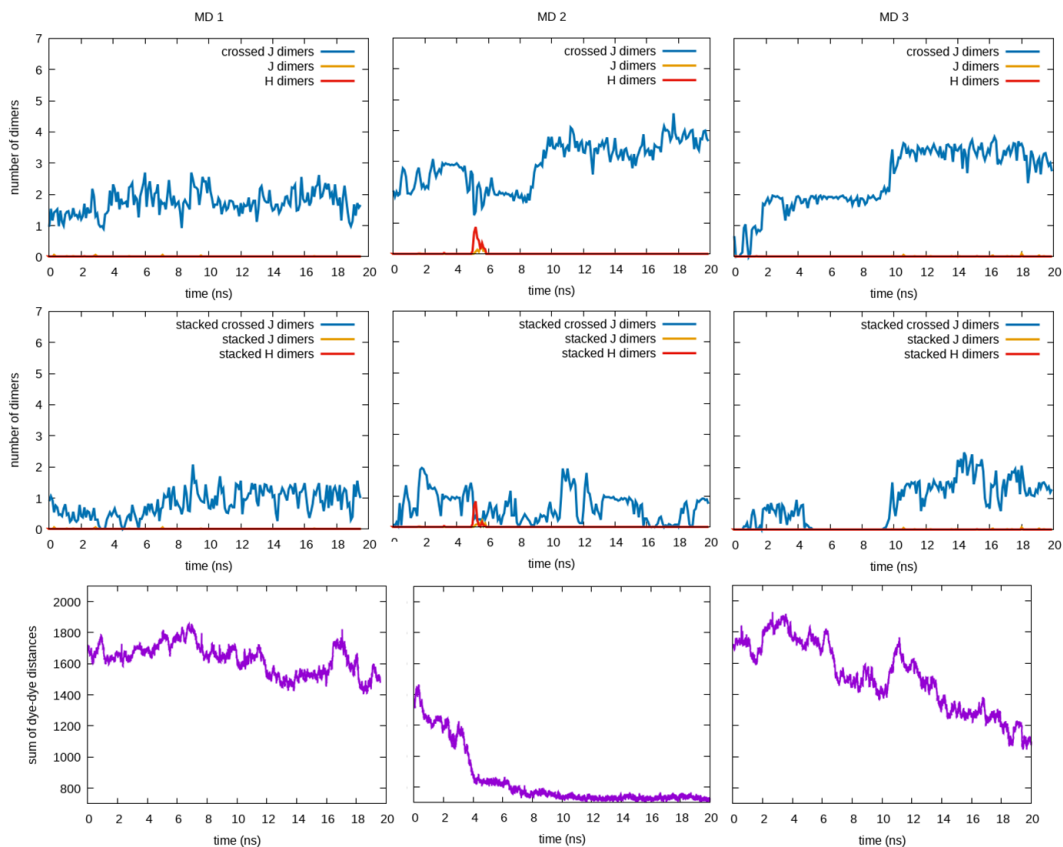


**Figure 3.4:** Results of three MD simulations carried out in presence of the F5TPB counterion. The first row shows the time evolution of the number of generic dimers, the second the time evolution of the number of  $\pi$ -stacked dimers and the third the time evolution of the sum of dye-dye distances. The time evolution of the number of H, J and crossed J dimers in both generic and stacked conformations is reported as the mean number of dyes formed within time intervals of 0.1 ns.

## MD Simulation of RB Aggregation in Water

---

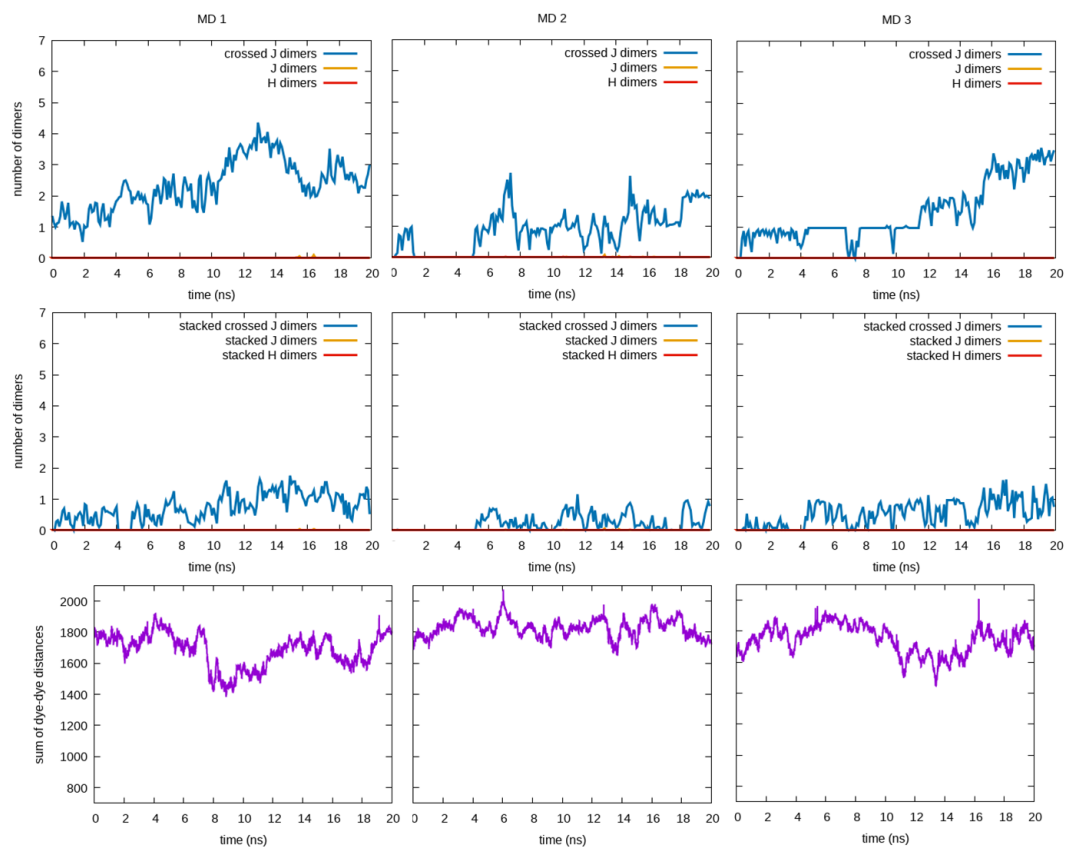


**Figure 3.5:** Results of three MD simulations carried out in presence of the iodide counterion. The first row shows the time evolution of the number of generic dimers, the second the time evolution of the number of  $\pi$ -stacked dimers and the third the time evolution of the sum of dye-dye distances.

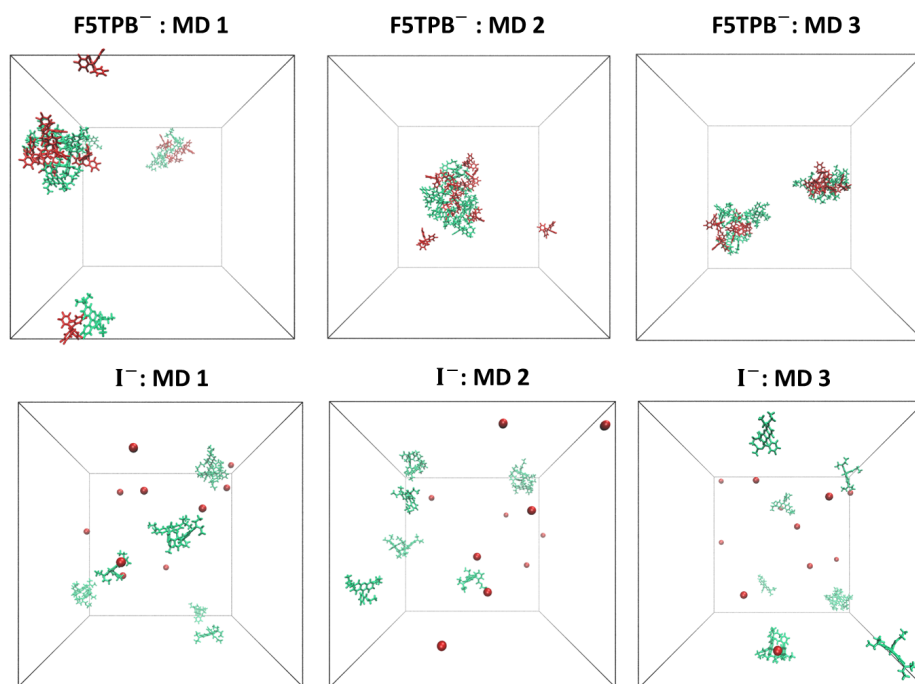


**Figure 3.6:** Representative snapshots from the MDs of Figures 3.4 and 3.5 recorded after 20 ns of dynamics (RB molecules are depicted in green, counterions in red and solvent molecules are omitted for clarity).

## MD Simulation of RB Aggregation in Water

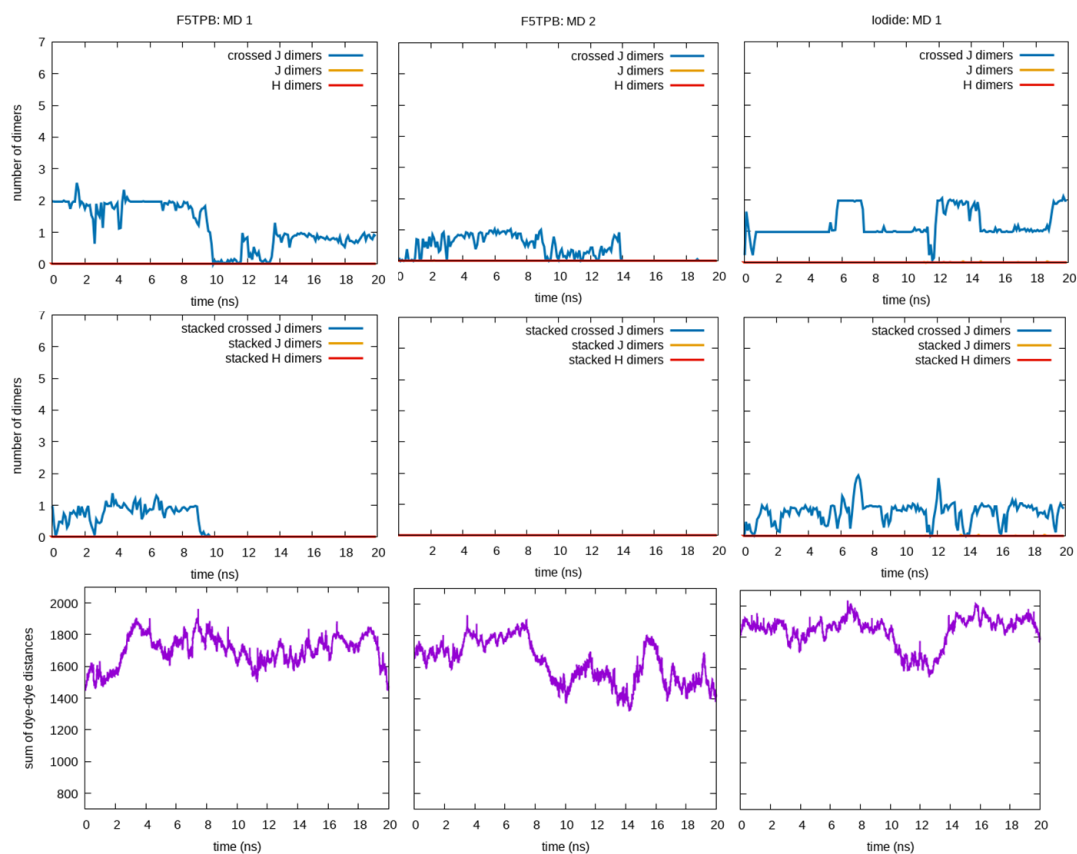


**Figure 3.7:** Results of MD simulations carried out by using the original GAFF in presence of F5TPB (1<sup>st</sup> and 2<sup>nd</sup> columns) and of the iodide (3<sup>rd</sup> column) counterions. The first row shows the time evolution of the number of generic dimers, the second the time evolution of the number of  $\pi$ -stacked dimers and the third the time evolution of the sum of dye-dye distances.

## Chapter 4

# Density Functional Theory Studies of Rhodamine B and Its Dimers

### 4.1 Theoretical Background: Density Functional Theory for Electronic-Structure Calculations

#### 4.1.1 Wavefunction Description of Electronic-Structure: the Schrödinger Equation

##### The Wavefunction and Its Properties.

In quantum mechanics (QM), the electronic structure of a molecule composed of  $N$  electrons is assumed to be completely described by a certain *wavefunction*  $\Psi(\mathbf{q}, t)$  expressed as a time dependent complex function of the spatial and spin coordinates of the particles, namely  $\mathbf{q} = \mathbf{q}_1, \mathbf{q}_2, \dots, \mathbf{q}_N$  with  $\mathbf{q}_i = \mathbf{r}_i, s_i$ , where  $\mathbf{r}$  and  $s$  represent the cartesian and spin coordinates (that is, the spin quantum number  $+1/2$  or  $-1/2$ ), respectively. The physical meaning of the wavefunction [43] is given by the product  $\Psi^*(\mathbf{q}, t)\Psi(\mathbf{q}, t)$ , a real quantity representing the probability density of finding the particle 1 in the position  $\mathbf{r}_1$  with spin quantum number  $s_1$ , the particle 2 in the position  $\mathbf{r}_2$  with spin quantum number  $s_2$  and so on.

The wavefunction has to respect two fundamental principles of QM, that is, the *indistinguishability principle*, which establishes that electrons cannot be enumerated or identified in any way, and the *antisymmetry principle* [44], which requires the wavefunction to be *antisymmetric* with respect to the interchange of the coordinates (spatial or spin) of each pair of electrons:

$$\Psi(\mathbf{q}_1, \dots, \mathbf{q}_i, \dots, \mathbf{q}_j, \dots, \mathbf{q}_N) = -\Psi(\mathbf{q}_1, \dots, \mathbf{q}_j, \dots, \mathbf{q}_i, \dots, \mathbf{q}_N) \quad (4.1)$$

The antisymmetry implies the so called *Pauli exclusion principle*, which states that two electrons in the same molecule cannot have identical quantum numbers.

When molecular systems are considered, one usually invokes the *orbital approximation* [45, 46] which assumes that each electron can be described by an own mono-electronic wavefunction referred to as *spinorbital*. The  $a$ -th spinorbital containing the  $i$ -th electron takes the form

$$\varphi_a(\mathbf{q}_i) = \phi_a(\mathbf{r}_i)\sigma(s_i) \quad (4.2)$$

where  $\phi_a(\mathbf{r})$  is the spatial part and is normally called *molecular orbital* (MO), while  $\sigma(s)$  is the spin part given by one of the two possible spin states for the electron, namely  $\alpha(1/2)$  or  $\beta(-1/2)$ . The MO is generally expressed as a *linear combination of atomic orbitals* (LCAO) of the form

$$\phi_a(\mathbf{r}) = \sum_v c_v^a \xi_v(\mathbf{r}) \quad (4.3)$$

where  $\xi_v(\mathbf{r})$  are *atomic orbitals* (AOs) centered on the atoms composing the molecule.

The fundamental prototype of wavefunction is expressed in the form of a *Slater determinant* [47] built on the spinorbitals set:

$$\Psi(\mathbf{q}) = \frac{1}{\sqrt{N!}} \begin{vmatrix} \varphi_a(\mathbf{q}_1) & \varphi_a(\mathbf{q}_2) & \cdots & \varphi_a(\mathbf{q}_N) \\ \varphi_b(\mathbf{q}_1) & \varphi_b(\mathbf{q}_2) & \cdots & \varphi_b(\mathbf{q}_N) \\ \vdots & \vdots & \ddots & \vdots \\ \varphi_z(\mathbf{q}_1) & \varphi_z(\mathbf{q}_2) & \cdots & \varphi_z(\mathbf{q}_N) \end{vmatrix} \quad (4.4)$$

In its explicit form, the Slater determinant is a sum of  $N!$  products of the form  $\varphi_a(\mathbf{q}_1)\varphi_b(\mathbf{q}_2) \dots \varphi_z(\mathbf{q}_N)$  describing all possible permutations of the  $N$  electrons in the  $N$  spinorbitals. Such an expression makes electrons indistinguishable and respect the antisymmetry principle, because the interchange of indices of an electron pair corresponds to the exchange of the corresponding columns in the determinant, which leads to the change of its sign. Moreover, also the Pauli exclusion principle is respected: the situation in which two electrons occupy the same spinorbital (that is, they have the same quantum numbers) corresponds to a determinant having two equal columns, resulting thus equal to zero. In the following, spin coordinates will be neglected and spinorbitals will be simply referred to as MOs.

### The Time-Independent Schrödinger Equation.

Another fundamental assumption of QM is that the wavefunction must satisfy the iconic *time-dependent Schrödinger equation*[48]:

$$\hat{H}\Psi(\mathbf{r}, t) = -\frac{\hbar}{i} \frac{\partial \Psi(\mathbf{r}, t)}{\partial t} \quad (4.5)$$

where  $\hat{H}$  is the electronic hamiltonian operator defined within the *Born-Oppenheimer* approximation (that is, by assuming the separability of electronic and nuclear motions) as (atomic units)

$$\hat{H} = -\sum_{i=1}^N \frac{1}{2} \hat{\nabla}_i^2 + \frac{1}{2} \sum_{i,j=1}^N \frac{1}{|\mathbf{r}_i - \mathbf{r}_j|} - \sum_{i=1}^N \sum_{J=1}^M \frac{Z_J}{|\mathbf{r}_i - \mathbf{R}_J|} \quad (4.6)$$

Here, the first term containing the *Laplace operator* for the electronic coordinates

$$\hat{\nabla}_i^2 = \frac{\partial^2}{\partial x_i^2} + \frac{\partial^2}{\partial y_i^2} + \frac{\partial^2}{\partial z_i^2} \quad (4.7)$$

describes the electron kinetic energy, while the second and third terms account for the electrons-electrons and electrons-nuclei coulomb interactions, respectively (in the latter, the  $J$  index runs over the  $M$  nuclei located at  $R_J$ ). Since the wavefunction is usually assumed to be factorable with respect to the spatial and temporal coordinates, that is,  $\Psi(\mathbf{r}, t) = \Psi_S(\mathbf{r})\Psi_T(t)$ , eq.(4.5) can be separated into two equations for each coordinate: the equation related to the spatial wavefunction is referred to as the *time-independent Schödinger equation* and takes the eigenvalue form

$$\hat{H}\Psi_S(\mathbf{r}) = E\Psi_S(\mathbf{r}) \quad (4.8)$$

Eq.(4.8) represents the milestone of *Quantum Chemistry*: the hamiltonian operator (4.6) is totally defined by the positions of nuclei, that is, by the chemical structure of the molecule, and the electronic states (wavefunctions) and their energies are uniquely determined as the hamiltonian's eigenstates and eigenvalues, respectively. Hereafter,  $\Psi_S$  will be referred to simply as  $\Psi$ .

### The Variational Theorem.

The variational theorem [49] is a fundamental statement of QM that provides a powerful strategy for obtaining the exact solutions of the Schrödinger equation starting from trial solutions. Considering the exact wavefunction, the energy of the systems can be written from the eigenvalue equation (4.8) as

$$E_{exact} = \frac{\langle \Psi | \hat{H} | \Psi \rangle}{\langle \Psi | \Psi \rangle} \quad (4.9)$$

where the bracket notation indicates the integral over the electrons coordinates. Considering instead the trial wavefunction  $|\Psi_{\text{trial}}\rangle$ , the associated energy is analogously calculated as

$$E_{\text{trial}} = \frac{\langle \Psi_{\text{trial}} | \hat{H} | \Psi_{\text{trial}} \rangle}{\langle \Psi_{\text{trial}} | \Psi_{\text{trial}} \rangle} \quad (4.10)$$

Since the hamiltonian eigenstates set represents a complete basis set,  $|\Psi_{\text{trial}}\rangle$  can be always written as a linear combination of the exact states. By exploiting this mathematical property, one can easily show that the following disequality always holds:

$$E_{\text{trial}} \geq E_{exact} \quad (4.11)$$

This equation straightforwardly suggests the strategy for obtaining the best approximate solution: since each approximate solution is always higher in energy than the exact one, every wavefunction parametrization will provide the best approximation simply by finding those parameters that minimize the energy given by eq.(4.10).

**The Hartree-Fock Theory.**

The Hartree-Fock (HF) method [50, 51, 52] is a MO optimization-procedure for minimizing the energy of a wavefunction expressed in the form of a Slater determinant. By using the Slater-Condon rules for mono- and bi-electronic integrals [47, 53, 54], the energy of the Slater determinant can be written as

$$E_{trial} = \sum_a h_a + \frac{1}{2} \sum_{a,b} J_{ab} - K_{ab} \quad (4.12)$$

where the *core hamiltonian*

$$h_a = \langle \phi_a | \hat{h}_1 | \phi_a \rangle \quad (4.13)$$

$$\hat{h}_1 = -\frac{1}{2} \hat{\nabla}_1^2 - \frac{Z_J}{|\mathbf{r}_1 - \mathbf{R}_J|} \quad (4.14)$$

contains the kinetic energy of the electron occupying the  $a$ -th MO and its coulomb interaction with nuclei, the *Coulomb integral*

$$J_{ab} = \langle \phi_a \phi_b | 1/r_{12} | \phi_a \phi_b \rangle = \int \int \phi_a^*(\mathbf{r}_1) \phi_b^*(\mathbf{r}_2) \frac{1}{r_{12}} \phi_a(\mathbf{r}_1) \phi_b(\mathbf{r}_2) d\mathbf{r}_1 d\mathbf{r}_2 \quad (4.15)$$

(in which  $r_{12} = |\mathbf{r}_1 - \mathbf{r}_2|$ ) accounts for the spatially-averaged coulomb interaction between the two electrons occupying the  $\phi_a$  and  $\phi_b$  MOs, and the *exchange integral*

$$K_{ab} = \langle \phi_a \phi_b | 1/r_{12} | \phi_b \phi_a \rangle = \int \int \phi_a^*(\mathbf{r}_1) \phi_b^*(\mathbf{r}_2) \frac{1}{r_{12}} \phi_b(\mathbf{r}_1) \phi_a(\mathbf{r}_2) d\mathbf{r}_1 d\mathbf{r}_2 \quad (4.16)$$

is a pure quantum mechanical quantity that has no counterparts in the classical electrostatics.

Basing on the variational theorem, one can set the conditions for optimizing the MOs in order to minimize the energy given by (4.12): by exploiting the Lagrange method of undetermined multipliers [55] (which ensures MOs to remain orthonormal), the minimization conditions lead to the *HF equations*

$$\hat{f}(\mathbf{r}_1) \phi_a(\mathbf{r}_1) = \epsilon_a \phi_a(\mathbf{r}_1) \quad (4.17)$$

where  $\epsilon_a$  is the MO energy and  $\hat{f}(\mathbf{r}_1)$  is the *Fock operator*

$$\hat{f}(\mathbf{r}_1) = \hat{h}(\mathbf{r}_1) + \sum_b \hat{J}_b(\mathbf{r}_1) - \hat{K}_b(\mathbf{r}_1) \quad (4.18)$$

in which the Coulomb and exchange operator act on the MOs in the following way:

$$\hat{J}_b(\mathbf{r}_1) \phi_a(\mathbf{r}_1) = \left[ \int \phi_b^*(\mathbf{r}_2) \frac{1}{r_{12}} \phi_b(\mathbf{r}_2) d\mathbf{r}_2 \right] \phi_a(\mathbf{r}_1) \quad (4.19)$$

$$\hat{K}_b(\mathbf{r}_1) \phi_a(\mathbf{r}_1) = \left[ \int \phi_b^*(\mathbf{r}_2) \frac{1}{r_{12}} \phi_a(\mathbf{r}_2) d\mathbf{r}_2 \right] \phi_b(\mathbf{r}_1) \quad (4.20)$$

Since the Fock operators depend on the MOs that are their eigensolutions, HF equations take the form  $\hat{f}(\{\phi_b\})\phi_a = \varepsilon_a\phi_a$ . Such equations are solved iteratively: an initial set of trial MOs is used to build trial Fock operators and the eigenvalue problem of eq.(4.17) is solved leading to a new set of optimized MOs. This new set is used to build up another Fock operator and the cycle is repeated until the MOs of the last cycle remain almost unchanged with respect to the penultimate, namely, until the *self-consistency* of the cycle is reached.

Another striking result of the HF theory concerns the physical meaning of MOs energies: the *Koopmans theorem* [56] elegantly demonstrates that the energies of the *highest occupied molecular orbital* (HOMO) and the *lowest unoccupied molecular orbital* (LUMO) correspond to the *ionization potential* (IP) and *electron affinity* (EA) of the molecule, respectively:

$$\varepsilon_{HOMO} = -IP \quad (4.21)$$

$$\varepsilon_{LUMO} = -EA \quad (4.22)$$

### 4.1.2 Density Functional Theory

One of the major drawback of wavefunction-based methods is that the computational cost increase upon extending the molecular size to such an extent that molecules composed by more than about 100 atoms are completely out of reach. The most powerful method allowing for circumventing this problem is the *Density Functional Theory* (DFT) [57, 58], which is aimed at calculating the molecular energy by using an electron density determined without any calculation of the wavefunction.

#### The Electron Density.

The electron density is uniquely determined by the wavefunction through the following expression:

$$\rho(\mathbf{r}_1) = N \int \cdots \int \Psi^*(\mathbf{r}_1, \mathbf{r}_2, \dots, \mathbf{r}_N) \Psi(\mathbf{r}_1, \mathbf{r}_2, \dots, \mathbf{r}_N) d\mathbf{r}_2 \dots d\mathbf{r}_N \quad (4.23)$$

where the integration is performed over the coordinate of all electrons excepted one (by virtue of the indistinguishability principle, this electron represents a generic electron). If the wavefunction takes the form of a Slater determinant, eq.(4.4), the electron density is readily obtained from MOs as

$$\rho(\mathbf{r}_1) = \sum_a^N |\phi_a(\mathbf{r}_1)|^2 \quad (4.24)$$

Being the electron density a very simpler mathematical object with respect to the wavefunction (the former is a mono-electronic function and thus depends on 3 coordinates only, while the latter depends on the whole set of 3N coordinates), the computational cost of DFT methods is extremely reduced with respect to wavefunction-based ones, and this fact represented the turning point that opened the way of QM calculations to large molecular systems (hundreds of atoms).

### The Hohenberg-Kohn Theorem.

The possibility of exploiting the electron density as the sole ingredient to determine the molecular energy lies on the famous *Hohenberg-Kohn theorem* [59], which states that the electron density uniquely determines both the number of electrons composing the system and the electric field generated by the nuclei, which in turn uniquely determine the nuclear arrangement composing the molecular structure. Together, these two statements imply that the electron density uniquely determines also the whole electronic energy for the *ground state* (GS) of the system, which can be therefore written as a *functional* of the electron density:

$$E = E[\rho] \tag{4.25}$$

Since the electron density is uniquely related to the wavefunction, it can be shown that the variational principle holds also for the density functional:

$$E[\rho_{\text{trial}}] \geq E_{\text{exact}} \tag{4.26}$$

The deep piece of information given by the Hohenberg-Kohn theorem is that the electron density suffices for having a complete description of the system; nevertheless, it is not possible to *a priori* know the exact mathematical expression underlying eq.(4.25). During last decades, researchers have proposed a huge variety of reliable density functionals which have nowadays become one of the most widely used tools in the field of Quantum Chemistry.

### Density Functionals for Molecular Energy.

The exact density functional takes the general form

$$E_{\text{exact}}[\rho] = T[\rho] + E_{ee}[\rho] + E_{eN}[\rho] \tag{4.27}$$

where the three terms represent the electronic kinetic energy, the interelectronic interactions and the electrons-nuclei interactions, respectively. While the term accounting for the electrons-nuclei interactions takes the straightforward form

$$E_{eN}[\rho] = - \sum_{J=1}^M \int \frac{Z_J \rho(\mathbf{r}_1)}{|\mathbf{r}_1 - \mathbf{R}_J|} d\mathbf{r}_1, \tag{4.28}$$

a successful formula for the kinetic energy has never been found. This fact determined a relevant breakthrough in the history of the DFT development, opening the way to the cunning idea by Kohn and Sham [60] who solved the problem of the kinetic energy by re-introducing MOs, which in turn allowed for the definition of a successful expression also for the interelectronic interaction term.

#### 4.1.3 Kohn-Sham Theory

The Kohn-Sham method for DFT (KS-DFT) [60] is based on the use of a set of auxiliary MOs  $\{\phi_a\}$  defining a Slater determinant which has no physical meaning (that is, it is not the real wavefunction) but is simply required to reproduce the density via eq.(4.24). Such

MOs are used for calculating the kinetic energy term, which is thus no longer considered as a functional of the density:

$$T_{KS}[\{\phi_a\}] = -\frac{1}{2} \sum_a^N \langle \phi_a | \hat{\nabla}_1^2 | \phi_a \rangle \quad (4.29)$$

Such a definition allows to rewrite the functional for the molecular energy as

$$E[\rho] = T_{KS}[\rho] + J[\rho] + E_{XC}[\rho] + E_{eN}[\rho] \quad (4.30)$$

where the second term is the inter-electronic coulomb interaction functional

$$J[\rho] = \int \int \frac{\rho(\mathbf{r}_1)\rho(\mathbf{r}_2)}{|\mathbf{r}_1 - \mathbf{r}_2|} d\mathbf{r}_1 d\mathbf{r}_2 \quad (4.31)$$

and the third term is the *exchange-correlation* (XC) energy functional, accounting for all the quantum effects, that is, the exchange interactions and the correlation effects. This crucial term is simply defined as

$$E_{XC}[\rho] = T[\rho] - T_{KS}[\rho] + E_{ee}[\rho] - J[\rho] \quad (4.32)$$

and is assumed to take the simple form

$$E_{XC}[\rho] = E_X[\rho] + E_C[\rho] = \int \epsilon_X[\rho(\mathbf{r}_1)]\rho(\mathbf{r}_1)d\mathbf{r}_1 + \int \epsilon_C[\rho(\mathbf{r}_1)]\rho(\mathbf{r}_1)d\mathbf{r}_1 \quad (4.33)$$

where two separated exchange ( $\epsilon_X$ ) and correlation ( $\epsilon_C$ ) functionals have been introduced.

Similarly to the HF MOs, also KS MOs are determined basing on the variational theorem, that is, they are obtained through an optimization procedure aimed at minimizing the DFT energy. Also in this case, the minimization condition leads to the fulfilling of a set of eigenvalue equations for the MOs, the so-called *Kohn-Sham equations*:

$$\hat{h}_{KS}(\mathbf{r}_1)\phi_a(\mathbf{r}_1) = \varepsilon_a^{KS} \phi_a(\mathbf{r}_1) \quad (4.34)$$

where the *Kohn-Sham operator* reads

$$\hat{h}_{KS}(\mathbf{r}_1) = -\frac{1}{2}\hat{\nabla}_1^2 + V_N(\mathbf{r}_1) + V_H[\rho(\mathbf{r}_1)] + V_{XC}[\rho(\mathbf{r}_1)] \quad (4.35)$$

in which  $V_N$  is the nuclear potential and  $V_H$  and  $V_{XC}$  are the *Hartree potential* and *XC potential* functionals, respectively:

$$V_H[\rho(\mathbf{r}_1)] = \int d\mathbf{r}_2 \frac{\rho(\mathbf{r}_2)}{|\mathbf{r}_1 - \mathbf{r}_2|}, \quad (4.36)$$

$$V_{XC}[\rho(\mathbf{r}_1)] = \frac{\delta E_{XC}[\rho(\mathbf{r}_1)]}{\delta \rho(\mathbf{r}_1)} \quad (4.37)$$

Since the KS operators are functionals of the density which in turn depends on the spinorbitals that are their eigensolutions, KS equations take the form  $\hat{h}_{KS}(\{\phi_b\})\phi_a = \varepsilon_a \phi_a$  and are thus solved iteratively.

The KS MOs are deeply different from HF ones: while HF MOs are calculated by considering spatially-averaged inter-electronic interactions between pairs, KS MOs are obtained by considering (i) a simple Coulomb interaction between macroscopic densities and (ii) extremely rough quantum effects described by simple local functionals: this means that in DFT electrons have to be considered as spurious particles, that is, mere mathematical devices conceived to obtain the correct GS density only. Moreover, in HF theory the Koopmans theorem ensures the MOs'energies to have a demonstrated physical meaning, while a corresponding theorem does not exist in KS theory.

During last decades, a huge number of XC local functionals have been proposed, and a brief summary of the most widely used can be found in the following subsection. The most serious issue concerning XC functionals is that they suffers from a deficiency intrinsically related to the concept of functional, that is, the *locality* problem: differently from the  $J$  functional, which includes the interaction between densities at different points,  $E_{XC}$  is a functional of a single density and is therefore local in space, that is, it only depends on the density at a given point completely neglecting contributions from the quantum interactions between densities at different points. Due to this rude approximation, local functionals commonly fail in reproducing certain molecular properties. The most successful attempt to solve the locality problem has been provided by the introduction of *hybrid functionals*, which are discussed in section 4.1.5.

### Local Exchange-Correlation Functionals.

The two main categories of *local XC functionals* are the *Local Spin Density Approximation* (LSDA), which assume the energy to be a pure local functional of the density, and the *Generalized Gradient Approximation* (GGA), which introduce in the functional a dependence on the gradient of the density and are therefore referred to as *semi-local* functionals.

The LSDA assumes that the electrons within a molecule can be described by the same functional of the most simple many-electrons system, that is, the uniform gas of electrons, for which the exchange functional has been demonstrated to take the simple analytical form [61, 62]

$$\epsilon_X^{LDA}[\rho(\mathbf{r}_1)] = -\frac{3}{4} \left( \frac{6}{\pi} \right)^{1/3} \int \left( \rho_\alpha^{4/3}(\mathbf{r}_1) + \rho_\beta^{4/3}(\mathbf{r}_1) \right) d\mathbf{r}_1 \quad (4.38)$$

where different electron densities have been introduced for the two kind of spins. Differently from the exchange, for the correlation no analytical expressions can be derived, but since the exact correlation energy for the electron gas can be directly calculated by QM methods, several analytical expressions for interpolating its dependence on the density have been proposed: the most widely used formulas are those developed by *Perdew and Wang* (PW) [63] and by *Vosko, Wilk and Nusair* (VWN) [64].

The GGA functionals take advantage of the density gradient as a variable to set up flexible interpolation formulas allowing for the fitting of XC effects calculated through QM methods for single atoms. Among the most widely used GGA XC functionals there are the *Becke's exchange* (B88) [65], which corrects the LDA expression eq.(4.38) with a simple additive term aimed to fit the QM exchange in rare gas atoms, and the correlation functional by *Lee, Yang and Parr* (LYP) [66], which offers a quite complicated expression for fitting the correlation of the helium atom. Another widely used XC functional is the one developed by

*Perdew, Burke and Ernzerhof* (PBE) [67], which introduces a multiplicative correction to the LDA exchange and an additive correction to the LDA correlation, and whose parameters are not derived in an empirical fashion (that is, by fittings some data) but are instead established from theoretical considerations.

#### 4.1.4 The Correction for Dispersion Interactions.

Probably, the most serious deficiency of DFT is that functionals are normally unable to account for dispersion interactions among atoms: while certain functionals even predict purely repulsive interactions, others are able to account only for a slight stabilizing interaction, but basically all standard functionals fail in reproducing the typical  $1/R^6$  long-range behaviour characterizing the dispersion interaction between two atoms.

The most simple strategy for fixing this deficiency is to include into the functional (4.30) empirical terms describing the dispersion interactions for each couple of atoms. A very refined and successful model is the so called *D3 corrections* presented by S. Grimme and collaborators [68], who introduced also higher order terms with  $1/R^8$  form aimed to better account the medium-range dispersions: the correction to the total energy is given by

$$E_{disp}^{D3} = -\frac{1}{2} \sum_{A,B} \left[ s_6 \frac{C_{6,AB}}{R_{AB}^6} f_{6,damp}(R_{AB}) + s_8 \frac{C_{8,AB}}{R_{AB}^8} f_{8,damp}(R_{AB}) \right] \quad (4.39)$$

where the  $A, B$  indexes run over atoms, the  $C_{n,AB}$  (with  $n = 6, 8$ ) are atom-dependent coefficients of the form  $C_{n,AB} = \sqrt{C_{n,A}C_{n,B}}$  ( $C_{n,A}$  and  $C_{n,B}$  are tabulated coefficient which have been determined for each element),  $s_n$  is a functional-dependent scaling factor aimed for accounting the possible attractive interactions predicted by the functionals in their uncorrected form and  $f_{n,damp}$  are damping functions of the form

$$f_{n,damp}(R_{AB}) = \left[ 1 + 6 \left( \frac{R_{AB}}{s_{n,r} R_{AB}^0} \right)^{-\beta_n} \right]^{-1} \quad (4.40)$$

where  $R_{AB}^0$  are parameters obtained from the van der Waal radii of  $A$  and  $B$  atoms,  $\beta_6 = 12$ ,  $\beta_8 = 14$ ,  $s_{6,r} = 1$  and  $s_{8,r}$  has to be optimized for each functional.

#### 4.1.5 Generalized Kohn-Sham Theory

In the *Generalized Kohn-Sham* (GKS) theory [69, 70], the density functional of eq.(4.30) is redefined by considering for both the kinetic energy and the inter-electronic interactions the possibility of having a generic parametrization based on a set of auxiliary MOs  $\{\phi_a\}$ , that is, the density functional is assumed to be described by the general expression:

$$E[\rho, \{\phi_a\}] = E_{eN}[\rho] + S[\{\phi_a\}] + R[\rho] \quad (4.41)$$

where  $S[\{\phi_a\}]$  is the term containing the MOs dependence and  $R[\rho]$  is a remainder term that, considering  $E[\rho]$  to be the energy given by eq.(4.30), is simply defined as  $R[\rho] = E[\rho] - S[\{\phi_a\}]$ , that is, is a term aimed to ensure eq.(4.41) to give exactly the same energy

of eq.(4.30). When MOs are optimized to minimize the energy associated to this functional form, the following *GKS equations* are obtained:

$$\hat{h}_{GKS}(\mathbf{r}_1)\phi_a(\mathbf{r}_1) = \varepsilon_a\phi_a(\mathbf{r}_1) \quad (4.42)$$

where the GKS operator reads

$$\hat{h}_{GKS}(\mathbf{r}_1) = O_S[\{\phi_a\}] + V_{eN}[\rho(\mathbf{r}_1)] + V_R[\rho(\mathbf{r}_1)] \quad (4.43)$$

in which  $O_S$  is the sole MOs-dependent term and the potential associated to  $R$  takes the same form of eq.(4.37)

$$V_R[\rho(\mathbf{r}_1)] = \frac{\delta R[\rho(\mathbf{r}_1)]}{\delta \rho(\mathbf{r}_1)} \quad (4.44)$$

The most important result from GKS theory is that the optimal MOs are always determined by an eigenvalue equation with the same form of the original KS equations, eq.(4.34), independently from the chosen MOs-based parametrization of eq.(4.41).

### Hybrid Functionals.

The GKS method can be used to finally fix the problem of the locality of the XC functional, and this is made possible by introducing the *non-local* quantum exchange energy calculated on the auxiliary spinorbitals, which is usually referred to as *exact or HF exchange*:

$$E_X^{HF} = \sum_{a,b}^N K_{ab} \quad (4.45)$$

where the exchange integrals  $K_{ab}$  are given by eq.(4.16). In *hybrid functionals*, the XC functional is given by

$$E_{XC}^{Hyb}(\alpha) = \alpha E_X^{HF} + (1 - \alpha)E_X^{DFT} + E_C^{DFT} \quad (4.46)$$

where  $0 < \alpha < 1$  is a parameter governing the extent of HF exchange to be included and  $E_X^{DFT}$  and  $E_C^{DFT}$  are the terms of eq.(4.33) (the "DFT" label reminds that these are density functionals). In the framework of GKS theory, this is equivalent to set

$$S[\{\phi_a\}] = T_{KS}[\{\phi_a\}] + \alpha E_X^{HF}[\{\phi_a\}] \quad (4.47)$$

$$R[\rho] = E_{eN}[\rho] + J[\rho] + E_C^{DFT}[\rho] + (1 - \alpha)E_X^{DFT}[\rho] \quad (4.48)$$

The operator defining the corresponding GKS equations is found to be

$$\begin{aligned} \hat{h}_{Hyb}(\mathbf{r}_1) = & -\frac{1}{2}\hat{\nabla}_1^2 + V_N(\mathbf{r}_1) + V_H[\rho(\mathbf{r}_1)] + \alpha V_X^{HF}(\mathbf{r}_1) \\ & + (1 - \alpha)V_X^{DFT}[\rho(\mathbf{r}_1)] + V_C^{DFT}[\rho(\mathbf{r}_1)] \end{aligned} \quad (4.49)$$

where the  $V_X^{HF}$  operator acts on the spinorbitals in the same way as the HF exchange operator, eq.(4.20), and the  $V_X^{DFT}$  and  $V_C^{DFT}$  potentials have the same form of eq.s (4.37) and (4.44).

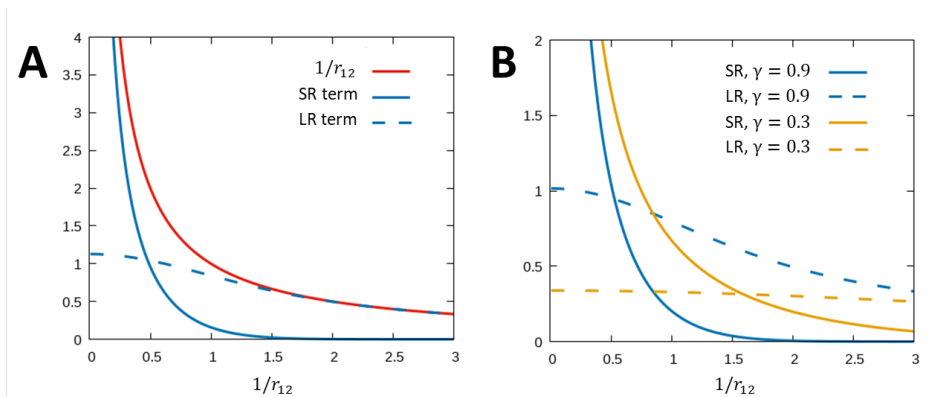


**Figure 4.1:** (A) The splitting of the Coulomb operator employed in RSH functionals. The short-range (SR) and long-range (LR) terms correspond to  $1 - \text{erf}(\gamma r_{12})/r_{12}$  (full line) and  $\text{erf}(\gamma r_{12})/r_{12}$  (dashed line) respectively. The value  $\gamma = 1$  has been used. (B) Effect of the range separation parameter on the SR and LR terms. The values  $\gamma = 0.9$  (blue) and  $\gamma = 0.3$  (orange) are compared.

Among the widely used hybrid functionals there is the PBE0 functional [71], which is based on the PBE XC functional (see section 4.1.3) and contains the 25% of HF exchange, a value obtained from theoretical considerations:

$$E_{XC}^{PBE0} = 0.75E_X^{PBE} + 0.25E_X^{HF} + E_C^{PBE} \quad (4.50)$$

Probably, the most used hybrid is the B3LYP functional [72, 73], which contains a mixing of LSDA and B88 exchange along with a mixing of LSDA and LYP correlation and introduces three parameters to differently weight each contribute:

$$E_{XC}^{B3LYP} = (1 - a)E_X^{LSDA} + aE_X^{HF} + bE_X^{B88} + (1 - c)E_C^{LSDA} + cE_C^{LYP} \quad (4.51)$$

where the optimal parameters  $a=0.20$ ,  $b=0.72$  and  $c=0.81$  have been determined by fitting experimental data.

### Range-Separated Hybrid Functionals.

A deeper control on the HF exchange extent included in the functional has been made possible by the advent of *range-separated hybrid* (RSH) or *long-range corrected* (LC) functionals [74], in which the amount of HF exchange can be modulated upon varying the inter-electronic distance. To introduce this further flexibility, the Coulomb operator entering the exchange integrals is split by means of the error functions (*erf*) in the following way:

$$\frac{1}{r_{12}} = \frac{1 - \text{erf}(\gamma r_{12})}{r_{12}} + \frac{\text{erf}(\gamma r_{12})}{r_{12}} \quad (4.52)$$

Here, the first and second terms represent the short-range (SR) and long-range (LR) contributions, respectively, and the range-separation parameter  $\gamma$  is used to establish the switching

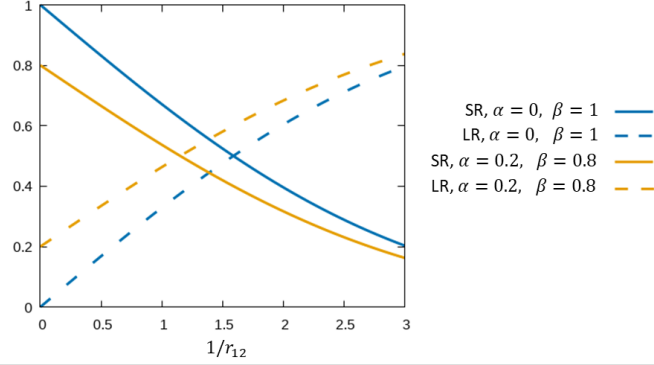


**Figure 4.2:** Comparison between SR and LR terms employed in standard (blue) and CAM (orange) RSH functionals. The reported SR terms correspond to  $1 - \text{erf}(\gamma r_{12})$  and  $1 - \alpha - \beta \text{erf}(\gamma r_{12})$  (full lines), while the LR terms correspond to  $\text{erf}(\gamma r_{12})$  and  $\alpha + \beta \text{erf}(\gamma r_{12})$  (dashed lines). The value  $\gamma = 0.3$ ,  $\alpha = 0.2$  and  $\beta = 0.8$  have been used. While for the standard RSH functional the SR and LR terms are 100% and 0% respectively for  $r_{12} \rightarrow 0$ , for the CAM functional such values are given by  $\beta$  and  $\alpha$  respectively.

distance between the two terms, which corresponds to  $1/\gamma$ . The shape of these terms is reported in figure 4.1. A very successful strategy is to associate the SR and LR terms to the DFT and HF exchange respectively: the HF exchange is obtained by substituting the LR term of eq.(4.52) into the HF exchange integrals in eq.(4.45):

$$E_{X,HF}^{LR}[\{\phi_a\}](\gamma) = \sum_{a,b}^N \langle \phi_a \phi_b | \text{erf}(\gamma r_{12}) / r_{12} | \phi_b \phi_a \rangle \quad (4.53)$$

while the SR term is simply obtained by replacing the lacking HF exchange with the DFT counterpart, indicated as  $E_{X,DFT}^{SR}[\rho](\gamma)$ . The XC for RSH functionals is thus written as

$$E_{XC}^{RSH}(\gamma) = E_{X,HF}^{LR}(\gamma) + E_{X,DFT}^{SR}(\gamma) + E_C^{DFT} \quad (4.54)$$

The parametrization given by eq.(4.52) implies that 100% of HF and DFT exchange are used at LR and SR, respectively; a more flexible parametrization is the one employed in the *Coulomb-attenuated* (CAM) functionals [75], in which two additional parameters  $\alpha$  and  $\beta$  allow for a modulation of the HF exchange at both SR and LR basing on the following split of the coulomb operator:

$$\frac{1}{r_{12}} = \frac{1 - \alpha - \beta \text{erf}(\gamma r_{12})}{r_{12}} + \frac{\alpha + \beta \text{erf}(\gamma r_{12})}{r_{12}} \quad (4.55)$$

The effect of  $\alpha$  and  $\beta$  parameters is depicted in figure 4.2. The corresponding XC functional reads

$$E_{XC}^{RSH}(\gamma, \alpha, \beta) = \alpha E_{X, HF}^{SR}(\gamma) + (1 - \alpha) E_{X, DFT}^{SR}(\gamma) \\ + (\alpha + \beta) E_{X, HF}^{LR}(\gamma) + (1 - \alpha - \beta) E_{X, DFT}^{LR}(\gamma) + E_C^{DFT} \quad (4.56)$$

and the operators defining the GKS equations are found to be

$$\hat{h}_{RSH}(\mathbf{r}_1) = -\frac{1}{2} \hat{\nabla}_1^2 + V_N(\mathbf{r}_1) + V_H[\rho(\mathbf{r}_1)] + \alpha V_{X, HF}^{SR}(\mathbf{r}_1) + (1 - \alpha) V_{X, DFT}^{SR}[\rho(\mathbf{r}_1)] \\ + (\alpha + \beta) V_{X, HF}^{LR}(\mathbf{r}_1) + (1 - \alpha - \beta) V_{X, DFT}^{LR}[\rho(\mathbf{r}_1)] + V_C^{DFT}[\rho(\mathbf{r}_1)] \quad (4.57)$$

where the  $V_{X, HF}^{SR}$  and  $V_{X, HF}^{LR}$  operators act on the MOs in the same way as the HF exchange operator, eq.(4.20), but with the  $1/r_{12}$  term substituted by the first and second terms of eq.(4.52), and the  $V_{X, DFT}^{SR}$ ,  $V_{X, DFT}^{LR}$  and  $V_C^{DFT}$  potentials have the same form of eq.s (4.37) and (4.44).

Among the most widely used RSH functionals there are the CAM-B3LYP functional [75] using the B3LYP XC with parameters  $\gamma=0.33$ ,  $\alpha=0.19$ ,  $\beta=0.46$  and the LC-PBE functional [76] using the PBE XC with parameters  $\gamma=0.47$ ,  $\alpha=0$ ,  $\beta=1$ .

#### 4.1.6 Solvent Effect: the Polarizable Continuum Model

Since QM calculations often refer to molecules in solution, it becomes necessary to take into account also the interaction with the surrounding solvent molecules. A very computationally efficient method for describing solvent effects is represented by the *Continuum Polarization Model* (PCM) [77, 78], in which the solvent is assumed to be described by a continuous dielectric medium (that is, the atomistic structure of solvent molecules is completely neglected) and the solute molecule is considered to be encapsulated into a certain cavity within that medium. To simplify the description of the dielectric polarization induced by the molecular charge distribution  $\rho_M$ , it is also assumed that the response of the whole dielectric can be reduced to the response of the cavity surface only. The electrostatic description of such a system consists in determining the surface charge distribution of the cavity, indicated as  $\sigma(\mathbf{s})$  (where  $\mathbf{s}$  is a vector indicating a generic point on the surface  $S$ ), generated by the polarization induced by  $\rho_M$ . Basing on the Poisson equation, which provides the electrostatic potential associated to a certain distribution of charges, the following integral equation is obtained [79, 80]:

$$\left(2\pi \frac{\epsilon + 1}{\epsilon - 1} - \hat{D}\right) \hat{S}\sigma(\mathbf{s}) = -(2\pi - \hat{D})V_M(\mathbf{s}) \quad (4.58)$$

where  $V_M$  is the electrostatic potential generated by  $\rho_M$  on the surface and the integral operators act on a generic function  $f(\mathbf{s})$  in the following way

$$\hat{S}f(\mathbf{s}) = \int_S \frac{1}{|\mathbf{s} - \mathbf{s}'|} f(\mathbf{s}') ds' \quad (4.59)$$

$$\hat{D}f(\mathbf{s}) = \int_S \left[ \frac{\partial}{\partial \mathbf{n}_s} \frac{1}{|\mathbf{s} - \mathbf{s}'|} \right] f(\mathbf{s}') ds' \quad (4.60)$$

where  $\mathbf{n}_s$  represents the unit vector applied at the surface point  $\mathbf{s}$  and pointing toward the dielectric.

To reduce the computational effort required for solving this equation, the charge distribution on the cavity surface is discretized into a set of surface elements, each one located by a vector  $s_n$  and bearing a charge  $q_n$ : within this approximation, eq.(4.58) can be recast in a matrix equation of the form

$$\mathbf{T}\mathbf{q} = -\mathbf{R}\mathbf{V}_N \quad (4.61)$$

where  $\mathbf{q}$  and  $\mathbf{V}_M$  are vectors containing, respectively, the surface charges and the electrostatic potential generated by the solute on each surface element, while  $\mathbf{T}$  and  $\mathbf{R}$  are the matrix analogue of operators defined in eq.(4.58) containing the discrete representation of  $\hat{S}$  and  $\hat{D}$  operators.

Once the surface charges associated to a certain  $\rho_M$  are obtained, they are used to build the PCM solute-solvent electrostatic interaction operator

$$\hat{V}_{PCM} = \sum_n q_n V_M(\mathbf{s}_n) \quad (4.62)$$

which has to be added to the electronic hamiltonian for molecules in vacuum, eq.(4.6). Since the  $V_M$  potential is to be calculated from the hamiltonian eigensolution, the Schrödinger equation for the molecule solvated by using the PCM takes the form  $[\hat{H} + \hat{V}_{PCM}(\Psi)]\Psi = E\Psi$ , and has thus to be solved iteratively (starting from a guess set of surface charges) until the self-consistency is reached.

Since both HF and KS-DFT theory are self-consistent methods, the application of PCM solvation is straightforward [81]. The resulting Fock and KS operators keep the same forms given by eq.s (4.18) and (4.35) but with an additional term describing the interaction between the electron in a given MO and the surface elements charges:

$$\hat{v}_{PCM}(\mathbf{r}_1) = - \sum_n \frac{q_n}{|\mathbf{r}_1 - \mathbf{s}_n|} \quad (4.63)$$

### 4.1.7 Excited State Calculations: Time-Dependent Density Functional Theory

#### Response Theory for Wavefunctions.

When a molecule experiences an electromagnetic radiation, the electrons-field interaction can be responsible for the excitation of the electronic state, which is promoted from its GS to a certain excited state (ES) upon absorbing the energy provided by the incident photon. Several advanced wavefunction methods are nowadays available for determining the molecular ES properties, and all of them are based on the complete calculation of the ES wavefunction; nevertheless, extended molecular systems are often out of reach because of the very high computational costs. An alternative less-demanding method is provided by the QM *Response Theory* [82, 83, 84], which allows to determine ES properties basing on the GS response to the incident electromagnetic field, a property that can be obtained without any explicit calculation of the ES wavefunction.

The generic hamiltonian describing a molecule interacting with an oscillating electric field  $\mathbf{E}(t) = \mathbf{E}_0 \cos(\omega t)$  is given by

$$\hat{H}(t) = \hat{H}_0 - \hat{\boldsymbol{\mu}} \cdot \mathbf{E}(t) \quad (4.64)$$

where  $\hat{H}_0$  is the unperturbed hamiltonian given by eq.(4.6) and  $\hat{\boldsymbol{\mu}}$  is the molecular dipole moment. If the field is weak enough, the interaction term  $\hat{\boldsymbol{\mu}} \cdot \mathbf{E}$  can be treated as a small perturbation of  $\hat{H}_0$ , and  $\hat{\boldsymbol{\mu}}$  can be referred to as a *perturbation operator*. The perturbed wavefunction is indicated as  $|\Psi(t)\rangle$ , while the unperturbed GS wavefunction is indicated as  $|\Psi_0\rangle$ . In Response Theory, the mean value of a generic operator  $\hat{O}$  is expressed as a Taylor expansion with respect to the perturbation operator:

$$\langle \Psi(t) | \hat{O} | \Psi(t) \rangle = \langle \Psi_0 | \hat{O} | \Psi_0 \rangle + \langle \langle \hat{O}; \mu \rangle \rangle \mu e^{-i\omega t} + \frac{1}{2} \langle \langle \hat{O}; \mu, \mu \rangle \rangle \mu^2 e^{-i2\omega t} + \dots \quad (4.65)$$

where  $\langle \langle \hat{O}; \mu \rangle \rangle$  is defined as the *linear response function*,  $\langle \langle \hat{O}; \mu, \mu \rangle \rangle$  as the *quadratic response function* and so on. The most striking property of the response functions defined in eq.(4.65) is that they allows for the calculation of a wide range of ES properties (whatever the chosen operator  $\hat{O}$ ) such as transition energies and transition dipole moments for the linear one-photon absorption (from linear response) but also for the two-photon absorption and excited-state absorption (from quadratic response). Indeed, by assuming to known the set of  $\hat{H}_0$  eigenstates,  $\{|\Psi_k\rangle\}$ , and using it as basis set for expressing  $|\Psi\rangle$ , one can derive explicit expressions for the response functions; for example, the linear response is found to be given by

$$\langle \langle \hat{O}; \mu \rangle \rangle = \sum_k \frac{\langle \Psi_0 | \hat{O} | \Psi_k \rangle \langle \Psi_k | \mu | \Psi_0 \rangle}{\omega - (E_k - E_0)} - \frac{\langle \Psi_0 | \mu | \Psi_k \rangle \langle \Psi_k | \hat{O} | \Psi_0 \rangle}{\omega + E_k - E_0} \quad (4.66)$$

from which one can immediately see that the transition frequency for the transition to the k-th state  $\omega_{0k} = E_k - E_0$  corresponds to the *singularity* of the linear response, that is, the frequency at which the denominator in eq.(4.66) becomes zero and thus the response function becomes infinite, while the corresponding transition dipole moments can be extracted through the so-called *residue* defined as

$$\lim_{\omega \rightarrow \omega_{0k}} \hbar(\omega - \omega_{0k}) \langle \langle \hat{O}; \mu \rangle \rangle \equiv \langle \Psi_0 | \hat{O} | \Psi_k \rangle \langle \Psi_k | \mu | \Psi_0 \rangle \quad (4.67)$$

These relations simply serve as mathematical conditions for the extraction of ES properties from response functions, which are actually determined without any calculation of the ES wavefunctions  $\{|\Psi_k\rangle\}$ .

### Time-Dependent Hartree-Fock Theory.

Considering an HF wavefunction (expressed in the form of a Slater determinant) for which are available a set of occupied  $\{\phi_a\}$  and virtual  $\{\phi_i\}$  MOs, one can demonstrate that the linear response function can be calculated as [83]

$$\langle \langle \hat{O}; \mu \rangle \rangle = -(\mathbf{O} \mathbf{O}^*) \begin{pmatrix} \mathbf{A} & \mathbf{B} \\ \mathbf{A}^* & \mathbf{B}^* \end{pmatrix}^{-1} \begin{pmatrix} \mathbf{M} \\ \mathbf{M}^* \end{pmatrix} \quad (4.68)$$

where the matrix elements are built on the occupied and virtual spinorbitals and read

$$O_a^i = \langle \phi_a | \hat{O} | \phi_i \rangle \quad (4.69)$$

$$M_a^i = \langle \phi_a | \mu | \phi_i \rangle \quad (4.70)$$

$$A_{ab}^{ij} = \delta_{ab} \delta_{ij} (\epsilon_a - \epsilon_b) + \langle \phi_a \phi_b | 1/r_{12} | \phi_i \phi_j \rangle - \langle \phi_a \phi_i | 1/r_{12} | \phi_b \phi_j \rangle \quad (4.71)$$

$$B_{ab}^{ij} = \langle \phi_a \phi_b | 1/r_{12} | \phi_i \phi_j \rangle - \langle \phi_a \phi_b | 1/r_{12} | \phi_j \phi_i \rangle \quad (4.72)$$

The excitation energies are determined exploiting the singularity condition for the response (4.68), which leads to the following eigenvalue matrix equation

$$\begin{pmatrix} \mathbf{A} & \mathbf{B} \\ \mathbf{A}^* & \mathbf{B}^* \end{pmatrix} \begin{pmatrix} \mathbf{X} \\ \mathbf{Y} \end{pmatrix} = \omega \begin{pmatrix} \mathbf{1} & \mathbf{0} \\ \mathbf{0} & -\mathbf{1} \end{pmatrix} \begin{pmatrix} \mathbf{X} \\ \mathbf{Y} \end{pmatrix} \quad (4.73)$$

where the  $\mathbf{X}$  and  $\mathbf{Y}$  matrices contain the real  $x_a^i$  and imaginary  $y_a^i$  components of the linear response of the wavefunction, which describe how the perturbation modifies the starting GS. Such a modification is defined as an orbital transformation which mixes  $\{\phi_a\}$  with  $\{\phi_i\}$ , and therefore the  $x_a^i$  element describes the mixing between the  $a$ -th occupied and the  $i$ -th virtual MOs. This MOs transformation is equivalent to describe the perturbed wavefunction as a linear combination of the starting GS Slater determinant  $\Psi_0$  with a singly-excited determinant  $\Psi_a^i$  in which one electron is promoted from the  $a$ -th to the  $i$ -th MO:

$$\Psi_0 \rightarrow \Psi_0 + x_a^i \Psi_a^i \quad (4.74)$$

Therefore, the elements of the eigenstates  $\mathbf{X}$  and  $\mathbf{Y}$  describe the molecular ESs (one for each eigenvalue) as sets of  $x_a^i$  coefficients each one quantifying a specific transition of the kind  $\phi_a \rightarrow \phi_i$ . The solution of the above equations constitutes the framework of the *Time-Dependent Hartree-Fock* (TD-HF) theory.

### Time-Dependent Density Functional Theory.

Since also the KS-DFT formulation makes use of a Slater determinant, the same framework of the TD-HF theory can be applied to set up the *Time-Dependent Density Functional Theory* (TD-DFT) [85, 86, 87]. The equations for calculating the transition energies have the same form of those of section 4.1.7 but with  $\mathbf{A}$  and  $\mathbf{B}$  matrices having matrix elements

$$A_{ab}^{ij} = \delta_{ab} \delta_{ij} (\epsilon_i - \epsilon_a) + \langle \phi_a \phi_b | 1/r_{12} | \phi_i \phi_j \rangle - \langle \phi_a \phi_b | f_{XC} | \phi_i \phi_j \rangle \quad (4.75)$$

$$B_{ab}^{ij} = \langle \phi_a \phi_b | 1/r_{12} | \phi_i \phi_j \rangle - \langle \phi_a \phi_b | f_{XC} | \phi_j \phi_i \rangle \quad (4.76)$$

where  $f_{XC}$  is the so called *XC kernel*:

$$f_{XC}(\mathbf{r}_1, \mathbf{r}_2, t_1, t_2) = \frac{\delta V_{XC}[\rho(\mathbf{r}_1, t_1)]}{\delta \rho(\mathbf{r}_2, t_2)} = \frac{\delta^2 E_{XC}[\rho(\mathbf{r}_1, t_1)]}{\delta \rho(\mathbf{r}_1, t_1) \delta \rho(\mathbf{r}_2, t_2)} \quad (4.77)$$

In order to significantly reduce the computational cost, the *adiabatic approximation*, which consists in a total neglecting of the time dependence in the XC kernel, is always considered:

$$f_{XC}^{adia}(\mathbf{r}_1, \mathbf{r}_2) = \frac{\delta V_{XC}[\rho(\mathbf{r}_1)]}{\delta \rho(\mathbf{r}_2)} \quad (4.78)$$

In hybrid functionals, where an amount  $\alpha$  of HF exchange is inserted within the XC functional, the **A** and **B** matrix elements become [88]

$$A_{ab}^{ij} = \delta_{ab}\delta_{ij}(\epsilon_a - \epsilon_b) + \langle \phi_a \phi_b | 1/r_{12} | \phi_i \phi_j \rangle - \alpha \langle \phi_a \phi_i | 1/r_{12} | \phi_b \phi_j \rangle - \langle \phi_a \phi_b | f_{XC} | \phi_i \phi_j \rangle \quad (4.79)$$

$$B_{ab}^{ij} = \langle \phi_a \phi_b | 1/r_{12} | \phi_i \phi_j \rangle - \alpha \langle \phi_a \phi_b | 1/r_{12} | \phi_j \phi_i \rangle - \langle \phi_a \phi_b | f_{XC} | \phi_j \phi_i \rangle \quad (4.80)$$

where  $f_{XC}$  contains in this case a  $1 - \alpha$  coefficient weighting the DFT exchange. When RSH functionals are instead considered, such matrix elements read:

$$A_{ab}^{ij} = \delta_{ab}\delta_{ij}(\epsilon_a - \epsilon_b) + \langle \phi_a \phi_b | 1/r_{12} | \phi_i \phi_j \rangle - \langle \phi_a \phi_i | erf(\gamma r_{12})/r_{12} | \phi_b \phi_j \rangle - \langle \phi_a \phi_b | f_{XC} | \phi_i \phi_j \rangle \quad (4.81)$$

$$B_{ab}^{ij} = \langle \phi_a \phi_b | 1/r_{12} | \phi_i \phi_j \rangle - \langle \phi_a \phi_b | erf(\gamma r_{12})/r_{12} | \phi_j \phi_i \rangle - \langle \phi_a \phi_b | f_{XC} | \phi_j \phi_i \rangle \quad (4.82)$$

where  $f_{XC}$  contains a DFT exchange calculated as discussed in section 4.1.5.

#### 4.1.8 Excited State Analysis: Natural Transition Orbitals

As discussed in section 4.1.7, ESs calculated at TD-DFT level are basically described by a set of  $x_a^i$  coefficients quantifying the transition from the  $a$ -th occupied to the  $i$ -th virtual MOs, which can be in turn associated to the mixing of Slater determinants given by eq.(4.74). A fundamental information for characterizing each ES is given by how the excitation modifies the electronic state with respect to the GS, highlighting in particular whether the excitation transfers electrons from a certain spatial region to another. A quantity that can in principle allow to readily visualize such a variation is the *transition density*, which represents the electron density variation associated to the excitation and is calculated as

$$\rho_T(\mathbf{r}_1) = \sum_{a,i} x_a^i \int \cdots \int \Psi_0^*(\mathbf{r}_1, \mathbf{r}_2, \dots, \mathbf{r}_N) \Psi_a^i(\mathbf{r}_1, \mathbf{r}_2, \dots, \mathbf{r}_N) d\mathbf{r}_2 \dots d\mathbf{r}_N \quad (4.83)$$

Nevertheless, the fact that MOs are often delocalized on the whole molecule along with the fact that typically different MO couples contribute to the same transition makes such an ES analysis far from trivial. A powerful tool to address such a problem is provided by the calculation of *Natural Transition Orbitals* (NTOs) [89], which are obtained through a procedure aimed at reducing as much as possible the number of occupied-virtual MOs couples needed for describing the excitation. Therefore, NTOs necessarily represent MOs delocalized only over those molecular regions that are strictly involved in the excitation. NTOs are calculated starting from the *transition density matrix* having elements calculated on the occupied and virtual MOs:

$$T_{ai} = \langle \phi_a | \rho_T | \phi_i \rangle \quad (4.84)$$

Since virtual MOs are normally higher in number than occupied ones, the **T** matrix having dimension  $N_{occ} \times N_{virt}$  is rectangular, and any rectangular matrix can be rewritten in the form [90]

$$\mathbf{T} = \mathbf{U} \mathbf{\Lambda} \mathbf{V}^\dagger \quad (4.85)$$

where  $\mathbf{U}$  and  $\mathbf{V}$  are  $N_{occ} \times N_{occ}$  and  $N_{virt} \times N_{virt}$  matrices which diagonalize  $\mathbf{T}\mathbf{T}^\dagger$  and  $\mathbf{T}^\dagger\mathbf{T}$ , respectively, while  $\mathbf{\Lambda}$  is a diagonal matrix containing the square root of the  $N_{occ}$  eigenvalues of  $\mathbf{T}\mathbf{T}^\dagger$ , which can be proved to be identical to the first  $N_{occ}$  eigenvalues of  $\mathbf{T}^\dagger\mathbf{T}$ :

$$\mathbf{U}^\dagger\mathbf{T}\mathbf{T}^\dagger\mathbf{U} = \mathbf{\Lambda}_U \quad (4.86)$$

$$\mathbf{V}^\dagger\mathbf{T}^\dagger\mathbf{T}\mathbf{V} = \mathbf{\Lambda}_V \quad (4.87)$$

where  $\mathbf{\Lambda}_U$  and  $\mathbf{\Lambda}_V$  are diagonal matrices with dimension  $N_{occ} \times N_{occ}$  and  $N_{virt} \times N_{virt}$ , respectively, and

$$\mathbf{\Lambda}_U = \mathbf{\Lambda}^2 \quad (4.88)$$

$$(\mathbf{\Lambda}_V)_{aa} = (\mathbf{\Lambda}_U)_{aa} \quad a = 1, 2, \dots, N_{occ} \quad (4.89)$$

Another important property is that the sum of  $\mathbf{\Lambda}$  matrix elements is equal to 1, and such a value can be therefore interpreted as the number of electrons which are excited (that is, 1). The fact that  $\mathbf{T}\mathbf{T}^\dagger$  and  $\mathbf{T}^\dagger\mathbf{T}$  share exactly the same eigenvalues means that the eigenvectors contained in  $\mathbf{U}$  and in the first  $N_{occ}$  columns of  $\mathbf{V}$  are somehow correlated, and since  $\mathbf{U}$  and  $\mathbf{V}$  are transformation matrices that can be applied to occupied and virtual MOs, respectively, to give new sets of MOs, the physical sense of such a correlation falls on these new MOs, which are referred to as NTOs and are calculated as

$$\phi_{occ}^{NTO} = \phi_{occ}\mathbf{U} \quad (4.90)$$

$$\phi_{virt}^{NTO} = \phi_{virt}\mathbf{V} \quad (4.91)$$

where  $\phi_{occ}$  and  $\phi_{virt}$  are row vectors containing the starting MOs. In particular, by keeping the  $a,i$  index notation for occupied and virtual MOs, respectively, the whole procedure consists in a  $\phi_a^{NTO}-\phi_i^{NTO}$  mapping which associates to each  $a = i$  couple the value  $(\mathbf{\Lambda})_{aa}$ , and since such a value corresponds to a fractional number of excited electrons,  $\phi_a^{NTO}$  and  $\phi_i^{NTO}$  represent the MOs describing the transition for such a fraction. Typically, the  $\mathbf{\Lambda}$  matrix has the first value close to 1 and the others close to 0, and that means that NTOs allow to map each excitation (originally described by several transition among MOs) onto a simpler transition involving only two MOs.

#### 4.1.9 Charge Transfer States in Time-Dependent Density Functional Theory

*Charge Transfer* (CT) states can be generally defined as those ES in which there is a pronounced spatial redistribution of electrons with respect to the GS. CT states are typically found in large molecules, where the excitation can move electron density from a certain molecular region to another region spatially separated from it, or in donor-acceptor systems formed by close molecules, where the excitation can move an electron from one molecule (the donor, D) to the other (the acceptor, A).

The TD-DFT ability to describe the CT states has been extensively studied over the years, and several critical issues related to the use of the various functionals have been straightforwardly individuated [91, 92, 93]; in following sections, such problems and the strategies proposed to solve them are briefly summarized and discussed.

### Drawbacks of Local and Semi-Local Functionals.

To highlight the TD-DFT deficiencies, it is worth comparing its results with those obtained from the TD-HF theory. Considering the case of a D-A system for which is assumed a simple CT transition involving only two MOs, that is, the donor's HOMO  $\phi_D$  and the acceptor's LUMO  $\phi_A$ , the excitation energies obtained from the TD-HF and TD-DFT reads [85, 92]:

$$\omega_{CT}^{TDHF} = \varepsilon_A^{HF} - \varepsilon_D^{HF} + 2 \langle \phi_D \phi_A | 1/r_{12} | \phi_A \phi_D \rangle - \langle \phi_D \phi_A | 1/r_{12} | \phi_D \phi_A \rangle \quad (4.92)$$

$$\omega_{CT}^{TDDFT} = \varepsilon_A^{KS} - \varepsilon_D^{KS} + 2 \langle \phi_D \phi_A | 1/r_{12} | \phi_A \phi_D \rangle - \langle \phi_D \phi_D | f_{xc} | \phi_A \phi_A \rangle \quad (4.93)$$

In order to reproduce the TD-HF results, the  $\langle \phi_D \phi_D | f_{xc} | \phi_A \phi_A \rangle$  integral in eq.(4.93) should (i) account for the coulomb interaction described by the last term in eq.(4.92) and (ii) provide a correction to the  $\varepsilon_A^{KS} - \varepsilon_D^{KS}$  value (in general, KS orbital energies are not reliable approximations for HF ones). A serious issue is that since  $\phi_D$  and  $\phi_A$  are localized on different molecules, their vanishing overlap makes vanishing also the  $\langle \phi_D \phi_D | f_{xc} | \phi_A \phi_A \rangle$  integral unless  $f_{xc}$  increases in a quasi-singular manner in the region where the  $\phi_D$  and  $\phi_A$  tails slightly overlap. But if looking at the XC kernel expression, eq.(4.77), one can immediately realize that (semi)local functionals cannot accomplish this task [91]: indeed, since the electron density is local, the derivative  $\delta V_{xc}[\rho(\mathbf{r}_1, t_1)]/\delta \rho(\mathbf{r}_2, t_2)$  is non-vanishing only when  $\mathbf{r}_1 \sim \mathbf{r}_2$  and in regions of space in which the density is appreciable, which is not the case of the overlap region between  $\phi_D$  and  $\phi_A$ . Another way for increasing the derivative value would come from the temporal dependence, but also this possibility is eliminated because of the the adiabatic approximation (4.78). In conclusion, the locality of the XC kernel represents an insurmountable problem for correctly describing CT excitations because it makes impossible not only to recover the TD-HF results, but also to account for any kind of inter-electronic interactions when the transition involves non-overlapping orbitals!

A further serious issue concerns the lack of physical meaning of the KS orbitals, and the impact of this deficiency can be easily highlighted upon considering the ideal case of an infinitely separated D-A system for which (since any D-A interaction can be neglected) the CT excitation energy trivially becomes

$$\omega_{CT} = IP_D - EA_A \quad (4.94)$$

Since for such a system the overlap between  $\phi_D$  and  $\phi_A$  is zero, eq.s (4.92) and (4.93) reduce respectively to  $\omega_{CT}^{TDHF} = \varepsilon_A^{HF} - \varepsilon_D^{HF}$  and  $\omega_{CT}^{TDDFT} = \varepsilon_A^{KS} - \varepsilon_D^{KS}$ , and while Koopmans theorem (4.21) and (4.22) ensures eq.(4.94) to be fulfilled in TD-HF, this is not the case for TD-DFT. In particular, it has been shown that even for the exact KS functional, for which the condition (4.21) always holds [94], condition (4.22) cannot be satisfied due to an intrinsic error of KS theory: the energy given by the exact functional expressed as a function of the fractional number of electrons corresponds to a sequence of straight segments presenting derivative discontinuities at the integer values of electrons [95], and the LUMO's energy is always overestimated with respect to EA by a quantity equal to the derivative discontinuity value [96]. Regarding the approximate (semi)local functionals, they do not present the required discontinuities [97] and this fact is responsible for a systematic error also for HOMO energy other than LUMO [98].

### Improvements From Hybrid and RSH Functionals.

Regarding the inter-electronic interactions issue discussed in the previous section, the use of hybrid functionals represents an important improvement: indeed, by comparing the **A** and **B** matrix elements associated to local, eq.s (4.75) and (4.76), and hybrid functionals, eq.s (4.79) and (4.80), is evident that the fraction of HF exchange has the effect of introducing in such matrix elements the coulomb interaction between electrons associated to non-overlapping orbitals (which is the term multiplied by  $\alpha$ ). Nevertheless, CT excitations still remain problematic, because to get the *correct asymptotic behaviour* for the energy of very separated charges given by  $1/R$  (coulomb law), the HF exchange should be 100% of the total exchange (that is,  $\alpha = 1$ ) and such an amount has been shown to strongly worsen TD-DFT calculations.

The problem of the correct asymptotic behaviour can be easily overcome by using RSH functionals, in which parameters can be set to provide 100% of HF exchange at LR only, thus ensuring the presence of a certain amount of DFT exchange at SR. Such a requirement is automatically fulfilled when considering the simple splitting of eq.(4.52), and can be imposed also when considering the more sophisticated splitting of eq.(4.55) by setting  $\alpha + \beta = 1$ , which basing on eq.(4.56) leads to 100% HF and 0% of DFT exchanges at LR.

Despite the improved description of inter-electronic interactions in CT states, the lack of physical meaning of KS orbital energies still represents an issue. Indeed, there are no theoretical arguments indicating that the use of generic hybrid or RSH functionals could provide any improvement in this regard; nevertheless, RSH functionals have been showed to represent the fundamental ingredient for developing a strategy to finally fix the problem of orbital energies, which is presented and extensively discussed in the next sections.

### Improvements From Optimally-Tuned RSH Functionals.

A very conceptually simple strategy for solving the problem of the reliability of KS orbital energies has been proposed by R. Baer and collaborators [99], who presented a tuning procedure for the parameters of RSH functionals aimed to force the Koopmans theorem for KS HOMO and LUMO energies; the new functionals obtained through such an optimization are commonly referred to as the *optimally-tuned* RSH (opt-RSH) functionals. In the original work, authors considered the simple splitting given by eq.(4.52) and performed the tuning on the  $\gamma$  parameter to reproduce the experimental CT excitation energies for D-A systems composed by aromatic molecules (D) and tetracyanoethylene (A). To avoid the troubles associated to the LUMO energy predicted at the TD-DFT level (see section 4.1.9), the tuning have been performed by replacing the LUMO of the normal acceptor (neutral molecule having  $N_A$  electrons) with the HOMO of the acceptor bearing an additional electron (anionic molecule having  $N_A + 1$  electrons). The procedure for obtaining the optimal  $\gamma$  parameter consists in minimizing the following function:

$$J^2(\gamma) = \left[ \varepsilon_{D(N_D)}^{HOMO} - IP_{D(N_D)} \right]^2 + \left[ \varepsilon_{A(N_A+1)}^{HOMO} - IP_{A(N_A+1)} \right]^2 \quad (4.95)$$

where IPs are simply calculated from GS DFT calculations as

$$IP_{D(N_D)} = E_{D(N_D-1)} - E_{D(N_D)} \quad (4.96)$$

$$IP_{A(N_A+1)} = E_{A(N_A)} - E_{A(N_A+1)} \quad (4.97)$$

The optimal tuning has been extended also to CAM RSH functionals, for which the correct asymptotic behaviour has been found to be a crucial requirement for getting correct results [100].

Despite also standard RSH functionals are sometimes able to predict rather good CT excitation energies [101], opt-RSH has been demonstrated to systematically improve not only CT excitation energies in separated D-A systems [99, 102] but also the absorption energies of single molecules, ranging from simple molecules having almost fully localized bright states [104, 103] to covalently linked D-A systems considered as a whole as single molecules [105]. This means that the forcing of Koopmans theorem for frontier orbitals can be considered a kind of universal criterion to ameliorate the density functionals for the calculation of transition energies, independently from the ES character: for example, the optimal tuning has been showed to improve also singlet-triplet gaps in OLEDs [100, 106], a fundamental quantity governing the possibility of delaying the fluorescence lifetime of the dye thanks to a reversible inter-system crossing process involving a triplet ES very close in energy to singlet one.

### Improvements From Including Solvation Effects in Optimally-Tuned RSH Functionals.

When solvated systems are considered, a question which immediately arises is whether including the solvent effect within the optimal tuning procedure or not. Despite several possibilities for coupling the optimal tuning and the inclusion of the dielectric screening given by the solvent have been critically analyzed [107], an universal tuning strategy has not been emerged yet.

The most simple strategy consists in performing all calculations required for the tuning by using the PCM model, thereby forcing orbital energies to equal IPs within solvent. This method has been judged quite untrustworthy because of the fact that it leads to extremely low optimal  $\gamma$  values [108, 109] (corresponding to an unphysical introduction of HF exchange only at very high distances) which for the case of oligothiophenes have been showed to both underestimate [108] or overestimate [109] transition energies. Such low optimal  $\gamma$  values are due to the fact that PCM decreases the IP value but leaves the HOMO energy almost unaffected, and since both IP and  $-\varepsilon_{HOMO}$  are increasing function of  $\gamma$ , the condition  $\varepsilon_{HOMO} = -IP$  is fulfilled at lower  $\gamma$  values [108]. But despite this critical point, the optimal tuning within solvent has been used to predict extremely precise transition energies for small multimers of the MEH-PPV polymer [110].

A more prudent strategy consists in tuning the functional for the molecule in vacuum and then adding PCM in later calculations: this recipe has been showed to provide higher optimal  $\gamma$  values with respect to the tuning within solvent [108, 109], but these increased values do not always ensure an improvement for transition energies. Indeed, studies performed on extensive sets of test molecules showed that in certain cases the optimal tuning in vacuum ameliorates transition energies, while in other cases is not able to provide any improvement [100, 109].

A more sophisticated tuning strategy has been proposed for CAM functionals with the aim of including the solvent screening but avoiding the problems related to the tuning within

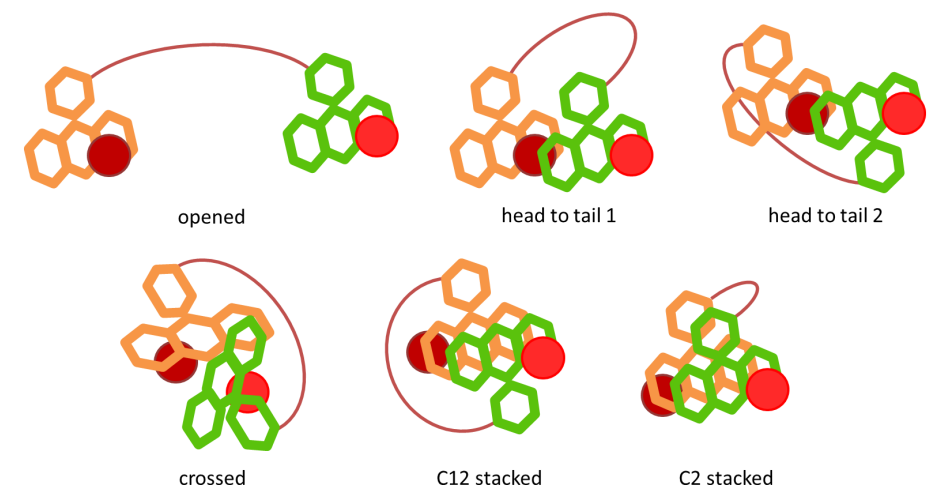


**Figure 4.3:** The guess RB-C-RB conformations considered as starting points for DFT geometry optimizations. The red spheres represent the counterions (F5TPB and  $\text{Cl}^-$ ).

solvent: such functionals are referred to as *Screened Optimally-Tuned Range-Separated Hybrid* (S-opt-RSH) functionals [111, 112], and the tuning strategy is based on exploiting the  $\alpha, \beta$  parameterization to include the solvent screening. The procedure consists in a preliminary tuning in vacuum to determine the optimal  $\gamma$  (which is typically performed testing different starting  $\alpha$  and  $\beta$  couples and considering the correct asymptotic behaviour  $\alpha + \beta = 1$ ) followed by a second tuning in solvent aimed to optimize  $\alpha$  and  $\beta$ . This second tuning consists in an  $\alpha$  scanning (with  $\gamma$  fixed to its optimal value in vacuum) in which  $\beta$  is each time reset to fulfill the condition

$$\alpha + \beta = \frac{1}{\epsilon} \quad (4.98)$$

which represents the correct asymptotic behaviour in presence of the dielectric screening operated by the solvent via its dielectric constant  $\epsilon$  (that is, the Coulomb law within a dielectric medium). S-opt-RSH functionals has been showed to give correct orbital ordering [111] and to ameliorate the CT transition energies with respect to non-screend opt-RSH functionals when used on D-A systems composed by anthracene derivatives (D) and tetracyanoethylene (A).

## 4.2 DFT Investigations on Rhodamine B Dimerization

### 4.2.1 Geometrical Conformations of Rhodamine B Dimers

In order to confirm the experimental insights discussed in previous sections, several RB-C-RB conformations have been analyzed by means of DFT calculations aimed to quantify how

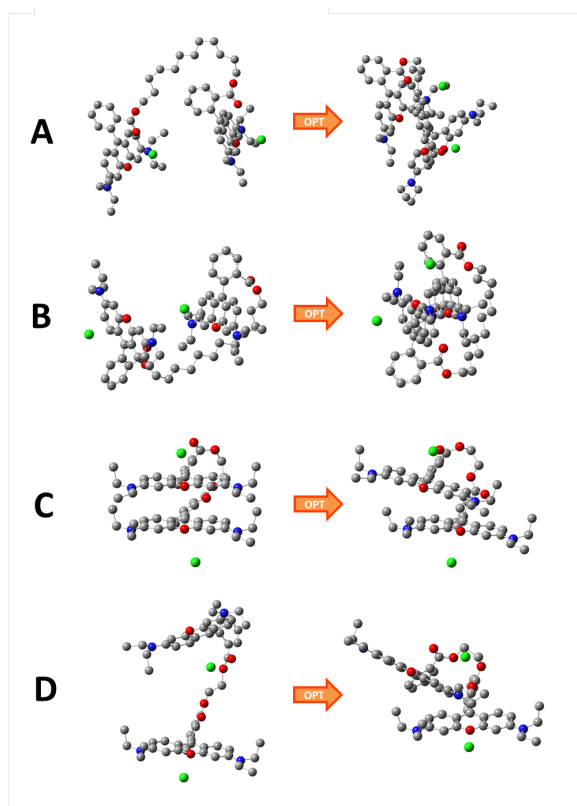


**Figure 4.4:** Results of geometry optimizations for RB-C-RB conformations in presence of the  $\text{Cl}^-$  counterion. (A) Head to tail 1 conformation with C12 linker. (B) Head to tail 2 conformation with C12 linker. (C) Stacked conformation with C2 linker. (D) Head to tail conformation with C2 linker.

counterions affect their stability. The different conformations have been obtained from the set of guess structures depicted in figure 4.3 (the red spheres indicating the counterions), which have been used as starting geometries for DFT geometry optimizations. The set comprises a conformation in which the RBs are completely separated (*opened* structure), the counterions act as spacer (*head to tail* structures), a *crossed* conformation which is likely to be formed in solution [113, 114] and a *stacked* structure. It is worth noting that for such structures a classification purely in terms of H and J dimers could be misleading. Indeed, basing on exciton theory, H dimers require the xanthene planes of the two RBs to be parallel (see section 1.1), and such a condition can be satisfied with and without the spacing given by the counterion (for example, H dimers can be formed in both *stacked* and *head to tail* conformations), while all conformations in which xanthene are not parallel can be in principle classified as J dimers. In the present analysis, dimers are defined as those conformations in which the two RBs are very close in space, i.e. it is assumed that the spacing given by the counterion (actually F5TPB only) is wide enough to prevent the RB-

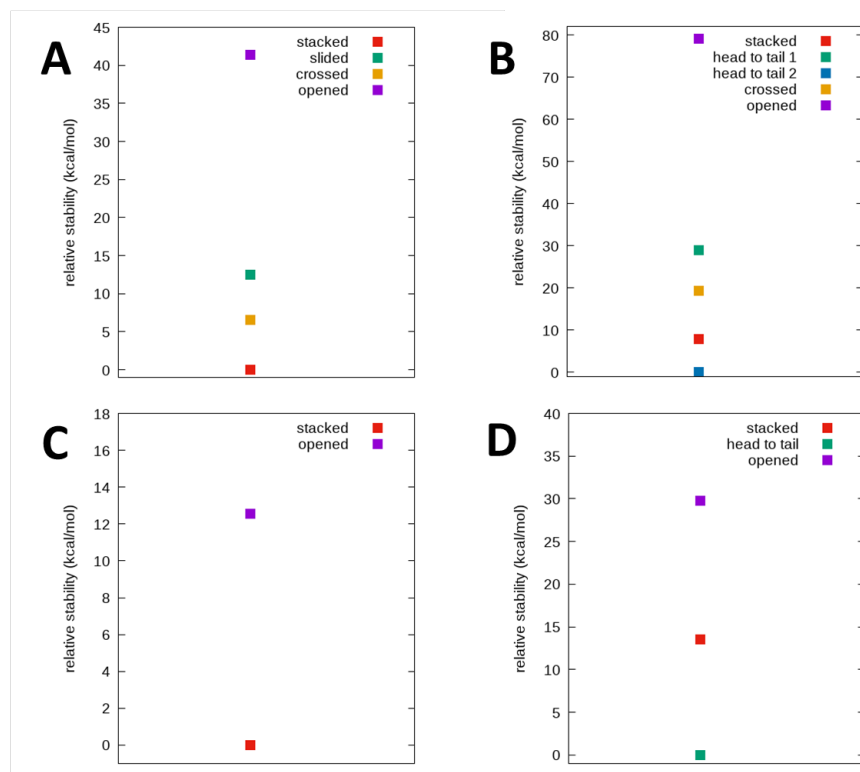


**Figure 4.5:** Relative stabilities of optimized RB-C-RB conformations. (A) C12 linker with Cl<sup>-</sup> counterion. (B) C12 linker with F5TPB counterion. (C) C2 linker with Cl<sup>-</sup> counterion. (D) C2 linker with F5TPB counterion.

RB electronic interaction (or coupling) which gives rise to the exciton formation (i.e., the formation of real H and J dimers). Regarding the comparison between the two linkers, the lower flexibility given by the C2 chain does not allow to consider the same conformations tested for the C12 one. In particular, the C2 chain is not long enough to build the *head to tail 1* and the *crossed* structures. Moreover, two different *stacked* conformations (both indicated in figure 4.3) have been considered for the two linkers: i) a structure having the two phenyl groups on different sides has been chosen for the C12 chain, given its flexible chain, while ii) a structure having the two phenyls on the same side is instead considered for the C2 chain. Geometry optimizations have been performed using the B3LYP functional with the D3 correction for dispersion interactions, the 6-31G\* basis set and by including the solvent (dioxane) at the CPCM level.

#### Dimers with C12 Linker Chain

The comparison of DFT geometry optimization results for conformations containing the two counterions clearly reveals the ability of F5TPB to act as a spacer for RBs. Indeed,

optimizations keep basically unchanged all the guess structures of figure 4.3 when F5TPB is considered, and the important result here is that the *head to tail* 1 and 2 conformations, having the counterion intercalated between RBs, represent stable structures (in other words, F5TPB is not moved away during the optimization). Instead, when considering the  $\text{Cl}^-$  counterion a different picture arises, because while the *stacked* and *crossed* conformations keep their guess geometries (stable structures), the intercalated structures are deeply modified during the optimization. As reported in Figure 4.4, the *head to tail* 1 relaxes to a conformation in which the two xanthene planes (originally parallel) are significantly slid (figure 4.4A) while the *head to tail* 2 relaxes to a stacked conformation in which the  $\text{Cl}^-$  counterion is removed from the space between RBs (figure 4.4B). The fact that *head to tail* 1 does not relax to a stacked form is to be imputed to the relative position of the phenyl groups that, being on the same side, would lead to a too distorted chain arrangement in the stacked form. But this is not the case for *head to tail* 2, in which the xanthene stacking is indeed formed, thereby demonstrating the inability of the small  $\text{Cl}^-$  counterion to act as a spacer.

The relative stabilities of the optimized conformations (given by the energy differences separating their DFT GS from the one of the most stable conformation) are reported in Figure 4.5. The first relevant finding is that all conformations are very stabilized with respect to the *opened* structures, indicating that RBs always tend to be stabilized by interacting each other and independently from the nature of the counterion. The second and most important finding is that the comparison between the two counterions allows to finally justify and quantify the ability of F5TPB to act as an efficient spacing agent for the dyes. In fact, when the  $\text{Cl}^-$  counterion is considered, the *stacked* structure is found to be the most stable conformation (figure 4.5A), but when  $\text{Cl}^-$  is replaced with F5TPB the most stable conformation becomes the *head to tail* 2 conformation (figure 4.5B), confirming that the RB-F5TPB interactions stabilize the intercalated form with respect to the stacked one. These results are fully in line with the experimental FQY measurements, from which one expects the stacked form (representing a quenching species) to be the most stable in presence of  $\text{Cl}^-$  but not in the presence of F5TPB.

### Dimers with C2 Linker Chain

For the short C2 linker chain, basically the same results of the C12 case have been found. First of all, the geometry optimizations keep unaltered the guess structures only with F5TPB, while the *head to tail* conformation relaxes to a stacked structure when considering  $\text{Cl}^-$  (figure 4.4D). Regarding the stacked conformation, it is worth noting that the stiffness given by the very short linker does not allow to reach a complete stacking between the two xanthene planes, which differently from the C12 case (maintaining the fully stacked arrangement), get slight shifted each other during the optimization (figure 4.4C). Moreover, such slid structure is also that formed starting from the *head to tail* conformation. Notably, the stabilization given by the spacing action of F5TPB can be clearly observed by comparing the relative stabilities of structures containing the two different counterions: while for the  $\text{Cl}^-$  case the most stable structure is the stacked one (figure 4.5C), the most stable structure for F5TPB is that having the counterion intercalated between the two RBs (figure 4.5D).

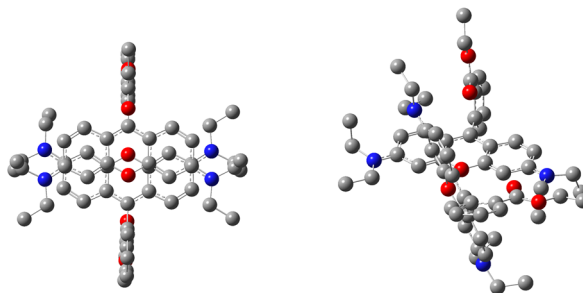


**Figure 4.6:** Molecular structures of H (left) and crossed J (right) dimers used for TD-DFT calculations (geometries have been optimized at the DFT/B3LYP-D3/6-31G\* level).

#### 4.2.2 TD-DFT Investigations on Rhodamine B Dimers Excited States

In order to investigate the optical and photophysical properties of different dimer conformations and, in particular, to confirm the experimental evidence concerning the possibility of having fluorescence from J dimers and quenching from H dimers, TD-DFT ES calculations have been performed by considering a simplified dimer model. Such model neglects both counterions and linker chain, with the monomer unit being chosen to be a simple RB ethyl ester. For the J dimer the crossed configuration presented in Figure 4.3 has been chosen, while for the H dimer the stacked configuration has been obviously considered. The guess geometries have been optimized at the DFT/B3LYP-D3/6-31G\* level with dioxane solvent described with the CPCM method. The resulting optimized structures are reported in Figure 4.6. Dimers typically present CT ESs describing a transfer of electron density between the monomer units. Since these states are normally dark, they can provide quenching channels, with population transfer from the fluorescent bright state (referred to as *Locally Excited* state, LE) to the CT dark state happening via internal conversion processes. Therefore, a good description of the CT states energies (especially with respect to LE ones) is crucial for correctly simulating the photophysical properties of dimers.

Basing on the discussion of Section 4.1.9, DFT functionals of different kind have been compared for studying how the CT states are affected by the inclusion of HF exchange with and without range-separation and, most importantly, by performing the optimal tuning with and without including the screening from the solvent. Two functional families have been compared: the first family comprises the hybrid, RSH and opt-RSH versions of the functional exploiting the B88 exchange with the LYP correlation, while the second comprises the same versions but related the PBE exchange-correlation functional. The full list of tested functionals is:

- **Standard hybrid functionals:** B3LYP and PBE0.
- **Standard RHS functionals:** CAM-B3LYP and LC-PBE.
- **$\gamma^*$ RHS functionals:** optimally tuned versions of CAM-B3LYP and LC-PBE in which

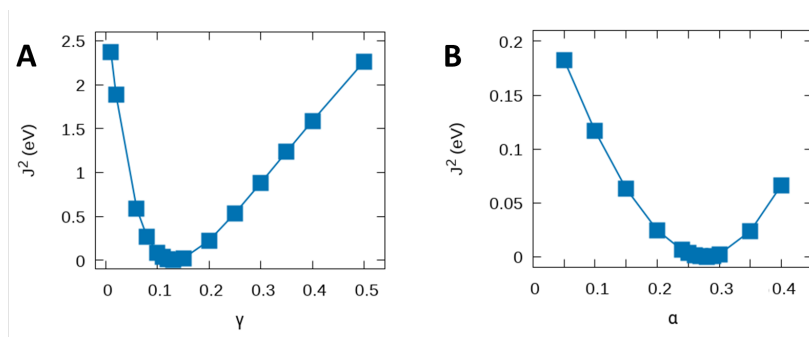


**Figure 4.7:** (A)  $\gamma$  optimal-tuning leading to the  $\gamma^*$ CAM-B3LYP functional ( $\alpha = 0.2$ ,  $\beta = 0.8$ ). (B)  $\alpha$  optimal-tuning leading to the S- $\gamma^*\alpha^*$ CAM-B3LYP functional ( $\gamma = 0.13$ ).

$\gamma$  is tuned in vacuum using  $\alpha$  and  $\beta$  fulfilling the correct asymptotic behaviour ( $\alpha + \beta = 1$ ).

- **S- $\gamma^*\alpha^*$ RHS functionals:** screened optimally tuned versions of CAM-B3LYP and LC-PBE in which  $\gamma$  is tuned in vacuum (same procedure of  $\gamma^*$ RHS functionals) and  $\alpha$  is further tuned within solvent including the dielectric screening, that is, by imposing  $\alpha + \beta = 1/\epsilon$  (see section 4.1.9).

While tuning has been performed using the 6-31G\* basis set, ES calculations have been performed by using the more extended 6-311+G\* within dioxane at the CPCM level.

### Optimally-Tuned Parameters.

The optimal  $\gamma$  values obtained from the CAM-B3LYP and LC-PBE tuning in vacuum are summarized in table 4.1, and the typical shape of the  $J^2$  function, eq.(4.95), is showed in Figure 4.7A. The  $\alpha, \beta$  couples have been fixed basing on literature suggestions, which commonly recommend small  $\alpha$  values (as more reliable) [107]. A very striking result is that the HF exchange seems to play a kind of universal role in satisfying the Koopmans theorem: indeed, the  $\alpha = 0$  and  $\beta = 1$  combination, for which no SR HF exchange is considered, is the only one leading to different optimal parameters for CAM-B3LYP and LC-PBE. When SR HF exchange is inserted, both functionals lead to almost identical optimal values (see Table 4.1), a results that has been already reported in literature [100]. This means that when an even very small fraction of SR exact exchange (5%) is set into the functional, the different nature of DFT exchange of the two functionals (i.e., B88 and PBE) does not have any influence on the tuning. All the tested  $\alpha, \beta$  couples allow for a satisfactorily fulfilling of the Koopmans theorem, and the associated optimal  $\gamma$  values fall in a rather narrow range (0.10-0.17). The value  $\gamma=0.13$  has been chosen for performing the  $\alpha$  tuning within solvent, which leads to the optimal value  $\alpha = 0.28$  (with the associated  $\beta = 1/\epsilon - \alpha = 0.164$ ) for both the CAM-B3LYP (see Figure 4.7.B) and LC-PBE functionals.

## DFT Studies of RB and its Dimers

Functional	$\alpha = 0$ $\beta = 1$	$\alpha = 0.05$ $\beta = 0.95$	$\alpha = 0.1$ $\beta = 0.9$	$\alpha = 0.15$ $\beta = 0.85$	$\alpha = 0.2$ $\beta = 0.8$
$\gamma^*$ CAM-B3LYP	0.10 (0.021)	0.17 (0.047)	0.16 (0.046)	0.14 (0.044)	0.13 (0.020)
$\gamma^*$ LC-PBE	0.18 (0.051)	0.17 (0.047)	0.16 (0.047)	0.14 (0.038)	0.13 (0.020)

**Table 4.1:** Optimal  $\gamma$  parameters obtained from the tuning in vacuum. The corresponding  $J$  minimum values (calculated as the square root of  $J^2$  and expressed in eV) are reported in parenthesis.

Functional	Transition energy (eV)	Functional	Transition energy (eV)
B3LYP	2.59	PBE0	2.64
CAM-B3LYP	2.80	LC-PBE	2.93
$\gamma^*$ CAM-B3LYP	2.69	$\gamma^*$ LC-PBE	2.69
S- $\gamma^*\alpha^*$ CAM-B3LYP	2.70	S- $\gamma^*\alpha^*$ LC-PBE	2.74

**Table 4.2:** RB monomer’s transition energy calculated at the different TD-DFT levels. The experimental value is about 2.21 eV.

### 4.2.3 Rhodamine B Excited States

Table 4.2 reports the RB monomer’s transition energies predicted by the two families of DFT functionals considered. Being the experimental value of the absorption maximum ca. 2.21 eV, it is evident that hybrid functionals give better results, while RSH functionals lead to significant discrepancies, up to 0.6-0.7 eV, in their standard versions. It is worth mentioning that the discrepancy mentioned above include a systematic error, since a direct comparison between computed vertical transition energies and experimental absorption maxima does not take into account the important role of vibronic effects (that could significantly shift the main absorption band with respect to the vertical transition). Since the two  $\gamma^*$ RSH and the two S- $\gamma^*\alpha^*$ RSH functionals give respectively very similar results, one can conclude that also for transition energy calculations the most relevant parameter is the amount of HF exchange, which mostly determines the results. Therefore, the comparison between hybrid and standard RSH functionals allows to speculate about the origin of the error given by the latter. Since B3LYP and CAM-B3LYP introduce almost the same amount of HF exchange at the SR (20% and 19% respectively), a crucial parameter affecting the transition energy turns out to be the HF exchange introduced at the LR (20% and 65%), for which too high amounts represent an important source of error. The situation is even worst when using the LC-PBE, in which the introduction of 0% and 100% of SR and LR HF exchange, respectively, represents a very poor combination. But the very surprising result is that, contrary to what expected from literature, also optimally-tuned RSH functionals are found to be unable to improve significantly the transition energy. The comparison between standard RSH and  $\gamma^*$ RSH functionals allows to indentify a second source of error, i.e. the range-

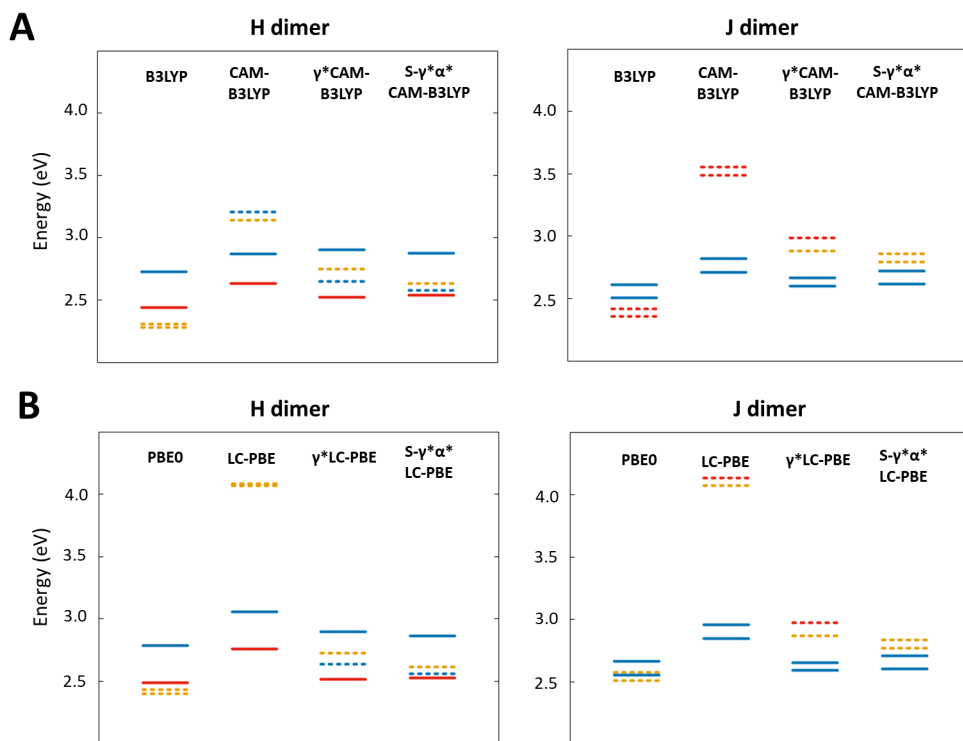


**Figure 4.8:** RB Dimers' ESs calculated at different levels of theory. LE states are indicated with full lines while CT states are indicated with dashed lines. (A) B3LYP family functionals. (B) PBE family functionals.

separation parameter. Indeed, passing from the standard CAM-B3LYP to the  $\gamma^*$ CAM-B3LYP functional, a clear improvement is observed, and since both functionals have almost the same SR HF exchange (19% and 20% respectively) and a rather high LR HF exchange (65% and 100%), such an improvement has to be imputed to the reduction of  $\gamma$  from 0.33 to 0.13, which implies the introduction of LR HF exchange at longer distances. Unfortunately, the comparison between  $\gamma^*$ RSH and S- $\gamma^*\alpha^*$ RSH (which share the same optimal  $\gamma$ ) does not help in shedding further light on the effect of HF exchange. Indeed, the SR amount increase (from 20% to 28%) due to the tuning within solvent is accompanied by a LR amount decrease (from 100% to 44%) given by the screening condition. The fact that the transition energies given by the two functionals are very similar is related to such a compensation.

#### 4.2.4 Rhodamine B Dimers Excited States

The lowest four ESs predicted by the two families of functionals for the H and crossed J dimers are reported in Figure 4.8. In both dimers, two LE and two CT states are found, and the representative NTOs associated to the transition describing the H dimer ESs are

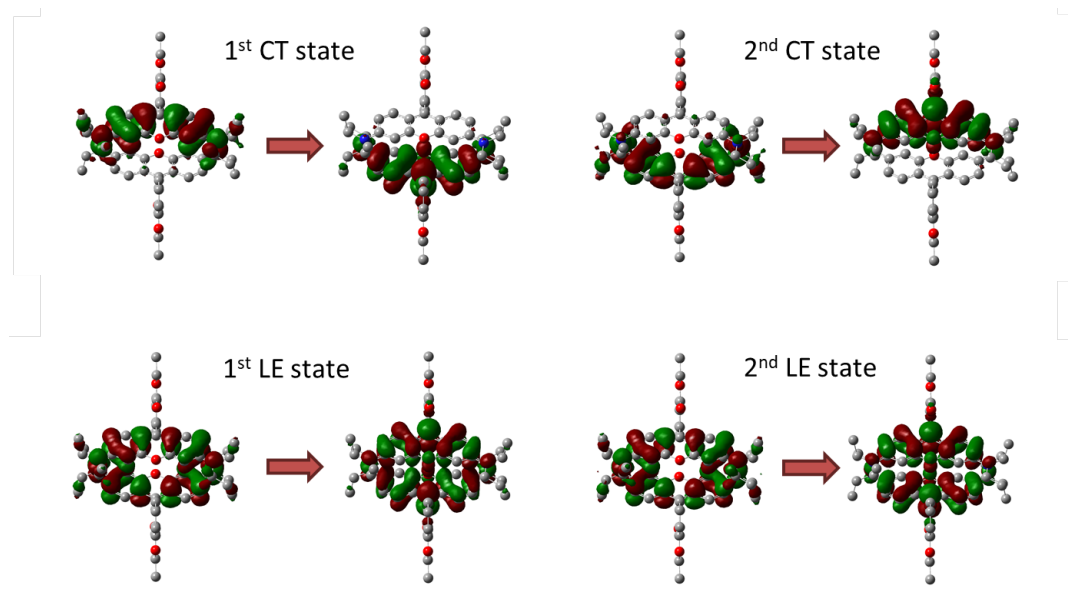


**Figure 4.9:** Typical NTOs (B3LYP calculation) associated to the major transition describing the first four ESs of the H dimer.

depicted in Figure 4.9. All functionals predict oscillator strengths for the LE states that are fully in line with what expected from exciton theory: in the H dimer the lower state is dark and the higher is bright, while in crossed J dimer both states are bright. Moreover, the H dimer main peak is blue shifted with respect to the monomer by a quantity that is quite close to the experimental value (error within 0.08 eV, see Table 4.3), confirming that the stacked conformation is really the species responsible for the rising of the blue-shifted shoulder in the absorption spectra. It is evident that the different functionals in each family predict a very different stabilization for the CT states with respect to LE. Again, the two  $\gamma^*$ RSH and S- $\gamma^*\alpha^*$ RSH functionals give almost identical results, indicating that the amount of HF exchange is the important parameter also for the relative stabilization of CT states, independently from the nature of the DFT counterpart.

The comparison of the various functionals allow to speculate about the kind of HF exchange, since its leading role in affecting the CT states energy. First, a crucial parameter seems to be the HF exchange introduced at the LR level. Indeed, going from B3LYP to CAM-B3LYP, the sensible increase of the LR HF exchange provokes a strong destabilization of the CT states, which are shifted above the LE states, and the same effect is observed also passing from PBE0 to LC-PBE. Moreover, the  $\gamma$  parameter also strongly affect the CT states energies: going from CAM-B3LYP to  $\gamma^*$ CAM-B3LYP, which features almost the same SR HF exchange, the CT states are stabilized by 0.5 eV, and since  $\gamma^*$ CAM-B3LYP has a larger LR HF exchange with respect to CAM-B3LYP, such a stabilization is due to the reduction of  $\gamma$  from 0.33 to 0.13.

Regarding the potential consequences on the RB dimers' photophysical properties, while

Functional	Blue Shift (nm)	Functional	Blue Shift (nm)
B3LYP	0.14	PBE0	0.15
CAM-B3LYP	0.07	LC-PBE	0.13
$\gamma^*$ CAM-B3LYP	0.21	$\gamma^*$ LC-PBE	0.21
S- $\gamma^*\alpha^*$ CAM-B3LYP	0.17	S- $\gamma^*\alpha^*$ LC-PBE	0.12

**Table 4.3:** Blue shift of the H dimer’s main peak with respect to the monomer (eV). The experimental value is about 0.13 eV.

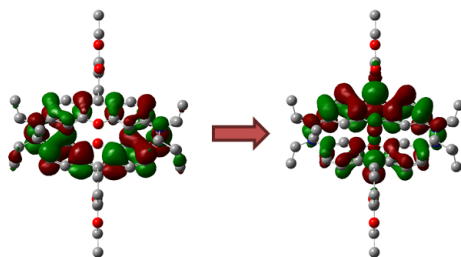


**Figure 4.10:** NTOs describing the bright CT state predicted at the CAM-B3LYP level. The delocalization tails can be easily individuated upon comparing the shape on these orbitals with those characterizing the 2<sup>nd</sup> CT state reported in figure 4.9.

for the H dimer all functionals equally describe the possibility of having fluorescence quenching because of the presence of low lying LE dark state (figure 4.8.A), in order to reproduce the experimental fluorescence in J dimers, calculations should predict the dark CT states to be destabilized above the bright LE states in this case. We observede that only RSH functionals (in both their standard and optimally-tuned versions) can provide such a picture (figure 4.8.B).

The most surprising result arising from figure 4.8 concerns the oscillator strengths associated to the CT states. In the present study, secondary bright states are defined as those having oscillator strengths with a magnitude greater or equal the 10% of the main peak, because such a cutoff value should ensure these secondary peaks to be clearly visible in the simulated absorption spectrum. Since CT states are described by transitions between NTOs localized on different monomers (see figure 4.9) and thus characterized by small overlaps, they are expected to be dark. While this is always the case for the CT states of J dimer, for the H dimer all functionals except B3LYP, PBE0 and LC-PBE predict one of the two CT states to be bright. The oscillator strengths for the CT states are reported in Table 4.4, with the comparison between the two  $\gamma^*$ RSH and the two S- $\gamma^*\alpha^*$ RSH functionals showing that, again, the oscillator strengths are mainly dictated by the amount of HF exchange without any strong dependence on the different kind of DFT exchange employed. The origin of the brightness is readily justified by inspecting the shape of NTOs. In Figure 4.10 are reported

## DFT Studies of RB and its Dimers

Functional	Oscillator strength	Functional	Oscillator strength
B3LYP	0.076 (0.036)	PBE0	0.125 (0.040)
CAM-B3LYP	0.280 (0.021)	LC-PBE	0.026 (0.016)
$\gamma^*$ CAM-B3LYP	0.720 (0.033)	$\gamma^*$ LC-PBE	0.680 (0.027)
S- $\gamma^*\alpha^*$ CAM-B3LYP	0.332 (0.036)	S- $\gamma^*\alpha^*$ LC-PBE	0.310 (0.029)

**Table 4.4:** Oscillator strengths for the bright and dark (in parenthesis) CT states in the H dimer. The B3LYP and LC-PBE functionals are the only predicting low oscillator strengths for both the CT states.

those associated to the CAM-B3LYP calculation, showing that the starting and final orbitals are no longer fully localized on each monomer, but instead present small delocalization tails on the other monomer, leading to a non-vanishing overlap. This CT bright state probably represents a spurious TD-DFT result, because (i) the experimental absorption spectra does not show any absorption peak blue-shifted with respect to the shoulder, which is instead what predicted for instance by CAM-B3LYP and (ii) all functionals predicting a bright CT state lead also to larger discrepancies in the monomer transition energy, and are therefore to be considered as less reliable for correctly describing ESs. The most important point here is that also the optimally-tuned functionals (both with and without including the solvent screening), which are normally considered a formidable tool for ameliorating TD-DFT calculations, has turned out to be absolutely unable to fix the problem of the CT state brightness.

The functionals comparison allow to infer what is the parameter responsible for the presence of this spurious bright CT state. First, one can consider the effect of the LR HF exchange to have a minor role, because the bright CT state is not predicted by the LC-PBE functional which introduces 100% of HF exchange at the LR. Secondly, the effect of the  $\gamma$  parameter can be also excluded because, for example, the comparison between CAM-B3LYP and  $\gamma^*$ CAM-B3LYP clearly shows that the  $\gamma$  reduction does not reduce the oscillator strength. Therefore, the brightness increase is due to the last parameter left, i.e. the SR exact exchange, and an important information can be achieved by comparing the B3LYP and PBE0 functionals: the B3LYP functional, which introduces a 20% of HF exchange at both SR and LR, predicts the CT oscillator strength to be about 2% of the main peak while PBE0, which instead introduces a 25% of HF exchange, predicts an increase to about 8%. This result suggests that the very small increase of 5% associated to the switching from B3LYP to PBE0 suffices to sensibly increase the oscillator strength of the CT state, and since the LR HF exchange has been showed to not affect the brightness, one can conclude that the key effect is to be imputed to the HF exchange amount at the SR.

In order to systematically study the effect the SR HF exchange on the oscillator strength of the CT states in the H dimer, its amount has been manually scanned for both B3LYP and PBE0 functionals. The resulting CT states oscillator strengths are reported in Table 4.5. As expected, the oscillator strength rapidly rises upon increasing the HF exchange amount, thus suggesting that only quite low fractions can ensure the bright CT state problem to be fixed. This finding can explain the fact that also optimally-tuned RSH functionals predict such

B3LYP		PBE0	
HF exchange (%)	Oscillator strength	HF exchange (%)	Oscillator strength
5	0.014 (0.031)	5	0.010 (0.037)
15	0.039 (0.044)	15	0.031 (0.055)
25	0.106 (0.071)	25	0.125 (0.040)
35	0.424 (0.039)	35	0.408 (0.028)
45	1.114 (0.033)	45	1.082 (0.034)
55	1.809 (0.031)	55	1.770 (0.028)

**Table 4.5:** Oscillator strengths for the 1<sup>st</sup> and 2<sup>nd</sup> (in parenthesis) CT states in the H dimer predicted upon manually increasing the HF exchange within B3LYP and PBE0 functionals.

bright CT state: regarding the  $\gamma^*$ RSH functionals, the quite low value of SR HF exchange (20%) does not suffice to lower the brightness because of contributions that could arise from the extremely large LR HF exchange (100%), while for the S- $\gamma^*\alpha^*$ RSH functionals the tuning within solvent leads to a 28% of SR HF exchange, which basing on the above analysis of the HF exchange effect in hybrid functionals clearly represents a too large fraction.

#### 4.2.5 A Novel Strategy for Improving the Excited State Calculation for Rhodamine B and Its Dimers.

To most relevant results concerning the TD-DFT ES calculation for RB and its dimers can be summarized as follows:

- Standard RSH functionals give an extremely poor description of the RB transition energy due to the too large  $\gamma$  values and the too large LR HF exchange amounts.
- Optimally-tuned RSH functionals slightly improve the RB transition energy with respect to standard RSH thanks to their reduced  $\gamma$  values, but errors still remains quite significant.
- Thanks to the proper amount of LR HF exchange, RSH functionals in both their standard and optimally-tuned versions predict CT states lying above the bright LE states in the J dimer, thereby justifying the possibility of having fluorescence.
- The inclusion of a too large fraction of SR HF exchange (indicatively higher than 20-25%) leads to the prediction of a spurious bright CT state in the H dimer.
- Despite having been showed to be the correct method for obtaining improved CT states energies in certain cases [112], the optimal-tuning including the solvent screening is not able to fix the problem of the CT state brightness.

Clearly, the unsatisfactory results given by the  $\gamma^*$ RSH and S- $\gamma^*\alpha^*$ RSH functionals for RB and its dimers suggest that the forcing of Koopmans theorem for DFT MOs cannot be considered an universal successful strategy for obtaining good functionals.

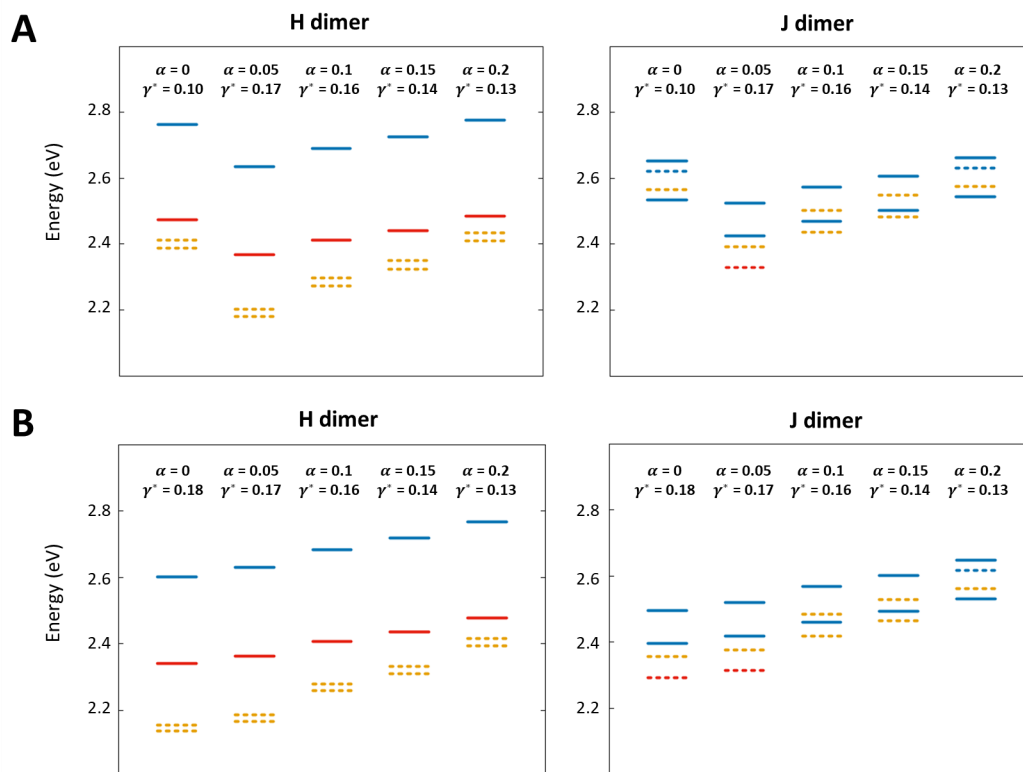


**Figure 4.11:** Dimers' ESs predicted by different couples of  $\alpha, \gamma^*$  values (in all cases  $\beta = 1/\varepsilon - \alpha$ ). LE states are indicated with full lines while CT states are indicated with dashed lines. (A) CAM-B3LYP functional. (B) LC-PBE functional.

In what follows it is presented a new strategy for obtaining functionals aimed at fixing the problem of the bright CT state and at the same time at ameliorating, as much as possible, the RB transition energy. This strategy is based on the following three main concepts arising from the above summary: (i) in order to reduce the brightness of the CT state, the SR HF exchange has to take small values; (ii) the  $\gamma$  parameter has to be optimally-tuned to ensure a correct description of CT states; (iii) no tuning within solvent is performed, but the screening is still considered through the relation  $\alpha + \beta = 1/\varepsilon$ . The first step of the procedure is the usual  $\gamma$  optimal-tuning in vacuum performed by using several  $\alpha, \beta$  couples in which  $\alpha$  takes small values (small fractions of HF exchange) and  $\beta$  is given by  $1 - \alpha$  (correct asymptotic behavior). The second step consists in a parameter scanning aimed at obtaining the best transition energy for the solvated RB in which the scanned parameters are  $\alpha, \gamma^*$  couples where  $\alpha$  is the value set in the optimal-tuning and  $\gamma^*$  is the associated optimal value, and where  $\beta$  which is calculated for each couple as  $\beta = 1/\varepsilon - \alpha$ .

The results of the  $\alpha, \gamma^*$  scanning (the values of Table 4.1 have been used) for both CAM-

CAM-B3LYP	Transition energy (eV)	LC-PBE	Transition energy (eV)
$\alpha = 0 \quad \gamma^* = 0.10$	2.61	$\alpha = 0 \quad \gamma^* = 0.18$	2.48
$\alpha = 0.05 \quad \gamma^* = 0.17$	2.51	$\alpha = 0.05 \quad \gamma^* = 0.17$	2.50
$\alpha = 0.10 \quad \gamma^* = 0.16$	2.55	$\alpha = 0.10 \quad \gamma^* = 0.16$	2.55
$\alpha = 0.15 \quad \gamma^* = 0.14$	2.58	$\alpha = 0.15 \quad \gamma^* = 0.14$	2.58
$\alpha = 0.20 \quad \gamma^* = 0.13$	2.63	$\alpha = 0.20 \quad \gamma^* = 0.13$	2.62

**Table 4.6:** RB transition energy predicted by different couples of  $\alpha, \gamma^*$  values (in all cases  $\beta = 1/\varepsilon - \alpha$ ).

B3LYP and LC-PBE functionals are reported in the Table 4.6. What emerges is that the discrepancy on the transition energy is greatly reduced with respect to the previously tested RSH functionals, and the observed general trend is an uniform decrease of the error upon reducing the  $\alpha$  value (i.e., the amount of SR HF exchange). Again, the effect of considering different kinds of DFT exchange is visible only when no HF exchange is introduced: for LC-PBE, the error continues to decrease even when  $\alpha$  reaches the zero value, while the opposite behaviour is observed for CAM-B3LYP.

The ESs predicted for the H and J dimers are reported in Figure 4.11, from which it clearly appears that the strategy of forcing small  $\alpha$  values successfully eliminates the problem of the CT bright state in the H dimer. The fact that this recipe ameliorates also the RB transition energy indicates that a proper amount of SR HF is a fundamental condition for reaching a correct description for the ESs of RB and its dimers. In conclusion,  $\alpha$  values of about 0.10-0.15 can be considered reliable for both CAM-B3LYP and LC-PBE functionals, because too small values should be avoided since they could lead to apparently good results by virtue of compensation errors arising from the use of almost 100% of SR DFT exchange (this seems to be the case of the LC-PBE functional with  $\alpha = 0, \gamma^* = 0.18$  which, differently from the case of the CAM-B3LYP with  $\alpha = 0, \gamma^* = 0.10$ , improves the transition energy with respect to  $\alpha = 0.5$  case).

Regarding the possibility of having fluorescent J dimers, from the comparison with the ESs predicted by the standard and optimally-tuned RSH functionals, it can be noticed that (at least for the considered geometry) the first CT state is slightly stabilized below the first LE state, but since the energy difference between them is quite low (about 0.02 eV for  $\alpha = 0.10, \gamma^* = 0.16$  and 0.03 eV for  $\alpha = 0.15, \gamma^* = 0.14$ ) one can speculate that different J conformations having more spaced RBs can present a more destabilized CT state passing above the LE one thereby allowing the fluorescence from the lowest bright state. The study of other geometrical conformations, thus, represents a perspective for future research in this context.



# Conclusions.

The RB tendency to dimerization represents a critical issue that can seriously undermine the technological application of RB-based LH NPs: indeed, being H dimers fluorescence quenchers, they could be responsible for a severe loss of excitations from the dye network, which is in turn responsible for a sensible reduction of the ET efficiency. A very important information to achieve is how the ET processes are affected by the quenching in the temporal scale, and macroscopic models offer a reliable tool for shedding light on such an influence through the analysis of fluorescence decay measurements. In order to establish a reliable macroscopic model for describing the fluorescence decay within LH NPs, the Gösele model has been used for including both EEA and quenching from dimers. The detailed analysis of all the parameters entering the macroscopic model led to the conclusion that when a small fraction of RB is assumed to dimerize, the quenching becomes visible only in the long time scale of the decay, where it produces an acceleration that can be considered as the straightforward signature for the presence of quenching species. Such an acceleration, could be in principle exploited for determining (through global fitting analysis) relevant chemical and photophysical parameters, such as the quencher concentration and its non-radiative lifetime.

Macroscopic models assume a homogeneous distributions of dyes, and therefore cannot provide any insight about the system organization at the mesoscopic scale, i.e. the spatial arrangement of the RB molecules within the LH NPs. In such regard, important information can be instead achieved through MD simulations, which allow characterization at the atomistic level of the arrangement of RB molecules within a nano-sized network of dyes and counterions. However, in order to get reliable MD simulations, a properly parametrization of the FF is required. In particular, since the networks formed within the LH NPs could be composed of very close RB units, the RB intramolecular flexibility and the RB-RB interactions become fundamental features that have to be correctly accounted for. Therefore, DFT calculations have been used as reference for parametrizing the RB intramolecular torsions and the LJ parameters describing the xanthene-xanthene interaction occurring in two RBs approaching to form a stacked H dimer. The parametrized FF has been tested by comparing MD simulations carried on 10 RB molecules in water solution in presence of F5TPB and iodide counterions. As expected, in the presence of the F5TPB counterions, the RB-F5TPB clustering experimentally observed has been correctly predicted (formation of a single aggregate or at most two separated aggregates), while in the presence of iodide no clustering has been observed. Moreover, the role of spacer proposed for the F5TPB bulky counterion has been clearly corroborated by the performed MD simulations. Indeed, only few stacked dimers are observed within RB/F5TPB aggregates and, most importantly, the formation

## Conclusions

---

of stacked H dimers (i.e. the potential quenchers) has turned out to represent a quite rare event, being the crossed-J the preferred stacked form. Finally, it is worth noting that despite the parametrization for the RB-RB interaction required a severe increase of the attractive interaction between the xanthenes planes to correctly reproduce the binding energy in a H dimer, this has not led to any preferential formation of H dimers that, indeed, resulted largely prevented by the bulky counterions. Therefore, the presented FF can be considered a reliable tool to be used in more for sophisticated simulations, including for instance also the polymer chains that would provide realistic models of synthetic LH NPs.

At the microscopic scale, QM methods can be used for determining the electronic properties of the individual molecules composing the system and the stability of specific dimeric conformations. Being RB a rather extended conjugated system, its electronic structure calculation is not feasible by means of wavefunction methods, and therefore one has to rely on the use of DFT. The presented QM study has been organized in two parts: the first aimed at rationalizing at the DFT level the F5TPB capability to hinder the formation of stacked dimers, while the second focused on finding a proper DFT functional for describing the optical and photophysical properties of dimers (in absence of counterions for simplicity) at the TD-DFT level.

In order to demonstrate the stabilizing effect given by the F5TPB spacer, this counterion has been compared with the small chloride: several dimer guess geometries have been optimized by using the B3LYP-D3 functional and their relative stabilities have been analyzed. It has been found that when F5TPB is considered, the conformation in which this counterion is intercalated between the two RBs is more stable with respect to the stacked form presenting the counterion outside. Instead, when chloride is considered no spacing action is possible: indeed, when the small counterion is intercalated between the two RBs, the geometry optimization readily removes it to allow reaching the stacked form, which has been found to be the most stable in this case.

When TD-DFT methods are used for describing the photophysical properties of a certain molecule, one fundamental quantity that has to be correctly reproduced is the transition energy associated to the experimental main absorption peak. In order to individuate a reliable DFT functional, two different families have been tested on RB and its H and J dimers, including standard hybrid (B3LYP and PBE0) and RSH (CAM-B3LYP and LC-PBE), optimally-tuned RSH ( $\gamma^*$ CAM-B3LYP and  $\gamma^*$ LC-PBE) and an optimally-tuned RSH accounting for the solvent screening (S- $\gamma^*\alpha^*$ CAM-B3LYP and S- $\gamma^*\alpha^*$ LC-PBE). RSH functionals have been demonstrated to be the most reliable for achieving a correct description of CT states, but when applied to RB they have been found to predict a very overestimated transition energy, even in their optimally-tuned versions (errors ranging from 0.5 to 0.7 eV). Moreover, the error on the RB transition energy is always accompanied by the prediction of a spurious bright CT state in the H dimer. The detailed analysis on the effect of the parameters defining the RSH functionals (i.e., the range separation parameter and the HF exchange amounts introduced at short and long ranges) has showed that the short range HF exchange is the crucial quantity for ameliorating the performances. In particular, it has been found that a small fraction of this exchange allows to compute an improved transition energy and, at the same time, to fix also the problem of the CT bright state. Basing on these findings, a new class of functionals containing a sufficiently small fraction of short range HF exchange (but which is nevertheless physically motivated based on the optimal tuning concept) has been proposed and tested on dimers. The quenching in H dimer has been proved to be due

to the presence of dark low lying LE states, while the possibility of having fluorescence from J dimers, which is correctly predicted by standard and optimally-tuned RSH functionals, can be speculated to be retained also with these new functionals.

Overall, this PhD thesis, not only provides several insights into the structural, photo-physical and optical properties of the RB dye and its aggregates (especially its dimers), but also represents an example of multiscale study based on various type of computational tools that can be used to understand different chemico-physical phenomena (e.g. ET, aggregation, structural-dependent optical properties, etc.) in complex systems, spanning from the microscopic to the macroscopic scale.

## Conclusions

---

## Appendix A

# Force Field Parameters.

In this Appendix are reported the new FF parameters obtained for the RB ethyl ester and the F5TPB counterion. All the reported values have been obtained from DFT calculations performed with the B3LYP-D3 functional and the 6-31G\* basis set.

The new atom types defined for the RB parametrization are reported in Figure A.1, along with some of the GAFF atom types required for the parameterization of equilibrium bond lengths and dihedral angles. The new parametrized equilibrium bond lengths are reported in Table A.1. Regarding the associated force constants, the GAFF values are kept by considering for each carbon atom in the xanthene plane the GAFF ca atom type. The new parameters obtained for the torsional energy profiles of xanthene-phenyl, xanthene-amine and phenyl-carboxyl dihedral angles are reported in Tables A.2, A.3 and A.5 respectively. The LJ parameters for the atoms indicated in Figure 3.2 that have been parametrized for describing the RB-RB interaction in a stacked H dimer are instead reported in Table A.6.

Regarding the F5TPB counterion, the calculated equilibrium bond length and force constant for the B-C bond are 1.6612 Å and 541.1 kcal mol<sup>-1</sup> rad<sup>-2</sup> respectively. The vdW parameters for boron have been taken from ref.[41], and read  $\sigma = 2.15$  Å and  $\epsilon = 0.14$  kcal/mol. The parameters for the torsion involving boron (rotation of the X-b-ca-X dihedral angle) have been approximated with those for the X-C(sp<sup>2</sup>)-C(sp<sup>2</sup>)-X torsion of the tetraphenyl-methane taken from ref.[41], in which a vanishing torsional energetic contribution is considered for this dihedral.

## Force Field Parameters

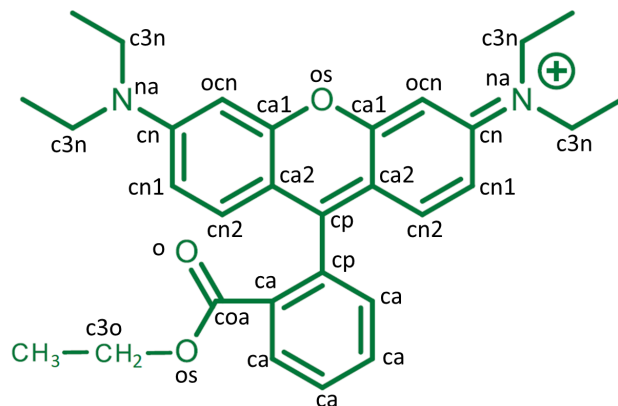


**Figure A.1:** New atom types defined for the FF parameterization of RB ethyl ester. In this picture are reported also some of the GAFF atom types (ca, cp, o, oc, na).

atom types	Equilibrium length (Å)	atom types	equilibrium length (Å)
coa o	1.2407	cn1 ha	1.0870
coa ca	1.4870	cn cn1	1.4420
coa os	1.3650	cn na	1.3500
c3o os	1.4756	ocn cn	1.4210
c3o hc	1.0920	ocn ha	1.0870
c3o c3	1.5350	ocn ca1	1.3870
ca2 cp	1.4094	c3n na	1.4860
ca2 ca1	1.4228	c3n c3	1.5350
ca1 os	1.3865	c3n hc	1.0920
cn2 ca2	1.4252	cn2 cn1	1.3688
cn2 ha	1.0870		

**Table A.1:** New parametrized equilibrium bond lengths for the RB ethyl ester.

$n$	2	4	6	8
$V_n$	-1.6414	0.1914	-0.0582	-0.1644

**Table A.2:** New parameters describing the xanthene-phenyl torsion (rotation of the X-cp-cp-X dihedral angle). The  $n$  values indicate the different periodicity contributions, while the  $V_n$  values are the corresponding amplitudes (kcal/mol), see eq.(3.4).

---

**Force Field Parameters**

---

$n$	2	4	8	10	12
$V_n$	-1.7024	0.0224	-0.1055	0.0543	-0.0672

**Table A.3:** New parameters describing the xanthene-amine torsion (rotation of the X-cn-na-X dihedral angle). The  $n$  values indicate the different periodicity contributions, while the  $V_n$  values are the corresponding amplitudes (kcal/mol), see eq.(3.4).

$n$	2	4	6	8	10
$V_n$	-1.591	0.0192	-0.0201	-0.0326	-0.0314

**Table A.4:** New parameters describing the phenyl-carboxyl torsion (rotation of the X-ca-coa-X dihedral angle). The  $n$  values indicate the different periodicity contributions, while the  $V_n$  values are the corresponding amplitudes (kcal/mol), see eq.(3.4).

$n$	2	4	6	8	10
$V_n$	-1.591	0.0192	-0.0201	-0.0326	-0.0314

**Table A.5:** New parameters describing the phenyl-carboxyl torsion (rotation of the X-ca-coa-X dihedral angle). The  $n$  values indicate the different periodicity contributions, while the  $V_n$  values are the corresponding amplitudes (kcal/mol), see eq.(3.4).

os na	-0.34000	ca1 ocn	-0.17198
os ca1	-0.24182	ca1 cn	-0.17198
os ca2	-0.24182	ca1 cn1	-0.17198
os ocn	-0.24182	ca1 cn2	-0.17198
os cn	-0.24182	ca2 ocn	-0.17198
os cn1	-0.24182	ca2 cn	-0.17198
os cn2	-0.24182	ca2 cn1	-0.17198
na ca1	-0.24182	ca2 cn2	-0.17198
na ca2	-0.24182	ocn cn	-0.17198
na ocn	-0.24182	ocn cn1	-0.17198
na cn	-0.24182	ocn cn2	-0.17198
na cn1	-0.24182	cn cn1	-0.17198
na cn2	-0.24182	cn cn2	-0.17198
ca1 ca2	-0.17198	cn1 cn2	-0.17198

**Table A.6:** New LJ parameters describing the RB-RB interaction in a stacked H dimer. The reported values refer to the  $\epsilon_{AB}$  parameters (kcal/mol) of eq.(3.7).

## Force Field Parameters

---

# Bibliography

- [1] K. Trofymchuk, A. Reisch, P. Didier, F. Frasc, P. Gilliot, Y. Mély, A. S. Klymchenko, *Nat. Photonics* **2017**, 11, 657-663.
- [2] A. Reisch, P. Didier, L. Richert, S. Oncul, Y. Arntz, Y. Mély, A. S. Klymchenko, *Nat. Commun.* **2014**, 5, 4089.
- [3] F. López Arbeola, P. Ruiz Ojeda, I. López Arbeola, *J. Lumin.* **1989**, 44, 105.
- [4] C. V. Bindhu, S. S. Harilal, *Anal. Sci.*, **2001**, 17, 141.
- [5] I. Shulov, S. Oncul, A. Reisch, Y. Arntz, M. Collot, Y. Mely, A. S. Klymchenko, *Nanoscale*, **2015**, 7, 18198–18210.
- [6] X.-F. Zhang, Y. Zhang, L. Liu, *J. Lumin.* **2014**, 145, 448–453.
- [7] M. Beija, C. A. M. Afonso, J. M. G. Martinho, *Chem. Soc. Rev.* **2009**, 38, 2410.
- [8] N. Bar, P. Chowdhury, *ACS Appl. Electron. Mater.* **2022**, 4, 3749–3771.
- [9] M. R. Mohebbifar, *Optik* **2021**, 242, 166902.
- [10] D. Moreau, C. Lefort, R. Burke, P. Leveque, R. P. O'Connor, *Biomed. Opt. Express* **2015**, 6, 4105.
- [11] I. López Arbeloa, P. Ruiz Ojeda, *Chem. Phys. Lett.* **1982**, 87, 556.
- [12] M. Kasha, H. R. Rawls, M. Ashraf El-Bayoumi, *Pure Appl. Chem.* **1965**, 11, 371-392.
- [13] K. Kemnitz, N. Tamai, I. Yamazaki, N. Nakashima, K. Yoshihara, *J. Phys. Chem.*, **1986**, 90, 5094-5101.
- [14] F. del Monte, D. Levy, *J. Phys. Chem. B* **1998**, 102, 8036-8041.
- [15] Q. Yuan, X. Zhang, Z. Wang, M. H. M. A. Shibraen, S. Yang, J. Xu, *Colloids and Surfaces A: Physicochem. Eng. Aspects*, **2015**, 486, 139-144.
- [16] B. Andreiuk, A. Reisch, E. Bernhardt, A. S. Klymchenko, *Chem. Asian J.* **2019**, 14, 836-846.
- [17] A. Reisch, K. Trofymchuk, A. Runser, G. Fleith, M. Rawiso, A. S. Klymchenko, *ACS Appl. Mater. Interfaces* **2017**, 9, 43030-43042.

## Bibliography.

---

- [18] T. Förster, *Ann. Phys.*, **1948**, 2, 55-75.
- [19] T. Förster, *Z. Naturforsch.*, **1949**, 4, 321-327.
- [20] I. Medintz, N. Hildebrandt (ed), *FRET- Förster Resonance Energy Transfer*, Wiley-VCH (2013).
- [21] G. D. Scholes, *Annu. Rev. Phys. Chem.* **2003**, 54, 57-87.
- [22] U. Gösele, M. Hauser, U. K. A. Klein, *Z. Physik. Chem. Neue Folge* **1975**, 99, 81-96.
- [23] T. R. Waite, *Phys. Rev.* **1957**, 107, 463-470.
- [24] U. Gösele, M. Hauser, U. K. A. Klein, R. Frey, *Chem. Phys. Lett.* **1975**, 34, 519-522.
- [25] S. Jang, K. J. Shin, S. Lee. *J. Chem. Phys.* **1995**, 102, 815-827.
- [26] F. Fennel, S. Lochbrunner, *Phys. Rev. B* **2015**, 92, 140301.
- [27] S. W. Haan, R. Zwanzig, *J. Chem. Phys.* **1978**, 68, 1879.
- [28] C. R. Gochanour, H. C. Andersen, M. D. Fayer, *J. Chem. Phys.* **1979**, 70, 4254.
- [29] J. E. Jones, *Proc. R. Soc. Lond. Ser. A* **1926**, 106, 463-477.
- [30] H. C. Andersen, *J. Chem. Phys.* **1980**, 72, 2384-2393.
- [31] H. J. C. Berendsen, J. P. M. Postma, W. F. Vangunsteren, A. Dinola, J. R. Haak, *J. Chem. Phys.* **1984**, 81, 3684-3690.
- [32] H. Ouachtak, R. El Haouti, A. El Guerdaoui, R. Haounati, E. Amaterz, A. A. Addi, F. Akbal, M. L. Taha, *J. Mol. Liq.* **2020**, 309, 113142.
- [33] V. Narayanaswamy, S. Alaabed, M.-A. Al-Akhras, I. M. Obaidat, *Mater. Today Proc.* **2020**, 28, 1078-1083.
- [34] N. Magalhães, G. M. Simões, C. Ramos, J. Samelo, A. C. Oliveira, H. A. L. Filipe, J. P. P. Ramalho, M. J. Moreno, L. M. S. Loura, *Molecules*, **2022**, 27, 1420.
- [35] J. Wang, R. M. Wolf, J. W. Caldwell, P. A. Kollman, D. A. Case, *J. Comput. Chem.* **2004**, 25, 1157-1174.
- [36] Gaussian 16, Revision C.01, M. J. Frisch, G. W. Trucks, H. B. Schlegel, G. E. Scuseria, M. A. Robb, J. R. Cheeseman, G. Scalmani, V. Barone, G. A. Petersson, H. Nakatsuji, X. Li, M. Caricato, A. V. Marenich, J. Bloino, B. G. Janesko, R. Gomperts, B. Mennucci, H. P. Hratchian, J. V. Ortiz, A. F. Izmaylov, J. L. Sonnenberg, D. Williams-Young, F. Ding, F. Lipparini, F. Egidi, J. Goings, B. Peng, A. Petrone, T. Henderson, D. Ranasinghe, V. G. Zakrzewski, J. Gao, N. Rega, G. Zheng, W. Liang, M. Hada, M. Ehara, K. Toyota, R. Fukuda, J. Hasegawa, M. Ishida, T. Nakajima, Y. Honda, O. Kitao, H. Nakai, T. Vreven, K. Throssell, J. A. Montgomery, Jr., J. E. Peralta, F. Ogliaro, M. J. Bearpark, J. J. Heyd, E. N. Brothers, K. N. Kudin, V. N. Staroverov, T. A. Keith, R. Kobayashi, J. Normand, K. Raghavachari, A. P. Rendell, J. C. Burant, S. S. Iyengar, J. Tomasi, M.

## Bibliography.

---

- Cossi, J. M. Millam, M. Klene, C. Adamo, R. Cammi, J. W. Ochterski, R. L. Martin, K. Morokuma, O. Farkas, J. B. Foresman, and D. J. Fox, Gaussian, Inc., Wallingford CT, 2016.
- [37] J. C. Phillips, D. J. Hardy, J. D. C. Maia, J. E. Stone, J. V. Ribeiro, R. C. Bernardi, R. Buch, G. Fiorin, J. Héning, W. Jiang, R. McGreevy, M. C. R. Melo, B. K. Radak, R. D. Skeel, A. Singharoy, Y. Wang, B. Roux, A. Aksimentiev, Z. Luthey-Schulten, L. V. Kalé, K. Schulten, C. Chipot, E. Tajkhorshid, *J. Chem. Phys.*, **2020**, 153, 044130.
- [38] J. Comer, J. C. Gumbart, J. Héning, T. Lelièvre, A. Pohorille, C. Chipot, *J. Phys. Chem. B* **2015**, 119, 3, 1129-1151.
- [39] A. Pizzirusso, M. E. Di Pietro, G. De Luca, G. Celebre, M. Longeri, L. Muccioli, C. Zannoni, *ChemPhysChem* **2014**, 15, 1356-1367.
- [40] Y. Wu, H. L. Tepper, G. A. Voth, *J. Chem. Phys.*, **2006**, 124, 024503.
- [41] S. Amirjalayer, R. Q. Snurr, R. Schmid, *J. Phys. Chem. C* **2012**, 116, 4921-4929.
- [42] L. Martínez, R. Andrade, E. G. Birgin, J. M. Martínez, *J. Comput. Chem.* **2009**, 30, 2157-2164.
- [43] L. Pauling, E. B. Wilson, *Introduction to Quantum Mechanics*, McGraw-Hill (1935).
- [44] W. Pauli, *Phys. Rev.* **1940**, 58, 716-722.
- [45] F. L. Pilar, *Elementary Quantum Chemistry*, 2nd ed., Dover Publications (2001).
- [46] P. W. Atkins, R. S. Friedman, *Molecular Quantum Mechanics*, 4th ed., Oxford University Press (2005).
- [47] J. C. Slater, *Phys. Rev.* **1929**, 34, 1293.
- [48] E. Schrödinger, *Ann. d. Phys.* **1926**, 79, 361.
- [49] S. T. Epstein, *The Variational Method in Quantum Chemistry*, Academic Press (1974).
- [50] V. Fock, *Z. Physik* **1930**, 61, 126.
- [51] J. C. Slater, *Phys. Rev.* **1930**, 35, 210.
- [52] D. R. Hartree, *Proc. Cambridge Phil. Soc.*, **1928**, 24, 89.
- [53] J. C. Slater, *Phys. Rev.* **1931**, 38, 1109.
- [54] E. U. Condon, *Phys. Rev.* **1930**, 36, 1121.
- [55] A. Szabo, N. S. Ostlund, *Modern Quantum Chemistry*, Dover Publications (1996).
- [56] T. C. Koopmans, *Physica*, **1934**, 1, 104-113.
- [57] R. G. Parr, W. Yang, *Density Functional Theory*, Oxford University Press (1989).

## Bibliography.

---

- [58] W. Koch, M. C. Holthausen, *A Chemist's Guide to Density Functional Theory*, Wiley-VCH (2001).
- [59] P. Hohenberg, W. Kohn, *Phys. Rev. B*, **1964**, 136, B864-B871.
- [60] W. Kohn, L. J. Sham, *Phys. Rev.* **1965**, 140, 1133.
- [61] F. Bloch, *Zeitschrift Fur Physik*, **1929**, 57, 545-555.
- [62] P. A. M. Dirac, *Proc. Camb. Philos. Soc.* **1930**, 26, 376-385.
- [63] J. P. Perdew, Y. Wang, *Phys. Rev. B* **1992**, 45, 13244-13249.
- [64] S. H. Vosko, L. Wilk, M. Nusair, *Can. J. Phys.* **1980**, 58, 1200-1211.
- [65] A. D. Becke, *Phys. Rev. A* **1988**, 38, 3098-3100.
- [66] C. T. Lee, W. T. Yang, R. G. Parr, *Phys. Rev. B* **1988**, 37, 785-789.
- [67] J. P. Perdew, K. Burke, M. Ernzerhof, *Phys. Rev. Lett.* **1996**, 18, 3865-3868.
- [68] S. Grimme, J. Antony, S. Ehrlich, H. Krieg, *J. Chem. Phys.* **2010**, 132, 154104.
- [69] A. Seidl, A. Görling, P. Vogl, J. A. Majewski, M. Levy, *Phys. Rev. B*, **1996**, 53, 3764-3774.
- [70] R. Garrick, A. Natan, T. Gould, L. Kronik, *Phys. Rev. X* **2020**, 10, 021040.
- [71] C. Adamo, V. Barone, *J. Chem. Phys.* **1999**, 110, 6158-6170.
- [72] A. D. Becke, *J. Chem. Phys.* **1993**, 98, 5648-5652.
- [73] P. J. Stephens, F. J. Devilm, C. F. Chabalowsky, M. J. Frish, *J. Phys. Chem.* **1994**, 98, 11623-11627.
- [74] T. Leininger, H. Stoll, H.-J. Werner, A. Savin, *Chem. Phys. Lett.* **1997**, 275, 151-160.
- [75] T. Yanai, D. P. Tew, N. C. Handy, *Chem. Phys. Lett.* **2004**, 393, 51-57.
- [76] W. Song, T. Hirose, T. Tsuneda, K. Hirao, *J. Chem. Phys.* **2007**, 126, 154105.
- [77] R. Cammi, B. Mennucci, J. Tomasi, in J. Leszczynski (ed), *Computational Chemistry: Reviews of Current Trends*, Vol. 10, Chapter 1, World Scientific (2003).
- [78] B. Mennucci, *WIREs Comput Mol Sci* **2012**, 2, 386-404.
- [79] E. Cancès, B. Mennucci, J. Tomasi, *J. Chem. Phys.* **1997**, 107, 3032-3041.
- [80] B. Mennucci, E. Cancès, J. Tomasi, *J. Phys. Chem. B* **1997**, 101, 10506-10517.
- [81] M. Cossi, V. Barone, *J. Chem. Phys.* **2001**, 115, 4708-4717.
- [82] P. Jørgensen, J. Olsen, in D. R. Yarkony (ed), *Modern Electronic Structure Theory*, Part II, Chapter 13, World Scientific (1995).

- [83] F. Jensen, *Introduction to Computational Chemistry*, 3rd ed., Wiley (2017).
- [84] P. Norman, K. Ruud, T. Saue, *Principles and Practices of Molecular Properties: Theory, Modeling, and Simulations*, Wiley (2018).
- [85] M. E. Casida, in D. P. Chong (ed), *Recent Advances in Density Functional Methods*, Vol. 1, Chapter 5, World Scientific (1995).
- [86] F. Furche, *J. Chem. Phys.* **2001**, 114, 5982-5992.
- [87] A. Dreuw, M. Head-Gordon, *Chem. Rev.* **2005**, 105, 4009-4037.
- [88] A. Dreuw, J. L. Weisman, M. Head-Gordon, *J. Chem. Phys.* **2003**, 119, 2943-2946.
- [89] R. L. Martin, *J. Chem. Phys.* **2003**, 118, 4775-4777.
- [90] A. T. Amos, G. G. Hall, *Proc. Roy. Soc. A* **1961**, 263, 483-493.
- [91] S. Kümmel, *Adv. Energy Mater.* **2017**, 7, 1700440.
- [92] J. Autschbach, *ChemPhysChem* **2009**, 10, 1757-1760.
- [93] N. T. Maitra, *J. Phys. Condens. Matter* **2017**, 29, 423001.
- [94] J. P. Perdew, M. Levy, *Phys. Rev. B* **1997**, 56, 16021-16028.
- [95] J. P. Perdew, R. G. Parr, M. Levy, J. L. Balduz, *Phys. Rev. Lett.* **1982**, 49, 1691-1694.
- [96] A.M. Teale, F. De Proft, D. J. Tozer, *J. Chem. Phys.* **2008**, 129, 044110.
- [97] J. P. Perdew, M. Levy, *Phys. Rev. Lett.* **1983**, 51, 1884-1983.
- [98] D. J. Tozer, *J. Chem. Phys.* **2003**, 119, 12697-12699.
- [99] T. Stein, L. Kronik, R. Baer, *J. Am. Chem. Soc.* **2009**, 131, 2818-2820.
- [100] M. Alipour, Z. Safari, *J. Phys. Chem. C*, **2019**, 123, 746-761.
- [101] M. J. Peach, P. Benfield, T. Helgaker, D. J. Tozer *J. Chem. Phys.* **2008**, 128, 044118.
- [102] A. K. Manna, M. H. Lee, K. L. McMahon, B. D. Dunietz, *J. Chem. Theory Comput.* **2015**, 11, 1110-1117.
- [103] N. Kuritz, T. Stein, R. Baer, L. Kronik, *J. Chem. Theory Comput.* **2011**, 7, 2408-2415.
- [104] K. Okuno, Y. Shigeta, R. Kishi, M. Nakano, *Chem. Phys. Lett.* **2013**, 585, 201-206.
- [105] Y. Jiang, Z. Hu, B. Zhou, C. Zhong, Z. Sun, H. Sun, *J. Phys. Chem. C* **2019**, 123, 5616-5625.
- [106] H. Sun, C. Zhong, J.-L. Brédas *J. Chem. Theory Comput.* **2015**, 11, 3851-3858.
- [107] L. Kronik, S. Kümmel, *Adv. Mater.* **2018**, 30, 1706560.
- [108] T. B. de Queiroz, S. Kümmel, *J. Chem. Phys.* **2014**, 141, 084303.

## Force Field Parameters

---

- [109] K. Garrett, X. A. Sosa Vazquez, S. B. Egri, J. Wilmer, L. E. Johnson, B. H. Robinson, C. M. Isborn *J. Chem. Theory Comput.* **2014**, 10, 3821-3831.
- [110] C. Halsey-Moore, P. Jena, J. T. McLeskey Jr., *Comput. Theo. Chem.* **2019**, 1162, 112506.
- [111] B. Joo, H. Han, E.-G. Kim, *J. Chem. Theory Comput.* **2018**, 14, 2823-2828.
- [112] S. Bhandari, B. D. Dunietz, *J. Chem. Theory Comput.* **2019**, 15, 4305-4311.
- [113] A. R. Godfrey Alig, D. Gourdon, J. Israelachvili, *J. Phys. Chem. B* **2007**, 111, 95-106.
- [114] D. Setiawan, A. Kazaryan, M. A. Martoprawiro, M. Filatov, *Phys. Chem. Chem. Phys.* **2010**, 12, 11238-11244.